ANALYSIS OF ACOUSTIC SCATTERING FROM LARGE FISH SCHOOLS USING BLOCH WAVE FORMALISM

A Dissertation
Presented to
The Academic Faculty

by

Jason A. Kulpe

In Partial Fulfillment
of the Requirements for the Degree
Doctor of Philosophy in the
George W. Woodruff School of Mechanical Engineering

Georgia Institute of Technology
May 2015

ANALYSIS OF ACOUSTIC SCATTERING FROM LARGE FISH SCHOOLS USING BLOCH WAVE FORMALISM

Approved by:

Dr. Michael J. Leamy,
Committee Chair
School of Mechanical Engineering
Georgia Institute of Technology

Dr. Michael J. Leamy, Advisor
School of Mechanical Engineering
Georgia Institute of Technology

Dr. Karim Sabra, Co-Advisor
School of Mechanical Engineering
Georgia Institute of Technology

Dr. Massimo Ruzzene
School of Mechanical Engineering
Georgia Institute of Technology

Dr. Nico F. Declercq
School of Mechanical Engineering
Georgia Institute of Technology

Dr. Julian J. Rimoli
School of Aerospace Engineering
Georgia Institute of Technology

Date Approved: 17-February-2015

ACKNOWLEDGEMENTS

For me, this Thesis is the culmination of 4 and a half years in graduate school, and near 10 entire years at Georgia Tech. This time has provided me numerous helpful and memorable experiences (including ten full years of football as a student). Within my time at Georgia Tech I learned an abundance of technical, professional, and life-based information.

Since I was a child, I had a high degree of curiosity and always wanted to learn new things and understand how the world works. Like many engineers, I got an early start with technical and practical hands-on abilities with Legos. Later, within my undergraduate degree at Georgia Tech, I was a member (and loved it) of the RoboJackets student robotics club. One day I asked Dr. Mike Leamy, my current undergraduate dynamics instructor, about a dynamics simulation issue for a RoboJackets project. After assessing my abilities and curiosity, a few months later, in the spring of 2008, he offered me an undergraduate research position regarding computational acoustics and the finite element method. Later, in 2010, Dr. Karim Sabra asked me to work on a fish acoustics project, co-advised with Dr. Leamy. The rest, you can say, is history.

In my time in graduate school I received an abundance of assistance from my advisers, Dr. Leamy and Dr. Sabra. I received, not only, advise and recommendations during the tough research times, but enjoyable social discussions as well. They provided a great graduate school experience that was full of opportunities. Through their advisement and patience, they pushed me the best I can be and helped develop me into a researcher. I am also grateful to the others on my committee: Dr. Massimo Ruzzene, Dr. Nico Declercq, and Dr. Julian Rimoli. They provided other opportunities and assistance along the way during the project. Lastly, I would like

to thank Dr. Karim Sabra, Dr. Wayne Whiteman, and Dr. Aldo Ferri for the many teaching assistant and grading opportunities with increased financial support. All of these opportunities helped fuel my intellectual curiosity and further my career. For that I am very grateful.

Within my time at Georgia Tech, many of my friends offered invaluable assistance and enjoyable times. In my lab group, I am thankful and appreciative of the help from: Dr. Kevin Manktelow, Kyle Karlson, John Arata, Dekun Pei, Maj. Elsa Johnson, Oscar Peña, Justin Wilbanks, Matt Fronk, Douglas Cox, Shane Lani, Brendan Nichols, Katherine Woolfe, Shima Shahab, Toby Xu, and Bernie Shieh. Specifically, Dr. Manktelow taught me the Bloch theorem and many other wave-based topics. There are many others within the department, other departments, and the Acoustical Society of America student group that provided assistance and friendship as well.

I am also very grateful to my gorgeous fiancée Rachel. Over the years through graduate school, her compassion, support, and sense of humor kept me focused, determined, and able to enjoy life. Specifically, towards the end, she was there as a constant source of motivation to work hard and complete the research effort. Her parents and other family members also offered much support and enjoyable times. Rachel also is significantly better at cooking than I. Her delicious and healthy meals kept me energized through the years we've spent together and through the Thesis writing process. I am very happy with her an very thankful for her support through the Ph.D degree.

Last of all, I have to thank my parents, Don and Cathy, and sister, Megan. They were always understanding when I would be stretched on time and unable to spend time with them. Throughout my life, they always encouraged me to keep working hard. My father, especially, always encouraged me to work hard in life and seek new opportunities. Throughout my lifetime, I am very grateful for their guidance, assistance, and love.

At last, my time in graduate school and at Georgia Tech is coming to an end. I will forever remember not only the support, encouragement, assistance, and friendship from those mentioned above and countless others but also many enjoyable times; to all: Thank You. I am eager to see what awaits me in the future.

TABLE OF CONTENTS

LIST OF TABLES

LIST OF FIGURES

SUMMARY

In the open ocean acoustic scattering by SONAR sources can be dominated by large fish schools. Multiple scattering effects are strong and the individual fish air-filled swimbladders scatter in the 1-10 kHz frequency range for most fish sizes. Furthermore, these schools are typically large in comparison to the acoustic wavelength and the individual fish typically swim in nearly periodic arrangements with a separation distance of approximately one body length. Hence, this work takes the perspective that fish schools can be studied simply and effectively by invoking the formalism of Bloch waves in periodic media. Analysis of the periodic school is aided through the Bloch theorem which reduces the study of the entire school to the study of a unit cell containing a single fish swimbladder. Application of the Bloch formalism to the school requires study of acoustic reflection from a semi-infinite half-space composed of an infinite tessellation of air-filled swimbladders in water. This media is denoted a fluid phononic crystal (PC). The reflection is considered, using a finite element discretization of the unit cell and an expansion of Bloch waves for the transmitted wave field. Next, scattering from a large finite school is studied through the context of the Helmholtz-Kirchhoff integral theorem where the semi-infinite PC pressure, determined by the Bloch wave expansion, is used as the surface pressure. Validation of results is accomplished via comparison with a finite element model (two dimensions) and a low frequency analytical multiple scattering model (three dimensions). Analysis of the dispersion relationship of the infinite PC yields useful information for a large school, namely, the frequency corresponding to target strength peaks, even as wave incidence angles and internal fish spacing are varied. The scattering effects attributed to the shape and weak internal disorder of the finite school were investigated with the surface integral method and a perturbation scheme. A general model using Bloch formalism, that encompasses the internal fish structure, fish biologic properties, and realistic school effects such as varying school geometry and disorder, was formulated. Transient analysis of the frequency dependent scattering, using the proposed approach developed in this thesis, may assist SONAR operators better classify large fish schools based on the observed characteristics of the scattered field.

CHAPTER I

INTRODUCTION

1.1 Overview

In an ocean environment the propagation of acoustic waves is strongly dominated by the waves interaction with groups of marine animals. In particular, it is well known that at frequencies less than 30 kHz [17] scattering from a school of fish contributes to a large source of volume reverberation in the open ocean [17, 22]. Additionally, multiple scattering effects from the incident acoustic wave and the collective arrangement of fish lead to a complicated frequency response. The received scattered waves from schools of fish can cause false alarms in tactical mid-frequency SONAR (SOund Navigation And Ranging) (1-10 kHz) systems [35]. Hence, understanding the spatial and temporal scales of the acoustic scattering from large fish schools is important to improving these SONAR systems.

1.2 Schools of fish

In the 1-10 kHz frequency range, the acoustic scattering is largely dominated by the fish's air filled swimbladder [22, 56]. As such, the scattering from swimbladder bearing fish is approximated as scattering from a spherical air bubble given the large wavelength of the incident wave (1m) compared to the typical dimension of most swimbladders (cm). Researchers have developed scattering models of fish which encompass the acoustically viscous fish flesh, given by Love's model [56], or viscous-elastic swimbladder muscle wall [21] which accurately describe resonance effects of individual fish [21]. These prior works that capture the acoustic nature of the fish body were mostly motivated by the resonant scattering behavior of a single fish. The acoustic scattering of entire fish schools have been considered by way of statistical modeling by Refs. [3, 58], low frequency homogenization by Hahn [28], or self-consistent scattering (SCS) methods [22, 1]. Feuillade *et al.* [22] explored the target strength variations, under a low frequency assumption, from schools with varying internal structure. Alvarez and Ye [1] similarly considered target strength dependency on the ensonificaiton direction, with a scattering model, albeit more numerically cumbersome than the SCS method, suitable for arbitrary point scatterers.

Schooling fish typically swim, not in random, but in regular spatial arrangements such that the nearest neighbor distance is essentially fixed [69, 65]; often the fish swim with a separation distance equal to approximately a body length [69]; see Fig. 1. This observation has prompted many to model the internal school structure as a periodic crystal lattice, with individual fish centered on the lattice points; see Ref. [65] for a review. Cullen *et al.* considered a simple cubic (SC) structure in pilchard (Harengula spp.); further evidence [69, 68] refuted this internal structure. Pitcher [68] and Pitcher *et al.* [69] documented evidence supporting an icosahedral packing structure to minimize packing volume in a school of minnows (Phoxinus phoxinus) and saithe (Pollachius virens). Feuillade *et al.* [22] and later Alvarez and Ye [1] modeled the fish school as having an internal body centered cubic (BCC) structure. Nero *et al.* [63] empirically considered an artificial fish school, with swimbladders on the lattice points of a SC structure, for frequency dependent target strength calculations.

The above observations assist in modeling the position of the fish. Ultimately, the target strength (backscattered intensity), and other relevant acoustic quantities of a model can be derived from the backscattered pressure field. That is, the pressure scattered to a receiver at an arbitrary location in the far field. Modeling the acoustic scattering from entire fish schools is a formidable task. Assuming the fish's movement is zero, relative to the sound speed, the multiple scattering problem among

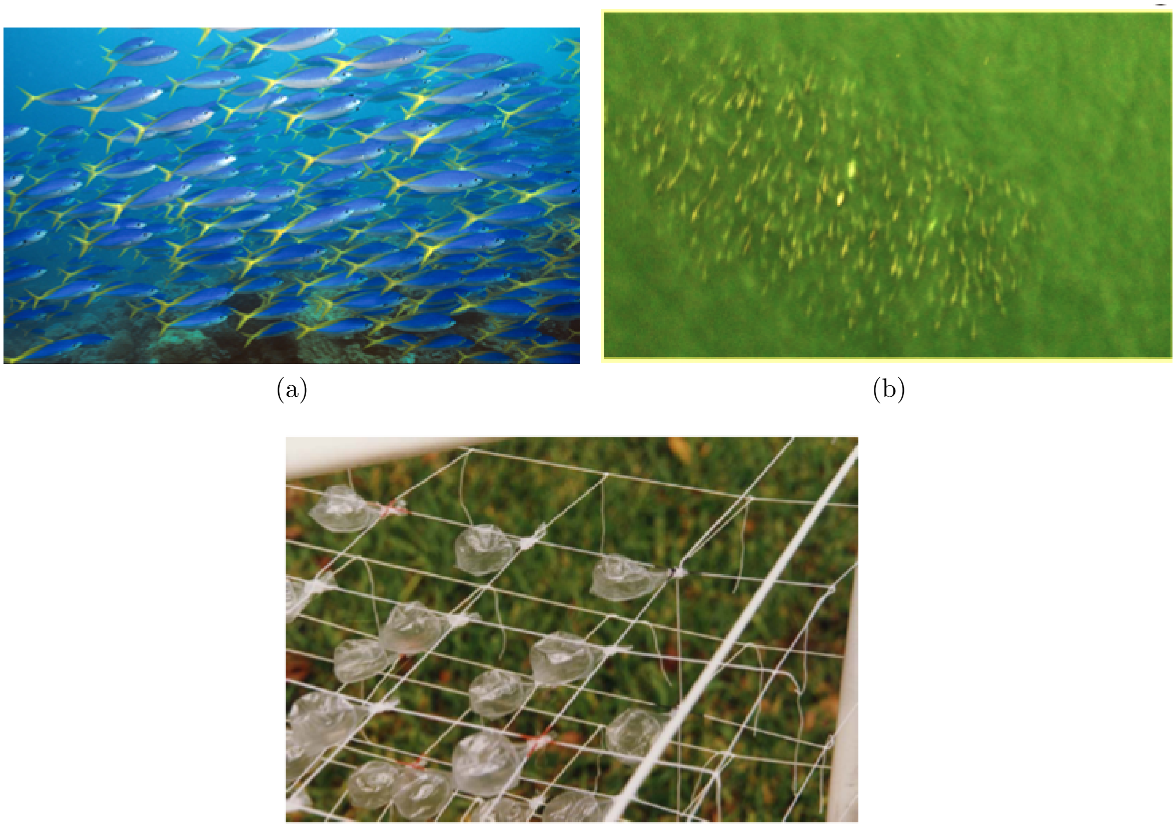

(a) (b)

(c)

Figure 1: Example (a) and (b) of fish photograph in their natural habitat. A degree of regularity can be observed. (a) fusiliers photographed by Randy Harwood in Papua New Guinea and (b) aerial photograph of adult tuna [83] (Fig. 1 in their work). (c) An experiment dealing with scattering from air-filled bubbles (proxy for a swimbladder) in a simple cubic array [63].

fish presents challenges. For a small number of fish, simple analytical, numerical, or experimental models may be adequate [22, 83, 14, 3]. For a large number of fish, with a potentially complicated school geometry, these prior methods can be impractical.

1.3 Phononic crystals

1.3.1 Previous work on PCs

Periodic arrays of scattering objects, embedded in a homogenous host medium, constitute a phononic crystal (PC). Multiple scattering effects combined with the resonances of the scattering objects lead to a complex dispersion relationship and the possibility of frequency band gaps and negative refraction [26, 78]. A band gap is a frequency range where there is no propagation allowed in the PC; the band gap is a consequence of the multiple scattering present inside the PC. A variety of PCs have been studied such as periodic arrays of fluid cylinders [8, 45] or spheres [12, 44] in a water background. Waveguides with periodic profiles [5], locally resonant periodic structures [55], and PCs designed to filter acoustic signals [77] are examples of structures engineered to exploit the frequency band gap behavior; see the example PCs in Fig. 2. Regardless of the system, knowledge of the dispersion relationship and associated acoustic wave fields are crucial for characterizing material and/or device response.

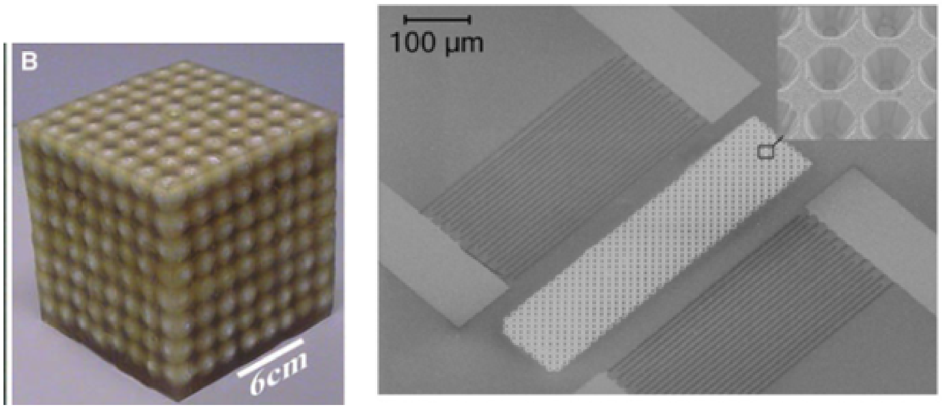

(a) (b)

Figure 2: Examples of phononic crystals studied in the literature. (a) A PC designed to exploit the resonance nature of the inclusions [55] (Fig. 1b in their work). (b) A micro-scale PC device developed to control wave behavior via exploitation of the band gaps [64] (Fig. 3 in their work).

A multitude of methods have been developed for dispersion computations, often focusing on wave dynamics within a single unit cell. Plane wave expansion methods, such as those detailed in Ref. [45], use Fourier expansions for the wave field and periodic material properties to compute the dispersion behavior, yet can experience convergence issues for highly contrasting material properties [77]. Chen and Ye [8] and Krynkin *et al.* [38] considered spherical harmonics via separation of variables to compute the dispersion relationship for given fluid, and respectively, fluid-solid crystals. Alternatively, transfer matrices [5] are well-suited for one-dimensional systems whereas finite difference techniques can also be used to numerically compute the dispersion of complex or finite periodic structures [77, 79]. Homogenization techniques [25, 37] are limited to low frequency systems and thus will not be considered here. Finite element (FE) based techniques [31, 18, 16, 46] allow calculation of the dispersion and acoustic wave field for arbitrary material and geometric configurations. The Bloch theorem [18, 34] allows one to consider a single unit cell of the periodic medium thereby enabling direct calculation of the dispersion behavior and a set of Bloch waves which describe the wave field within the entire medium.

In the context of periodic media, the Bloch theorem [18, 34] allows one to avoid studying the entire system and to instead consider a single unit cell for computation of the band structure. This theorem enables direct calculation of the dispersion behavior and a set of Bloch waves which describe the wave field within the PC. The FEM [16, 46], which allows for arbitrary inclusion geometry and materials (in the reference unit cell), is often employed to calculate the dispersion relationship and Bloch waves.

1.3.2 Scattering from PCs

In the past, authors have discussed the interaction of an external incident wave with a phononic crystal, to understand the effects of multiple scattering and PC dispersion on the wave field. The layer Korringa-Kohn-Rostoker (KKR) method [26, 74] is a common approximation method in the photonics literature where slabs of scattering objects, of infinite height, are correlated using specialized scattering matrix methods. Similar layer scattering methods have also been considered in elastic phononic crystals [70, 29]. Leroy *et al.* [52, 6] considered a layer method for modeling the reflection coefficients from successive thin layers of bubbles under low frequency limits.

Moiseyenko *et al.* [59, 60] conducted numerical FE studies that focused on diffraction of the incident wave but without a quantitative independent verification study of the pressure field results. Sanchis *et al.* [75] compared pressure fields using doubly multiple scattering theory versus experiment for an array of 35 aluminum cylinders periodically spaced in air. The work in Ref. [75], which did not exploit the periodicity of the structure, is the only work comparing analytical pressure fields to an independent verification study known to the authors of this work.

Researchers have applied a multitude of numerical techniques to study the interaction of a wave with finite phononic crystals. The finite difference time domain (FDTD) techniques offers a simple approach to a transient solution [77, 79] via discretization of the wave equation using divided differences. The finite element method (FEM) applied to PC geometries offers the flexibility of considering arbitrary material properties and geometries. Despite the straightforwardness of the prior two approaches, both can require high computational effort to analyze large PCs. Additionally, to prevent radiation from truncated computational boundaries from corrupting the results, either a very large homogenous domain must be employed, or specialized radiation boundary conditions must be developed [60].

Study of the external scattering from phononic crystals amounts to studying multiple scattering events between an incident acoustic wave and the PC constituents. The external scattering problem has received little attention in comparison to internal scattering and related band structure calculations. One possibility to obtain an accurate solution for a finite PC is to consider a multiple scattering approach using spherical harmonics [8]. This approach, however, does not exploit the inclusion periodicity, which can lead to an inefficient solution process for large PCs and also may require an expansion of a large number of Bessel functions. Work by Li *et al.* [53] considers the boundary element method, along with the Bloch theorem, to calculate dispersion and scattering from a PC. In this light, the Helmholtz-Kirchhoff integral

(HKI) [85, 86], which is the theoretical basis of the boundary element method, is attractive as the approach is general and encompasses the requisite spherical spreading necessary for wave scattering from finite objects. This analytical integral technique requires evaluation of a surface integral of the pressure and normal velocity along a vibrating surface.

Another approach to determine the scattering from a three-dimensional (3D) array of inclusions is Foldy's multiple scattering method [23]. This popular approach, applicable to only low frequency scattering, employs a self-consistent technique to determine the unknown amplitude of the scattered waves. Despite the simplicity of the approach, the solution for the scattered wave relies on a matrix with size equal to the square of the number of scattering objects, thus the technique scales poorly with large systems. Hence, exploitation of the inclusion periodicity using an analytical treatment can be used to enhance accuracy and algorithm efficiency of the scattering solution.

Recent work by Laude *et al.* [49] has examined the reflection of an incident plane wave from a two-dimensional (2D) semi-infinite phononic crystal by considering an expansion in terms of the Bloch waves (termed Bloch wave expansion, BWE) and an expansion of reflected plane waves. Laude *et al.* [49] did not, however, validate their expansion approach of the wave fields with an independent verification study nor explicitly include a crucial group velocity selection criterion. Kulpe *et al.* [42] added a group velocity criterion to the selection of possible Bloch waves for the expansion set and provided several numerical examples and verification. Later, in two dimensions, Kulpe *et al.* [40] combined the HKI with the BWE to accurately predict the external acoustic scattering from 2D finite phononic crystals. The scattering from three-dimensional (3D) phononic crystals was considered via Bloch wave expansion in Ref. [43] and more complicated PCs with disorder and geometric complexity in Ref. [41].

In closing, in the last few decades, there have been many analytical, numerical, and experimental advancements in the study of phononic crystals. One area open to further investigation is the scattering from finite phononic crystals with arbitrary inclusion geometry, crystal geometry, frequency, etc. Several of these topics are addressed within this Thesis in Chapters 2-5.

1.4 Scattering via Bloch wave formalism

In this work, large fish schools will be considered; the size of which will be much larger than the acoustic wavelength whereby an infinitely large medium approximation can be employed. As discussed previously, swimbladder bearing fish swim in a periodic arrangement, with the swimbladders dominating the acoustic response. In this perspective, the Bloch wave formalism will be applied to predicting the acoustic backscattering from a large fish school. For simplicity, and without loss of generality, fish will be considered to have an equilibrium position on a regular simple cubic lattice. Applying the phononic crystal theory to a large fish school enables an accurate and efficient prediction of the scattering from large fish schools.

Note, throughout the Thesis, depending on the context the words 'PC' or 'fish school' will be used to denote the scattering volume. The fish schools necessarily will consider fish arranged in a simple cubic lattice with weak disorder. However, since the theory introduced herein can be applied to general 2D and 3D PCs, or through the formalism discussed herein, fish schools, the use of the words should not illicit confusion. It is emphasized that the fish school is *not considered* to be a perfectly periodic phononic crystal, rather, Bloch formalism is applied to an appropriate unit cell of a fish.

1.5 Contributions to the literature

Overall, this Thesis introduces several topics to the emerging discipline of phononic crystals. In particular the BWE and its use with studying the scattering from finite

PCs. The following list outlines the scientific topics introduced into the literature through the published papers and conference presentations leading to the construction of the Thesis. This list is not complete, but rather, an overview only.

1. 2D half-space BWE selection criterion leading to a correct expansion; verification vs. FEM
2. 3D half-space BWE and verification vs. SCS
3. 2D and 3D layer BWE for PCs with a finite thickness
4. Scattering, and verification, from 2D and 3D PCs using the BWE integrated with the HKI
5. Bloch formalism applied, in 2D and 3D, to phononic crystals with weak internal disorder
6. The 3D BWE applied to PCs with arbitrary shape via a facet formalism
7. Bloch formalism applied to efficiently studying the scattering from large fish schools

All of the above items will be discussed throughout this work. As indicated, there is need to study the scattering from phononic crystals. Thus, the content presented in this Thesis provides a dual purpose: the study from fish schools using the Bloch wave formalism, and more generally, the study of scattering from finite phononic crystals of arbitrary shape.

1.6 Outline of the thesis

In the following Thesis, Bloch wave formalism will be introduced in order to accurately predict the scattering from a model fish school. Since the fish school considered herein contains fish arranged in a simple cubic arrangement, a simple cubic model of a two-dimensional and three-dimensional bubble will be considered. In Ch. 2 the Bloch wave expansion formalism will be introduced for the 2D system. Verification and parametric studies will be presented. In Ch. 3 the 3D BWE will be extended from its 2D counterpart. Verification studies and an overview of the SCS technique will also be presented. Next, in Ch. 4 the BWE will be used along with the HKI to study scattering (both monochromatic and transient scattering) from 2D and 3D finite phononic crystals. Verification is presented using the requisite FEM and SCS techniques. A formalism is also presented for PCs of arbitrary (i.e. non-cubic) geometries. Since, obviously, fish schools exhibit disorder, Ch. 5 discusses the role of the BWE and HKI when applied to predicting scattering from disordered systems. Lastly, in Ch. 6 the full Bloch wave formalism is put together to study scattering from fish schools. In closing, the Thesis concludes with a summary and recommendations for future work in Ch. 7.

CHAPTER II

BLOCH WAVE EXPANSION IN TWO DIMENSIONS

2.1 Overview

In this chapter the two-dimensional BWE will be discussed. As mentioned in Ch. 1, Laude *et al.* [49] introduced the concept of the BWE to study the reflection and transmission from a semi-infinite PC half-space. Herein, a new dispersion technique will be introduced and verified. Next, the half-space BWE will be improved upon; a layer BWE will be introduced. The chapter is closed with several verification studies demonstrating the accuracy of the technique.

2.2 Two-dimensional phononic crystal

The prototypical two-dimensional PC under study is displayed in Fig. 3a. This PC is composed of an arbitrary number of inclusions periodically spaced with period a_1, a_2. A representative unit cell is depicted in Fig. 3b: a cell centered inclusion within the PC background. The unit cell has lengths a_j $(j = 1, 2)$ and R is the radius of the cell-centered inclusion, ρ is the density, and c is the sound speed of the background (subscript 1) and inclusion material (subscript 2). For the sake of simplicity, a two-dimensional square unit cells $(a_1 = a_2 = a)$ with circular cell-centered inclusions is considered in this chapter. The theory in this chapter can be extended in a straight forward manner to non-square unit cells through a lattice transformation [25]. Additionally, the circular inclusion is chosen for simplicity; the theory is general and, via the finite element method, arbitrary shaped inclusions can be considered.

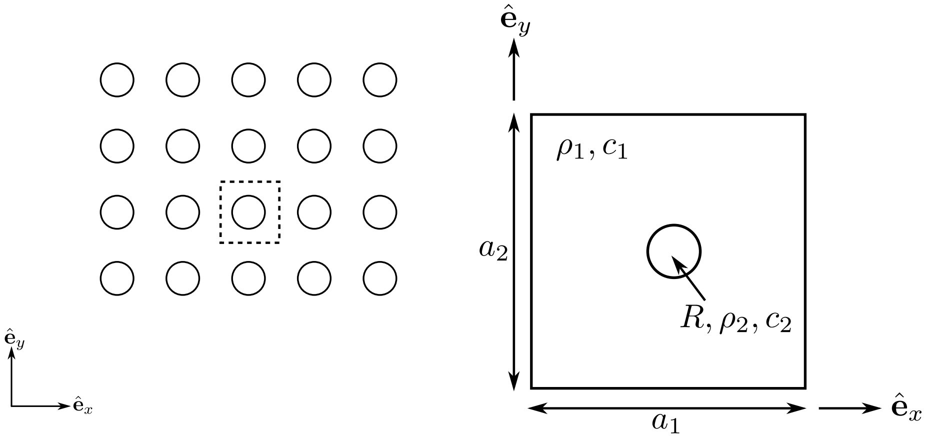

(a) (b)

Figure 3: (a) A typical two-dimensional phononic crystal. A typical unit cell is outlined in the box. (b) A single unit cell is highlighted with periodicity a_1 and a_2 in the $\hat{\mathbf{e}}_x$, $\hat{\mathbf{e}}_y$, directions, respectively, and a cell-centered circular inclusion.

2.3 The Bloch theorem

In a 2D periodic PC the Bloch theorem [34] states that everywhere in the medium the pressure field $p(\mathbf{x}, t)$ takes the form of a function $\tilde{p}(\mathbf{x})$, hereby termed a wave mode, that is periodic on the unit cell and modulated by a harmonic plane wave of frequency ω

$$p(\mathbf{x}, t) = \tilde{p}(\mathbf{x}) e^{i(\mathbf{k}\cdot\mathbf{x} - \omega t)}. \tag{1}$$

In fact, every field quantity in the PC obeys a similar relationship. From this point onward, the time t will be suppressed as it is understood that all wave fields are monochromatic. The Bloch wavevector $\mathbf{k}$ is related to ω by a dispersion relationship. Periodicity of the PC imposes periodicity of the real wavenumber space (reciprocal k-space), shown in Fig. 4a, where $b_j = 2\pi/a_j$ is the length of the cell in k-space. For notational clarity let subscript j = 1,2 (or x, y) correspond to a length or vector component. Unique Bloch waves are found with real part components in the range $-\pi/a_j \leq k_j \leq \pi/a_j$, an extent termed the first Brillouin zone, where k_j is the j^{th} component of the wavevector. However, the imaginary components of the wavevector are unbounded [48, 30]. For clarity propagating Bloch waves are defined as having a purely real wavevector, evanescent Bloch waves as having a purely imaginary wavevector, and decaying Bloch waves as having complex wavevectors. Implicit in this field representation is that there is an infinite number of Bloch waves $p(\mathbf{x}, t)$ each with corresponding wavevector $\mathbf{k}$ that satisfy the Bloch theorem of Eq. (1) and the acoustic wave equation. Hence, at a fixed frequency and direction in k-space there are a finite number of propagating waves, due to the limitations imposed by the Brillouin zone, yet an infinite set of decaying and evanescent waves.

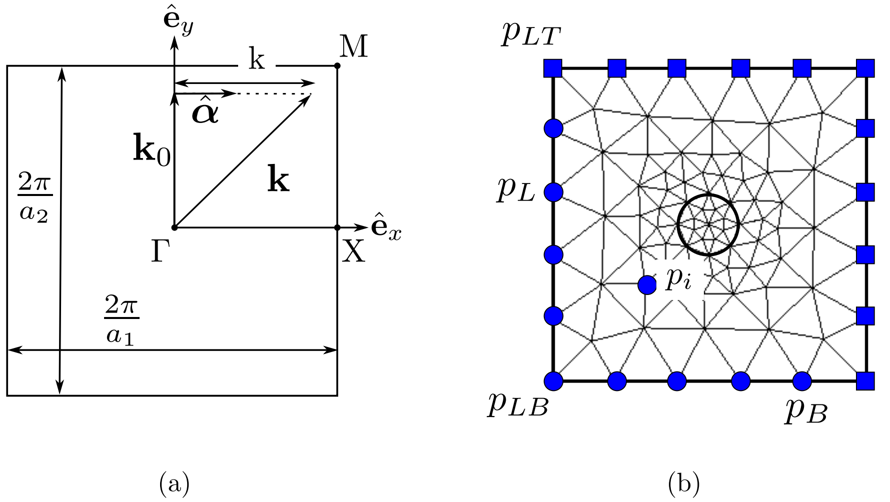

(a) (b)

Figure 4: (a) The first Brillouin zone, in wavenumber k-space, for a 2D unit cell. (b) A representative finite element mesh of a single unit cell with reduced nodal degrees of freedom depicted as dots. The nodal degrees of freedom represented by squares are related by periodic boundary conditions via matrix $\mathbf{T}$. p_i is one node contained within the set $\mathbf{p}_i$.

The complex waves of a PC constitute a complete basis and justify a wave expansion; see Appendix A for more details. Decaying and evanescent Bloch waves are necessary near the boundary of the incident medium and account for the near field wave refraction behavior [48]. Traditional methods for solving the dispersion relation for a particular phononic crystal involve specifying real $\mathbf{k}$ and finding ω as an eigenvalue. See the Appendix B and the papers [46, 66, 19] for a review of this method. The dispersion relationship of the PC considered here is shown in Fig. 8. The ex-

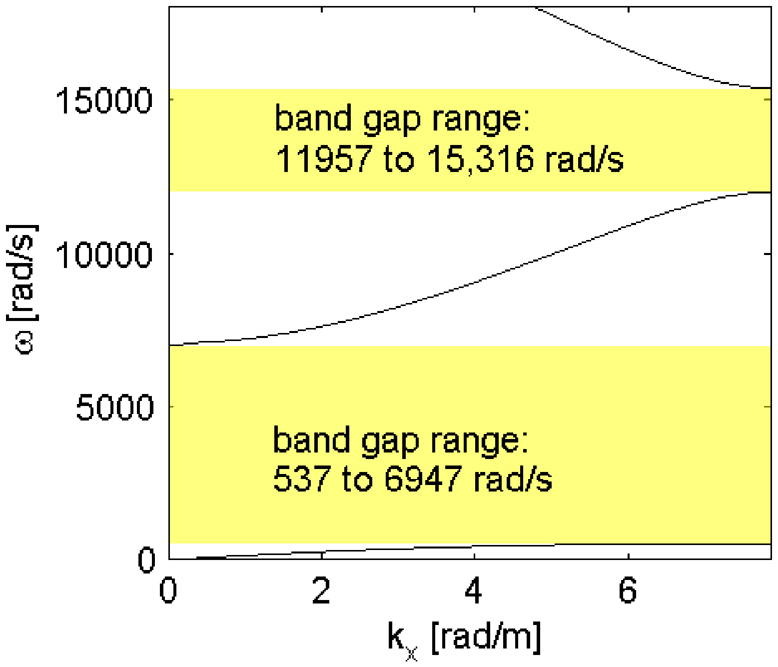

Figure 5: Dispersion relationship for the PC considered in this chapter. The y wavenumber is fixed to zero. The band gap ranges are indicated.

ponentially decaying and evanescent Bloch waves and the associated band structure are not revealed by these $\omega(\mathbf{k})$ methods [47], as $\mathbf{k}$ is restricted to be real. A different $\mathbf{k}(\omega)$ method will be introduced, for complex $\mathbf{k}$, with specific application to wave transmission into the PC half-space.

2.4 Dispersion relationship

2.4.1 Derivation of a new technique

Next, a method is presented which uses the FEM to form equations leaving a single parameter $\mathbf{k}$ as a *complex* eigenvalue and the discretized mode vector $\mathbf{p}$ as an eigenvector for a particular frequency ω. The method presented here is formulated specifically to easily obtain assembled FEM matrices from commercial software, such as COMSOL Multiphysics. Through the finite element method, this dispersion technique remains quite general and can adequately accommodate an arbitrary fluid inclusion.

Starting with the Helmholtz wave equation, with periodically varying density $\rho(\mathbf{x})$ and sound speed $c(\mathbf{x})$

$$\frac{-\omega^2}{\rho(\mathbf{x})c(\mathbf{x})^2}p(\mathbf{x}) - \nabla \cdot \left(\frac{1}{\rho(\mathbf{x})} \nabla p(\mathbf{x}) \right) = 0. \tag{2}$$

In this Thesis, the functions $\rho(\mathbf{x})$ and $c(\mathbf{x})$ are equal to constant values ρ_1 and c_1 for the water host ($\rho_1 = 1000$ kg/m^3 and $c_1 = 1500$ m/s) and ρ_2, c_2 and for the circular inclusion with radius R, as indicated in Fig. 3b. Insertion of the Bloch theorem Eq. (1) and simplification results in

$$-\nabla \cdot \left[\frac{1}{\rho} \left(\nabla \tilde{p} + i\mathbf{k}\tilde{p} \right) \right] - \frac{1}{\rho} \left[i\mathbf{k} \cdot \nabla \tilde{p} - (\mathbf{k} \cdot \mathbf{k})\tilde{p} \right] - \frac{\omega^2}{\rho c^2} \tilde{p} = 0. \tag{3}$$

Using triangular quadratic Lagrange elements, a finite element model of Eq. (3) is sought after. Multiplication by a test function $\psi(\mathbf{x})$ and integration over the unit cell results in

$$\int_{cell} \left\{ \nabla \psi \cdot \left[\frac{1}{\rho} \left(\nabla \tilde{p} + i\mathbf{k}\tilde{p} \right) \right] - \frac{\psi}{\rho} \left[i\mathbf{k} \cdot \nabla \tilde{p} - (\mathbf{k} \cdot \mathbf{k})\tilde{p} \right] - \frac{\omega^2}{\rho c^2} \psi \tilde{p} \right\} d\mathrm{V} = 0. \tag{4}$$

In anticipation of the follow-on development, and without loss of generality, the right hand side boundary integral terms in Eq. (4) resulting from application of the divergence theorem (see discussion following Eq. (8)) are zeroed. Tessellating the domain with triangular elements and invoking a Galerkin discretization of the pressure field $\tilde{p}$ and test function $\psi(\mathbf{x}) \rightarrow \psi_m(\mathbf{x})$ using quadratic Lagrange interpolation functions results in five elemental matrices with components

$$M_{mn}^{element} = \int_V \frac{1}{\rho c^2} \psi_m \psi_n \mathrm{d}V \tag{5a}$$

$$K_{mn}^{element} = \int_V \frac{1}{\rho} \nabla \psi_m \cdot \nabla \psi_n \mathrm{d}V \tag{5b}$$

$$B_{mn}^{element} = \int_V \frac{1}{\rho} \psi_m \psi_n \mathrm{d}V \tag{5c}$$

$$A_{mn,x}^{element} = \int_V \frac{1}{\rho} \left(\psi_n \frac{\partial \psi_m}{\partial x} - \psi_m \frac{\partial \psi_n}{\partial x} \right) \mathrm{d}V \tag{5d}$$

$$A_{mn,y}^{element} = \int_V \frac{1}{\rho} \left(\psi_n \frac{\partial \psi_m}{\partial y} - \psi_m \frac{\partial \psi_n}{\partial y} \right) \mathrm{d}V. \tag{5e}$$

Here $m, n = 1$ to 6 for quadratic triangular elements, corresponding to the individually numbered nodes of an element, and V is the volume of an element. The six interpolation functions ψ_m can be found in a typical finite element textbook [72]. Assembly of the elemental matrices Eq. (5) over all elements in the domain results in five assembled global matrices $\mathbf{M}, \mathbf{K}, \mathbf{B}, \mathbf{A}_x, \mathbf{A}_y$ and the equations of motion read

$$\left(-\omega^2\mathbf{M} + \mathbf{K} + ik_x\mathbf{A}_x + ik_y\mathbf{A}_y + (\mathbf{k}\cdot\mathbf{k})\mathbf{B}\right)\mathbf{p} = \mathbf{0}. \tag{6}$$

Dispersion techniques leaving the periodic mode vector $\mathbf{p}$ as an eigenvector require periodic boundary conditions [49]. Unit cell periodicity implies that the nodal degrees of freedom on the bottom “B” are equal to the nodal degrees of freedom on the top “T” ($\mathbf{p}_B = \mathbf{p}_T$), the left “L” to the right “R”, etc (see Fig. 4b). Implementation of periodic boundary conditions is easily achieved using a transformation matrix $\mathbf{T}$ [46, 66, 19] by preferential ordering of the nodal degrees of freedom in the global nodal vector $\mathbf{p}$, with $\mathbf{p}_I$ referring to all nodes on the mesh interior. The reduced set of unique nodal values is contained in the vector $\tilde{\mathbf{p}}$ (note: the choice of the left and bottom degrees of freedom in the reduced set is arbitrary) which is related to the vector $\mathbf{p}$ by

$$\mathbf{p} = \mathbf{T}\tilde{\mathbf{p}} \tag{7a}$$

$$\tilde{\mathbf{p}} = \begin{bmatrix} \mathbf{p}_L \\ \mathbf{p}_B \\ \mathbf{p}_{LB} \\ \mathbf{p}_I \end{bmatrix} \tag{7b}$$

$$\mathbf{T} = \begin{bmatrix} \mathbf{I} & \mathbf{0} & \mathbf{0} & \mathbf{0} \\ \mathbf{I} & \mathbf{0} & \mathbf{0} & \mathbf{0} \\ \mathbf{0} & \mathbf{I} & \mathbf{0} & \mathbf{0} \\ \mathbf{0} & \mathbf{I} & \mathbf{0} & \mathbf{0} \\ \mathbf{0} & \mathbf{0} & \mathbf{I} & \mathbf{0} \\ \mathbf{0} & \mathbf{0} & \mathbf{I} & \mathbf{0} \\ \mathbf{0} & \mathbf{0} & \mathbf{I} & \mathbf{0} \\ \mathbf{0} & \mathbf{0} & \mathbf{I} & \mathbf{0} \\ \mathbf{0} & \mathbf{0} & \mathbf{0} & \mathbf{I} \end{bmatrix} \tag{7c}$$

where $\mathbf{I}$ and $\mathbf{0}$ are identity and zero block matrices. The periodic boundary conditions are imposed on the equations of motion in Eq. (6) by premultiplication of $\mathbf{T}^T$ and substitution of Eq. (7) yielding

$$\left(-\omega^2\tilde{\mathbf{M}} + \tilde{\mathbf{K}} + ik_x\tilde{\mathbf{A}}_x + ik_y\tilde{\mathbf{A}}_y + (\mathbf{k}\cdot\mathbf{k})\tilde{\mathbf{B}}\right)\tilde{\mathbf{p}} = \mathbf{0} \tag{8}$$

where $\tilde{\mathbf{M}} = \mathbf{T}^T\mathbf{M}\mathbf{T}$, $\tilde{\mathbf{K}} = \mathbf{T}^T\mathbf{K}\mathbf{T}$, etc. and the superscript T denotes a matrix transpose. Note, to avoid confusion, other authors [46, 66, 19] use $\mathbf{T}(\mathbf{k})$ as the transformation matrix; the use herein corresponds to their $\mathbf{T}(\mathbf{0})$. The FEM right hand side boundary terms for the cell, omitted in Eq. (4), equate to zero after premultiplication by the matrix $\mathbf{T}^T$ [19]. Lastly, note, that all five of the preceding matrices depend *only* on geometry and acoustic properties. Thus, for a particular geometry, for implementation efficiency, the matrices can be loaded from a pre-computed set. This property can be exploited, for instance, in parametric studies involving ω.

2.4.2 Implementation in COMSOL

The five preceding FEM matrices can be created automatically via finite element method commercial software. In particular, throughout this work, COMSOL Multiphysics is used extensively as this software enables scripting via MATLAB and easy extraction of the matrices from Eq. (8). As such, this section pertains explicitly to COMSOL; other commercial software or in-house codes can alternatively be used to create and assemble the five matrices necessary for the dispersion calculations.

In the partial differential equation (PDE) interface in COMSOL [11], a general PDE is defined as

$$-\omega^2 e_a^c u^c - \nabla \cdot (d^c \nabla u^c) - \nabla \cdot (\hat{\boldsymbol{\alpha}}^c u^c) + \hat{\boldsymbol{\beta}}^c \cdot \nabla u^c + a^c u^c = 0 \tag{9}$$

where the 'c' superscript is given to the COMSOL variables (which are space and frequency dependent in general) and to avoid confusion with other quantities. Comparison of the preceding equation and Eq. (3) reveals that:

$$e_a^c = \frac{1}{\rho c^2} \tag{10a}$$

$$d^c = \frac{-1}{\rho} \tag{10b}$$

$$\hat{\boldsymbol{\alpha}}^c = \frac{-i\mathbf{k}}{\rho} \tag{10c}$$

$$\hat{\boldsymbol{\beta}}^c = \frac{i\mathbf{k}}{\rho} \tag{10d}$$

$$a^c = \frac{-k^2}{\rho} \tag{10e}$$

$$u^c = \tilde{p} \tag{10f}$$

Within the COMSOL software, Eq. 9 can be solved using a Galerkin discretization and the following equation is formed

$$\left[-\omega^2 \mathbf{M}^c + \mathbf{K}^c\right] \mathbf{u}^c = \mathbf{0}. \tag{11}$$

where $\mathbf{M}^c, \mathbf{K}^c$ are the mass and stiffness matrices generated within COMSOL from the Galerkin discretization of Eq. (9) and $\mathbf{u}^c$ is the vector of unknown nodal values of u^c. After the user inputs the numerical values of Eq. (10) using the geometry and mesh, respectively, described by Fig. 3b and Fig. 4b the mass and stiffness matrices can be exported to MATLAB. Of note also, since the model must be periodic, the mesh's nodes must be enforced to be periodic on the edges of the model; COMSOL possess this enforcement feature.

Given the two COMSOL matrices of Eq. (11), the next step is to determine the five matrices appearing in Eq. (8). Firstly, by direct comparison, it is found that $\mathbf{M}^c = \mathbf{M}$. Secondly, because of the similarity of $\mathbf{M}$ and $\mathbf{B}$ from Eq. (5), $\mathbf{B}$ be found by imposing an artificial density $\rho^c = \rho c^2$ and extracting the new COMSOL mass matrix $\mathbf{M}^c \rightarrow \mathbf{B}$.The matrices $\mathbf{K}, \mathbf{A}_x \mathbf{A}_y$ can be identified by specifying the values of k_x, k_y to be zero or one in the COMSOL variables of Eq. (10). This is a three step procedure: specify the value of k_j, assemble and extract the matrix $\mathbf{K}^c$ then follow

$$k_x = 0, k_y = 0, \mathbf{K} = -\mathbf{K}^c \tag{12a}$$

$$k_x = 1, k_y = 0, \mathbf{A}_x = i\left(\mathbf{K}^c + \mathbf{K} + \mathbf{B}\right) \tag{12b}$$

$$k_x = 0, k_y = 1, \mathbf{A}_x = i\left(\mathbf{K}^c + \mathbf{K} + \mathbf{B}\right) \tag{12c}$$

It is noted, this is purely a 'trick' to efficiently extract the matrices of interest from COMSOL into the desired form of Eq. (8).

2.4.3 Solution of the eigenvalue problem

Transformation of Eq. (8) to a scalar eigenvalue problem requires a wavevector parametrization leaving a single parameter k as an eigenvalue. To this end, $\mathbf{k}$ is written as

$$\mathbf{k} = \mathbf{k}_0 + k\hat{\boldsymbol{\alpha}} \tag{13}$$

and leave the vectors $\mathbf{k}_0$ and $\hat{\boldsymbol{\alpha}}$ as problem specific parameters; see Fig. 4a and Ref. [47]. This general scheme allows the complex dispersion relationship to be calculated along any direction $\hat{\boldsymbol{\alpha}}$ in k-space. Inserting Eq. (13) and manipulation of the equations of motion Eq. (8) results in a quadratic eigenvalue problem for the dispersion relationship with eigenvalue k and eigenvector (corresponding to the Bloch mode) $\tilde{\mathbf{p}}$.

$$\left(\mathbf{D}'(\omega) + k\mathbf{A}' + k^2\mathbf{B}'\right)\tilde{\mathbf{p}} = \mathbf{0} \tag{14}$$

where

$$\tilde{\mathbf{D}}(\omega) = -\omega^2\tilde{\mathbf{M}} + \tilde{\mathbf{K}} \tag{15a}$$

$$\mathbf{D}'(\omega) = \tilde{\mathbf{D}}(\omega) + i\left(k_{0x}\tilde{\mathbf{A}}_x + k_{0y}\tilde{\mathbf{A}}_y\right) + k_0^2\tilde{\mathbf{B}} \tag{15b}$$

$$\mathbf{A}' = i\left(\alpha_x\tilde{\mathbf{A}}_x + \alpha_y\tilde{\mathbf{A}}_y\right) \tag{15c}$$

$$\mathbf{B}' = \alpha^2\tilde{\mathbf{B}}. \tag{15d}$$

Note that the matrices $\tilde{\mathbf{M}}, \tilde{\mathbf{K}}, \tilde{\mathbf{B}}$ are symmetric and $\tilde{\mathbf{A}}_j$ is not, therefore the eigenvalues of Eq. (14) are not guaranteed to be real and positive. Numerical solution efficiency is obtained by converting the quadratic eigenvalue problem, of size N_R x N_R (N_R being the size of the square matrices appearing in Eq. (14)) to a generalized eigenvalue problem of size $2N_R$ x $2N_R$ by introducing $\tilde{\mathbf{u}} = k\tilde{\mathbf{p}}$ and writing

$$(\mathbf{S} - k\mathbf{G})\begin{bmatrix}\tilde{\mathbf{p}}\\ \tilde{\mathbf{u}}\end{bmatrix} = \mathbf{0} \tag{16}$$

$$\mathbf{S} = \begin{bmatrix}\mathbf{0} & \mathbf{I}\\ -\mathbf{D}'(\omega) & -\mathbf{A}'\end{bmatrix} \tag{17a}$$

$$\mathbf{G} = \begin{bmatrix}\mathbf{I} & \mathbf{0}\\ \mathbf{0} & \mathbf{B}'\end{bmatrix}. \tag{17b}$$

The finite element matrices are typically sparse and efficiency is obtained by using any one of the sparse eigenvalue solution routines. Solution of the discretized generalized eigenvalue problem Eq. (16) leads to a finite set of periodic Bloch modes and, possibly, complex wavenumbers k. The Bloch wavevector $\mathbf{k}$ is reconstituted from the eigenvalue k by Eq. (13). An iterative solution for many values of ω will lead to a $\mathbf{k}(\omega)$ dispersion relation for the arbitrary 2D PC, in any direction $\hat{\boldsymbol{\alpha}}$.

The eigenvalue problem previously outlined is perfectly general, given the vectors $\mathbf{k}_0$ and $\hat{\boldsymbol{\alpha}}$, and can be tailored to identify Bloch waves for a transmitted field expansion. The geometry of the reflection-transmission problem is shown in Fig. 6 where a semi-infinite 2D PC half-space is adjacent to a homogenous water medium with density ρ_i and sound speed c_i. For reflection-transmission problems the parallel wavevector component must be conserved along the PC interface [34, 49]. A set of Bloch waves is required in the expansion that have the parallel component equal to a specified constant. Wavenumber conservation along the interface, given by unit vector $\hat{\mathbf{e}}_y$, will be mantained by searching for Bloch waves along a direction $\hat{\boldsymbol{\alpha}} = \hat{\mathbf{e}}_x$ [47]. Note, regardless of the interface's orientation with respect to the coordinate axes, the vector $\hat{\boldsymbol{\alpha}}$ is always parallel to the PC interface normal. The vector $\mathbf{k}_0$ is composed of the parallel component of the incident wavevector, e.g. $\mathbf{k}_0 = [0\ \omega/c_i \sin(\theta)]^T$ where θ

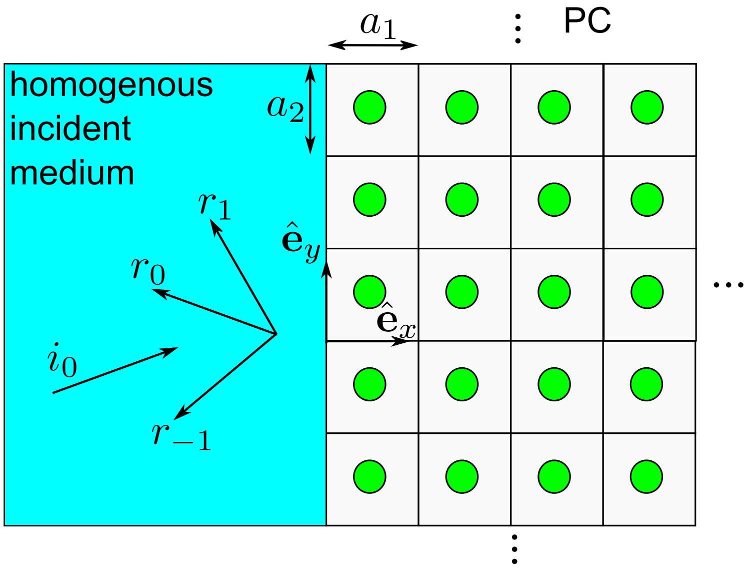

Figure 6: A half-space consisting of a homogenous water medium and a PC. Three reflected wave orders and the incident plane wave are included for an example.

is the incidence angle with respect to the interface normal $\hat{\mathbf{e}}_x$. Note $\mathbf{k}\cdot\hat{\mathbf{e}}_y = const \ \forall\ k$ and therefore the relationship allows for wavenumber conservation along the PC interface. Geometrically this constraint implies searching for Bloch waves along a line, given by Eq. (13) and at fixed ω, through the three-dimensional complex dispersion surface. See Ref. [34] for a further geometrical discussion of the wavevector relationship.

Calculation of the group velocity for a particular Bloch wave can be directly obtained from the eigenvalue problem of Eq. (16). First Eq. (16) is written as $\mathbf{W}(\omega)\mathbf{q} = k\mathbf{q}$ where $\mathbf{W}(\omega) = \mathbf{G}^{-1}\mathbf{S}(\omega)$ and $\mathbf{q} = [\tilde{\mathbf{p}} \ \ \tilde{\mathbf{u}}]^T$ is a right eigenvector of $\mathbf{W}$. The derivative of the n-th eigenvalue k_n with respect to ω can be obtained [82] as

$$\frac{\partial k_n}{\partial \omega} = \mathbf{h}_n^H \frac{\partial \mathbf{W}(\omega)}{\partial \omega}\mathbf{q}_n \tag{18}$$

where now the vector $\mathbf{h}_n^H$ is the n-th left eigenvector of $\mathbf{W}$ and is scaled such that $\mathbf{h}_n^H\mathbf{q}_n = 1$. Here the superscript H denotes the matrix Hermitian operation. Finally, the group velocity for the n-th Bloch wave into the PC medium $\mathbf{c}_{gn}\cdot\hat{\mathbf{e}}_x$ is obtained by

$$\mathbf{c}_{gn}\cdot\hat{\mathbf{e}}_x = \mathrm{Re}\left[\left(\frac{\partial k_n}{\partial \omega}\right)^{-1}\right] = \mathrm{Re}\left[\left(\mathbf{h}_n^H \begin{bmatrix} \mathbf{0} & \mathbf{0} \\ -\mathbf{B}'^{-1}\frac{\partial}{\partial\omega}\mathbf{D}'(\omega) & \mathbf{0} \end{bmatrix} \mathbf{q}_n\right)^{-1}\right]. \tag{19a}$$

$$\frac{\partial}{\partial\omega}\mathbf{D}'(\omega) = -2\omega\tilde{\mathbf{M}} + i\frac{\sin\theta}{c_i}\tilde{\mathbf{A}}_y + \frac{2\omega\sin^2\theta}{c_i^2}\tilde{\mathbf{B}}' \tag{19b}$$

With the two preceding equations the group velocity can be efficiently determined after solution of the eigenvalue problem in Eq. (16).

This section is closed with a fact regarding PCs with viscous fluids. Alternatively, a different $\omega(\mathbf{k})$ technique can be considered for PCs with viscous fluids [18, 32, 61]. The dispersion technique introduced herein is suitable for use with viscous fluids; see Appendix D. With the introduction of the frequency dependent matrices, the group velocity calculations must be modified. Since the dispersion relationship is not appreciably changed much by the introduction of viscous PCs (the viscosity properties are representative of those measured in fish), only ideal PCs will be considered in the rest of this research effort.

2.4.4 Verification

Up to this point, a technique has been formulated for easy implementation in commercial finite element programs. To verify the preceding dispersion technique the system parameters are set to $\{a_1 = a_2 = 1$ m, $R = 0.4$ m, $\rho_2 =$ 7,800 kg/m^3, $c_2 =$ 4,591 m/s, $\hat{\boldsymbol{\alpha}} = 1/\sqrt{2}[1\ 1]^T$, $\mathbf{k}_0 = \mathbf{0}\}$. This parameter choice allows direct comparison for the complex dispersion relationship from Laude *et al.* (see Fig. 6 in their work) [49]. Inspection of the results in Fig. 7 show that the dispersion curves calculated from the present technique agree very well with that reported in the literature.

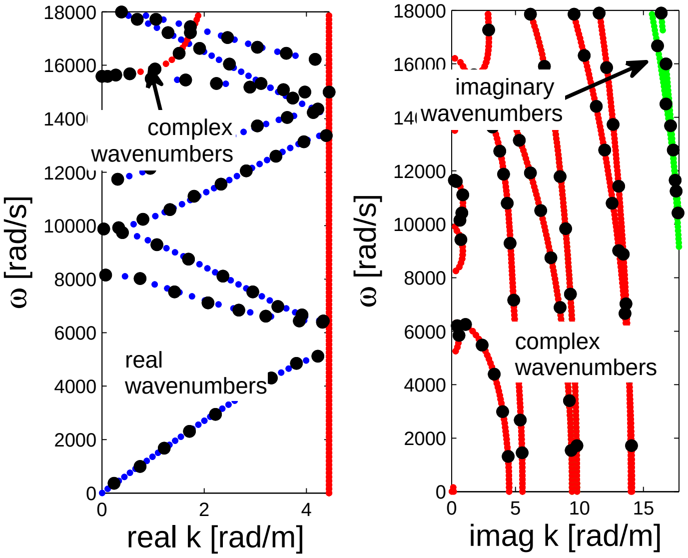

Figure 7: Verification of the complex dispersion relation for a circular steel rod in water. The large dots represent the dispersion relationship from Ref. [49] (see Fig. 6 in their work). The real wavenumbers, imaginary wavenumbers, and complex wavenumbers (small dots) were found by the dispersion technique demonstrated in this Thesis.

In the dispersion diagram of Fig. 7 the wavenumbers are displayed (as small dots) according to the real and imaginary parts. The results here indicate most decaying wavenumbers have a real component equal to $\sqrt{2}\pi/a$ (denoted as the M point in the first Brillouin zone [34]). At frequencies over 16,000 rad/s there is a branch with wavenumbers of complex values; these are wavenumbers not easily identified by a conventional $\omega(\mathbf{k})$ search method.

2.5 Half-space BWE

In this section the use of a Bloch wave expansion to model the transmitted wave field in a PC half-space is detailed. The dispersion technique discussed in Sec. 2.4.1 will be used to identify the Bloch waves needed to compose the expansion for a particular choice of frequency and incidence wave angle. The expansion equations and solution procedure are taken from the work of [49] and are repeated here for completeness. However, an additional constraint pertaining to wave group velocity for mode selection, is added. Additionally, a discussion of the mode selection and associated energy calculations quantifying the amount of acoustic energy reflected from the PC half-space is added. The PC considered consists of air inclusions with R = 2 cm, $\rho_2 = 1.22$ kg/m^3, and $c_2 = 343$ m/s in a water host medium with $a_1 = a_2$ = 40 cm. The physical parameters chosen correspond to the parameters discussed in Ref. [39].

Consider an incident harmonic plane wave $p_i(\mathbf{x}, t)$ propagating at frequency ω in a homogenous incident medium with density and speed (ρ_i = 1500 m/s and c_i = 1000 kg/m^3) and with wavevector $\mathbf{k}_i$ and angle θ relative to the PC normal, with θ = 0 corresponding to normal incidence. Standard boundary conditions for reflection problems apply: conservation of frequency and parallel wavevector, and the matching of pressure and normal particle velocity at the interface [67]. Recall the discussion in Sec. 2.4.1 pertaining to discussion of the choice of the parallel wavevector.

To begin identifying the Bloch waves that compose the transmitted wave field the dispersion relationship, outlined previously, is solved for a particular unit cell giving a set of Bloch wavevectors and modes. Solving Eq. (16) produces many eigenvalues and eigenvectors to choose from. A few notes are in order regarding the numerical solution of Eq. (16). First, a $\mathbf{k}(\omega)$ method does not automatically obey periodicity of the reciprocal k-space [47]. Unique Bloch waves can be identified by selecting waves with the real part within the first Brillouin zone: $-\pi/a \leq \text{Re } k \leq \pi/a$ [47]; no constraint is placed on the magnitude of the imaginary part of the wavevector. Secondly, eigenvalues k which would produce an exponentially growing Bloch wave are discarded. Thirdly, all propagating waves are chosen such that the wave's group velocity vector $\mathbf{c}_g$ satisfies

$$\mathbf{c}_g \cdot \hat{\mathbf{e}}_x > 0. \tag{20}$$

The group velocity vector always lies in the same direction as the acoustic intensity vector averaged over the unit cell [87]. Therefore, the constraint in Eq. (20) implies that at steady state acoustic power flows into the PC medium [34]. Identified propagating Bloch waves that do not satisfy this third criteria are discarded. This group velocity condition places a wavenumber selection criterion on $\pm k$ for some real wavenumber k. Symmetry of the dispersion relation about the vertical frequency axis implies a choice, based on group velocity, of real wavenumbers from a pair of wavenumbers.

Through the discretized eigenvalue problem, after considering the three solution criteria, there are N Bloch waves and wavevectors; often in practice $N \ll N_R$ where N_R is the number of degrees of freedom from the FEM discretization in Eq. (8). The following outline is helpful in summarizing the method of Bloch wave selection

1. Compute the dispersion relation, as defined in Sec. 2.4.1, for a chosen ω and θ
2. Numerically evaluate Eq. (16) for Bloch wavevectors and waves and and Eq. (19) for determining group velocity into the PC half-space
3. Remove very small erroneous real and imaginary wavenumber parts, left as

numerical artifacts

4. Select any and all propagating Bloch waves with $\mathbf{c}_g \cdot \hat{\mathbf{e}}_x > 0$ and $-\pi/a \leq \text{Re } k \leq \pi/a$

5. Select any and all, subject to a predefined maximum decay rate, decaying and evanescent Bloch waves such that the wave exponentially decays in a direction away from the interface

This set of waves constitute the Bloch expansion set.

As an example of the Bloch wave selection, consider identifying suitable Bloch waves for the expansion at normal incidence at three frequencies. As described in Sec. 2.4.1 Bloch waves with a conserved wavenumber can be found along a horizontal line at frequency ω, parametrized by k. Figure 8 depicts the complex dispersion diagram at normal incidence with lines drawn at $\omega = 5000$, 10000, and 18000 rad/s and the selected Bloch waves indicated by squares. At 5000 rad/s there are no propagating Bloch waves and only decaying and evanescent Bloch waves constitute the expansion basis. At 10000 rad/s there are two propagating Bloch waves (with wavenumbers at $\pm k$), one being selected (square) and the other being discarded (x) as this Bloch wave's group velocity is directed out of the PC half-space and violates the group velocity selection criterion. Similarly, at 18000 rad/s the propagating Bloch wave on the Re $k < 0$ side of the diagram is chosen as this wave satisfies the group velocity criterion. In practice, additional decaying and evanescent waves would be desired for an accurate expansion; the imaginary wavenumber diagram here is truncated to 20 rad/m for clarity. The above solution procedure applies equally to a variety of incidence angles, each with a corresponding complex dispersion diagram, as further described in Sec. 2.7.

Next, the pressure field in the PC half-space, $p_t(\mathbf{x})$, is written as a summation of

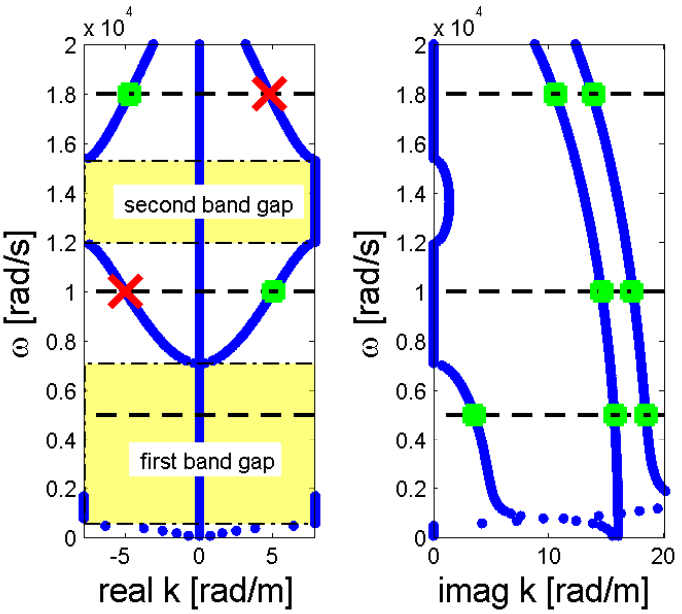

Figure 8: The dispersion diagram for the PC at normal incidence. Horizontal lines at 5,000, 10,000 and 18,000 rad/s. Squares indicate selected Bloch waves. Here a "x" indicates propagating Bloch waves discarded as they radiate energy out of the PC half-space ($\mathbf{c}_g \cdot \hat{\mathbf{e}}_x < 0$). The first two band gaps are denoted by the frequency ranges outlined in shaded boxes.

N Bloch waves

$$p_t(\mathbf{x}) = \sum_{n=1}^{N} t_n p_n(\mathbf{x}) \tag{21}$$

where the modal transmission coefficients t_n are obtained based on the interface boundary conditions. Similarly, the reflected pressure field, $p_r(\mathbf{x}, t)$, is written as an expansion of N plane waves with unknown modal reflection coefficients r_m as

$$p_r(\mathbf{x}) = \sum_{m=-N/2}^{N/2} r_m p_{mr}(\mathbf{x}) \tag{22}$$

where $p_{mr}(\mathbf{x}) = \exp(i\mathbf{k}_m \cdot \mathbf{x})$ represents a reflected plane wave of order m. Periodicity of the unit cell creates a diffraction grating on the interface [49] and therefore the two components of the reflected wavevector $\mathbf{k}_m$ satisfy $k_{my} = k_{iy} + b_2 m$ and $k_{mx} = -\sqrt{(\omega/c_i)^2 - k_{my}^2}$ with $b_2 = 2\pi/a_2$ and integer m. The sign of the square root in k_{mx} is chosen to have reflected propagating or evanescent waves travel away from the PC medium. In Ref. [49] the summation limit N is not explicitly indicated; N reflected waves are chosen such that the analysis yields square matrices for wave amplitudes. This choice of a square matrix system yields a unique solution in the entire field of interest. To determine the modal amplitudes of the N Bloch waves and N reflected wave orders the pressure continuity equations, valid at all times on the interface, are written as

$$p_i\left(0,y\right)+\sum_{m=-N/2}^{N/2} r_m p_{mr}\left(0,y\right)=\sum_{n=1}^{N} t_n p_n\left(0,y\right). \tag{23}$$

An equation enforcing continuity of normal particle velocity in the $\hat{\mathbf{e}}_x$ direction is written as

$$v_{ix}\left(0,y\right)+\sum_{m=-N/2}^{N/2} r_m v_{mrx}\left(0,y\right)=\sum_{n=1}^{N} t_n v_{nx}\left(0,y\right) \tag{24}$$

where from the linearized Euler's relationship the velocities of the incident and reflected plane waves are

$$v_{ix}=\frac{1}{Z_0}p_i \tag{25}$$

$$v_{mrx}=\frac{-1}{Z_m}p_{mr}. \tag{26}$$

The impedance of the m-th plane wave order is given by $Z_m=-\rho_i\omega/k_{mx}$. The particle velocity of the n-th Bloch wave is

$$v_{nx}=\tilde{v}_{nx}\exp\left(i\mathbf{k}_n\cdot\mathbf{x}\right) \tag{27}$$

$$\tilde{v}_{nx}=\frac{1}{i\omega\rho_1}\left(\frac{\partial\tilde{p}_n}{\partial x}+ik_{nx}\tilde{p}_n\right) \tag{28}$$

Note that the Bloch wave velocity in Eq. (28) also satisfies the Bloch theorem.

Solution of the expansion equations for the amplitude coefficients results from multiplication of both equations Eqs. (23) and (24)by $\exp(-ik_{my}y)$ and integration along the boundary of the unit cell to exploit orthogonality of complex exponentials. Following the integration, Eq. (23) reads (in matrix form)

$$\mathbf{i}+\mathbf{r}=\mathbf{M}^p\mathbf{t} \tag{29}$$

and velocity continuity from Eq. (24)

$$\mathbf{Z}^{-1}(\mathbf{i}-\mathbf{r}) = \mathbf{M}^{v}\mathbf{t} \tag{30}$$

where $\mathbf{i}$ is a vector of the incident plane wave order amplitudes ($i_m = \delta_{m0}$) and δ_{mn} is the Kronecker Delta. For compactness, two vectors are defined where

$$\mathbf{t} = [t_1\ t_2\ \ldots t_N]^T \tag{31a}$$

$$\mathbf{r} = [r_{-N/2}\ \ldots r_0\ \ldots r_{N/2}]^T \tag{31b}$$

Also, three matrices [49] with components defined are defined by

$$M^{p}_{mn} = \frac{1}{a_2}\int_0^{a_2} \tilde{p}_n(0,y)\, e^{-imb_2 y}\mathrm{dy} \tag{32}$$

$$M^{v}_{mn} = \frac{1}{a_2}\int_0^{a_2} \tilde{v}_{nx}(0,y)\, e^{-imb_2 y}\mathrm{dy} \tag{33}$$

$$Z_{mn} = Z_m \delta_{mn}. \tag{34}$$

From a mathematical perspective, the m,n element in $\mathbf{M}^p$ (or $\mathbf{M}^v$) represents the Fourier coefficient of the m-th harmonic of the n-th Bloch pressure (velocity) wave. Equations (29) and (30) can then be solved for the wave amplitude vectors as

$$\begin{bmatrix} \mathbf{I} & -\mathbf{M}^p \\ -\mathbf{I} & -\mathbf{Z}_{\mathbf{i}}\mathbf{M}^v \end{bmatrix} \begin{bmatrix} \mathbf{r} \\ \mathbf{t} \end{bmatrix} = \begin{bmatrix} -\mathbf{i} \\ -\mathbf{i} \end{bmatrix} \tag{35}$$

In summary, the solution of Eqs. (35) yields vectors $\mathbf{t}$ and $\mathbf{r}$ which, respectively, contain the Bloch wave and reflected order amplitudes and thereby allow the pressure and velocity fields to be obtained by the modal expansion (e.g. see Eqs. (21) and (22)).

Using the solution for the wave amplitudes a generalized power reflection R_W and transmission T_W coefficients are considered. These quantities describe the power reflected by or transmitted into the PC half-space. Note that these coefficients also depend on the frequency ω and θ. Following the solution for the expansion amplitudes, the time averaged intensity vector fields are defined (* denotes complex conjugation) as

$$\mathbf{I}_t(\mathbf{x}) = \frac{1}{2}\mathrm{Re}\left[p_t(\mathbf{x})\mathbf{v}_t^*(\mathbf{x})\right] \tag{36a}$$

$$\mathbf{I}_r(\mathbf{x}) = \frac{1}{2}\mathrm{Re}\left[p_r(\mathbf{x})\mathbf{v}_r^*(\mathbf{x})\right]. \tag{36b}$$

The reflected and transmitted velocity fields follow from Euler's equation: $\mathbf{v} = (1/i\omega\rho)\nabla p$. The R_W and T_W coefficients are computed by

$$R_W = \frac{S_r}{S_r + S_t} \tag{37a}$$

$$T_W = \frac{S_t}{S_r + S_t} \tag{37b}$$

with

$$S_r = \int_0^{a_2} -\hat{\mathbf{n}} \cdot \mathbf{I}_r(0, y)\,\mathrm{dy} \tag{38a}$$

$$S_t = \int_0^{a_2} \hat{\mathbf{n}} \cdot \mathbf{I}_t(0, y)\,\mathrm{dy}. \tag{38b}$$

Note that by construction, $R_W + T_W = 1$, which is mandated by energy conservation in a lossless medium. If, for a particular frequency and incidence angle θ, there are no propagating Bloch waves then energy must be perfectly reflected back to the incident medium and $R_W = 1$ and $T_W = 0$. This section is closed with mention that, in the simpler problem of reflection/transmission between two homogenous fluids, Eq (37) reduces exactly to the reflection and transmission intensity coefficients given within Ref. [36] (see page 150).

2.6 Layer BWE

In this section the Bloch expansion for a layered phononic medium is introduced. The technique is motivated for study of finite length PCs, for any frequency. This BWE technique, which, to the best of the author's knowledge has not been presented elsewhere, shares many similarities with the half-space BWE. The phononic crystal medium considered is infinite in extent in the $\hat{\mathbf{e}}_y$ direction, but finite in the $\hat{\mathbf{e}}_x$ direction. The layer is composed of an integer number, H, of unit cells; the layer thickness is Ha_1. Since the extent of the PC is included within the model, the layer BWE can be more accurate than the half-space version, especially for non-band gap frequencies, since the PC's finite size effects can be captured. As before, the incident medium ($x \leq 0$) has constant acoustic properties ρ_i, c_i, the PC medium ($0 \leq x \leq Ha_1$) possesses periodic material properties $\rho(\mathbf{x}), c(\mathbf{x})$, and the transmitted medium ($x \geq Ha_1$) has constant acoustic properties ρ_t, c_t. A pictorial diagram is shown in Fig. 9 in which a shifted position vector is introduced for convenience,

$$\mathbf{x}^B = Ha_1\hat{\mathbf{e}}_x - \mathbf{x}. \tag{39}$$

In the traditional analysis of reflection and transmission from a layered medium [36], one expects harmonic waves propagating within a homogenous layer will have the functional form $p(x) = \exp(ikx) + \exp(-ikx)$. In analogy to the homogenous medium, in the phononic crystal layer one can look for two sets of Bloch waves: 'A' waves taking the form $p^A(\mathbf{x}) = \tilde{p}^A(\mathbf{x})\exp(i\mathbf{k}^A \cdot \mathbf{x})$ and 'B' waves taking the form $p^B(\mathbf{x}^B) = \tilde{p}^B(\mathbf{x}^B)\exp(i\mathbf{k}^B \cdot \mathbf{x}^B)$; see Fig. 9. The total pressure field within the PC is posed as a summation of these A and B waves. These A and B waves are, respectively, denoted as forward and backward propagating Bloch waves. The notion of propagation direction is attributed to the direction of the group velocity vector, and not the phase velocity. Identification of the quantities $\mathbf{k}^A$ and $\tilde{p}^A$ proceeds exactly as discussed in Sec. 2.5.

To find the B wave set, first, examine the unit cell in the inset of Fig. 9. Imagine the inset unit cell rotated 180 degrees - it would identically resemble the unit cell in Fig. 3b. Also by the wavenumber conservation principle, the y, z components of the B waves must be conserved throughout the entire PC medium. Hence, to find the quantities $\mathbf{k}^B, \tilde{p}^B$ one would evaluate Eq. (17) for the rotated version of the 'forward' unit cell, but with the input wavenumber parameters $k^B_{iy} = -k_{iy}$. This prescription

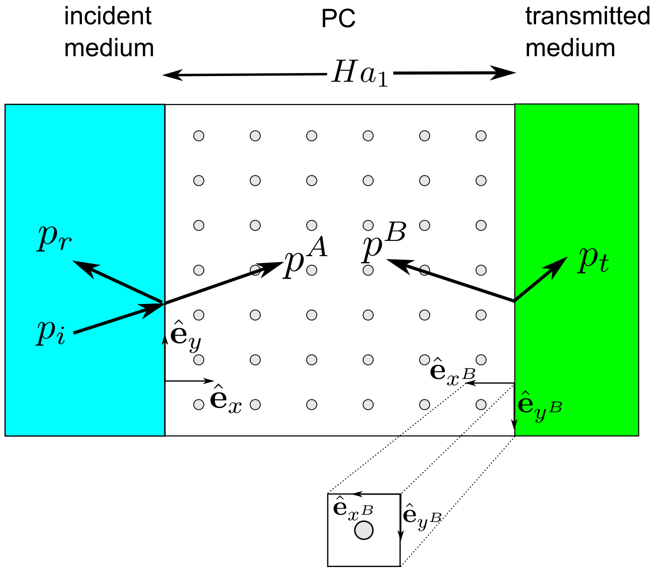

Figure 9: Diagram of the incident medium, phononic crystal layered medium, and transmitted medium. The direction of the incident, reflected, A, B, and transmitted waves is indicated by the arrows. For sake of presentation, only one wavevector is drawn for each respective wave. Note also that all waves possess the same y wavenumber component, equal to k_{iy}. The lower inset depicts the unit cell in the $\hat{\mathbf{e}}_{x^B}$ coordinate system.

of the wavenumber in the B coordinate system is a direct result of the choice of coordinate system from Eq. (39). As before for the A wave set, the waves of the B wave set must decay exponentially ($k_x^B > 0$) and possess group velocity such that $\mathbf{c}_g^B \cdot \hat{\mathbf{e}}_{x^B} = \mathbf{c}_g \cdot \hat{\mathbf{e}}_x > 0$. If the inclusion within the cell is rotationally symmetric, implementation efficiency is achieved since $k_x^B = k_x^A, k_y^B = -k_y^A$ and $\tilde{p}^A(\mathbf{x}) = \tilde{p}^B(\mathbf{x}^B)$; thus, only the values for the A waves need be stored in memory following solution of the eigenvalue problem.

The expansion of the pressure field for the layered system proceeds as before. The reflected field is expanded in plane waves with unknown coefficients r_m as in Eq. (22), except there are, in general, M^r plane waves. The pressure field within the PC is expanded in the A and B waves, with unknown modal coefficients A_n, B_n as

$$p_{layer}(\mathbf{x}) = \sum_{n=1}^{N^A} A_n \tilde{p}_n^A(\mathbf{x})\, e^{i\mathbf{k}_n^A \cdot \mathbf{x}} + \sum_{n=1}^{N^B} B_n \tilde{p}_n^B\left(\mathbf{x}^B\right) e^{i\mathbf{k}_n^B \cdot \mathbf{x}^B} \tag{40}$$

where N_A and N_B are the respective number of A and B Bloch waves used for the expansion. The field within the transmitted medium is also expanded as a set of plane waves, with coefficients t_{lm}, as

$$p_t(\mathbf{x}) = \sum_{m=-M^t/2}^{M^t/2} t_m \exp\left(i\mathbf{k}_{tm} \cdot (\mathbf{x} - Ha_1\hat{\mathbf{e}}_x)\right) \tag{41}$$

where the wavenumbers in the transmitted medium satisfy

$$\begin{aligned} \mathbf{k}_{tm} &= k_{tmx}\hat{\mathbf{e}}_x + k_{my}\hat{\mathbf{e}}_y \\ k_{tmx} &= \sqrt{k_t^2 - k_{my}^2} \end{aligned} \tag{42}$$

and M^t is the number of transmitted plane waves used in the expansion. When the incident and transmitted fluids are equal (as is the case in this Thesis), one can set $N^A = N^B = M^r = M^t$. It is important to note: to maintain wavenumber conservation in the transmitted medium, the incident's wavenumbers k_{iy} appear in Eq. (42) via k_{my}.

The boundary conditions that must be satisfied for the layer, at all y, are: continuity of pressure and normal particle velocity at $x = 0$ and Ha_1. In the manner done in Sec. 2.5, each of the four continuity conditions can be written, and then $\exp -ik_{my}y$ is multiplied by each term and integrated over the unit cell. The pressure and velocity continuity equations at $x = 0$ are written, succinctly in matrix form, as

$$\mathbf{i} + \mathbf{r} = \mathbf{M}^{pA0}\mathbf{A}_n + \mathbf{M}^{pB0}\mathbf{B}_n \tag{43}$$

$$\mathbf{Z}_i^{-1}(\mathbf{i} - \mathbf{r}) = \mathbf{M}^{vA0}\mathbf{A}_n + \mathbf{M}^{vB0}\mathbf{B}_n \tag{44}$$

The continuity relations at $x = Ha_1$ are written as

$$\mathbf{t} = \mathbf{M}^{pAH}\mathbf{A}_n + \mathbf{M}^{pBH}\mathbf{B}_n \tag{45}$$

$$\mathbf{Z}_t^{-1}\mathbf{t} = \mathbf{M}^{vAH}\mathbf{A}_n + \mathbf{M}^{vBH}\mathbf{B}_n. \tag{46}$$

In the preceding four equations, $\mathbf{r}, \mathbf{t}, \mathbf{A}, \mathbf{B}$ are the respective unknown amplitude coefficients of the reflected, transmitted, A waves, B waves; the incident plane wave is $\mathbf{i} = \delta_{m0}$; the impedance matrix for the transmitted medium $\mathbf{Z}_t$ is defined similar to Eq. (34) as

$$Z_{tm} = \rho_t \omega / k_{tmx}. \tag{47}$$

To incorporate the Bloch wave information within the prior continuity equations, eight new matrix quantities are introduced that contain the Fourier series components of the respective Bloch modes. At $x = 0$ the matrices in component form are

$$M_{mn}^{pA0} = \frac{1}{a_2}\int_0^{a_2} \tilde{p}_n^A(0, y) e^{-imb_2 y} \mathrm{dy} \tag{48a}$$

$$M_{mn}^{pB0} = \frac{1}{a_2}\int_0^{a_2} \tilde{p}_n^B(Ha_1, -y) e^{-i(k_{nx}^B Ha_1 + mb_2 y)} \mathrm{dy} \tag{48b}$$

$$M_{mn}^{vA0} = \frac{1}{a_2}\int_0^{a_2} \frac{1}{i\omega\rho_1}\frac{\partial}{\partial x}\left(\tilde{p}_n^A(\mathbf{x}) e^{i\mathbf{k}_n^A\cdot\mathbf{x}}\right) e^{-ik_{my}y} \mathrm{dy} \tag{48c}$$

$$M_{mn}^{vB0} = -\frac{1}{a_2}\int_0^{a_2} \frac{1}{i\omega\rho_1}\frac{\partial}{\partial x^B}\left(\tilde{p}_n^B(\mathbf{x}^B) e^{i\mathbf{k}_n^B\cdot\mathbf{x}^B}\right) e^{-ik_{my}y} \mathrm{dy}. \tag{48d}$$

where here $\mathbf{x} = y\hat{\mathbf{e}}_y$. Similarly, at $x = Ha_1$ the matrices are

$$M_{mn}^{pAH} = \frac{1}{a_2}\int_0^{a_2} \tilde{p}_n^A(Ha_1, y) e^{i(k_{nx}^A Ha_1 - mb_2 y)} \mathrm{dy} \tag{49a}$$

$$M_{mn}^{pBH} = \frac{1}{a_2}\int_0^{a_2} \tilde{p}_n^B(0, -y) e^{-imb_2 y} \mathrm{dy} \tag{49b}$$

$$M_{mn}^{vAH} = \frac{1}{a_2}\int_0^{a_2} \frac{1}{i\omega\rho_1}\frac{\partial}{\partial x}\left(\tilde{p}_n^A(\mathbf{x}) e^{i\mathbf{k}_n^A\cdot\mathbf{x}}\right) e^{-ik_{my}y} \mathrm{dy} \tag{49c}$$

$$M_{mn}^{vBH} = -\frac{1}{a_2}\int_0^{a_2} \frac{1}{i\omega\rho_1}\frac{\partial}{\partial x^B}\left(\tilde{p}_n^B(\mathbf{x}^B) e^{i\mathbf{k}_n^B\cdot\mathbf{x}^B}\right) e^{-ik_{my}y} \mathrm{dy} \tag{49d}$$

where here $\mathbf{x} = Ha_1\hat{\mathbf{e}}_x + y\hat{\mathbf{e}}_y$. One will also note that because of the coordinate system choice for the B waves a negative sign appears in front of M_{mn}^{vB0} and M_{mn}^{vBH}. Note also that M_{mn}^{pA0} and M_{mn}^{vA0} are identical to the quantities defined in Eqs. (32) and (33).

Finally after computing the above quantities for different values of m, n the four interface continuity conditions can be assembled into a large set of linear matrix equations

$$\begin{bmatrix} \mathbf{I} & -\mathbf{M}^{pA0} & \mathbf{0} & -\mathbf{M}^{pB0} \\ -\mathbf{I} & -\mathbf{Z}_i\mathbf{M}^{vA0} & \mathbf{0} & -\mathbf{Z}_i\mathbf{M}^{vB0} \\ \mathbf{0} & -\mathbf{M}^{pAH} & \mathbf{I} & -\mathbf{M}^{pBH} \\ \mathbf{0} & -\mathbf{Z}_t\mathbf{M}^{pvH} & \mathbf{I} & -\mathbf{Z}_t\mathbf{M}^{vBH} \end{bmatrix} \begin{bmatrix} \mathbf{r} \\ \mathbf{A} \\ \mathbf{t} \\ \mathbf{B} \end{bmatrix} = \begin{bmatrix} -\mathbf{i} \\ -\mathbf{i} \\ \mathbf{0} \\ \mathbf{0} \end{bmatrix}. \tag{50}$$

In Eq. (50), all vectors and matrices are partitioned according to the scheme in Eq. (31b) and **0** is a vector or matrix of zeroes of necessary size. Depending on the respective number of waves for the expansions, Eq. (50) can be solved via a least squares solution. Because the Bloch waves used in the expansion are complete, all matrices in Eq. (50) are of full rank; therefore, the least squares solution can be uniquely obtained [24] thus determining the wave amplitudes for the layer problem.

2.7 Verification

In this section the Bloch wave expansion is verified in several test cases using an independent finite element model implemented in COMSOL. To the author's knowledge there is no previous literature presenting a verification of reflected and transmitted pressure fields of a PC by an independent numerical model. Three verification studies will be performed with three different forcing frequencies and incidence angles.

2.7.1 Verification model

Modeling a PC half-space in a finite element model requires a 2D geometry with a large array of air-filled circular inclusions. The half-space model requires non-reflecting boundary conditions on the edges of the workable simulation domain, akin to perfectly matched layers for wave propagation modeling (but which were developed for homogenous media only) [88]. It is essential, to the numerical verification accuracy, to have the damping occur in a PC, and not a homogenous medium as in the case for perfectly matched layers, so additional PC domains and incorporating damping $\xi(x, y)$ that monotonically increases with distance from the workable domain are employed here. The following damping expression was found suitable for the simulated cases to approximate non-reflecting boundary conditions

$$\xi(x,y) = \xi_0 \left(\pm x - H_1 a_1\right)^{s_1} \left(\pm y \mp \frac{H_2 a_2}{2}\right)^{s_2}. \tag{51}$$

Here H_j is the discrete number of unit cells in the j^{th} direction encompassing the workable PC domain, s_j is an integer value herein set to 3, and ξ_0 is a constant value between 1,000 and 10,000 depending on the selected frequency. The damping parameters are arbitrarily tuned for each frequency to minimize reflection. Depending on the location of the individual damping domains, the first or second polynomial terms in Eq. (51) will be removed and the appropriate +/− sign will be selected to ensure the damping function increases away from the domain. This damping function is of arbitrary nature and other functions, such as an exponential, could be considered as well; the important damping function feature is a slow increase away from the real PC domain (see Fig. 10).

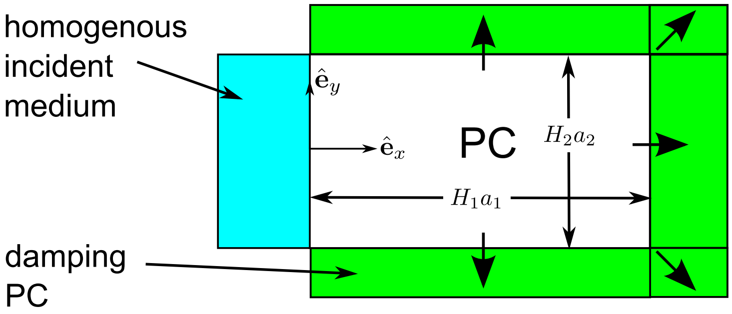

Figure 10: The geometry of a FEM model designed for normal and oblique incidence with a PC domain, a homogenous incident domain, and five damping PC domains to replicate an semi-infinite half-space. For each damping domain the arrows indicate the direction of damping, given by Eq. (51).

The FEM verification model, depicted in Fig. 10, can be used for either normal or oblique incidence. All numerical simulations are executed using COMSOL with a monochromatic plane wave, of unit amplitude, incident from the far left, specified using built-in radiation conditions. The number of unit cells to include in all numerical comparison models is tuned to minimize computational effort yet yield a sufficiently "infinite" domain; typically the number of cells ranges from 100 for normal incidence ($H_1 \gg H_2$) and up to 4,000 for oblique incidence ($H_1 \sim H_2$).

2.7.2 Verification of the half-space BWE

The three verification models will be executed at selected angular frequencies: $\omega =$ 10,000, 5,000, and 39,000 rad/s; the first two models at normal incidence (i.e. $\theta = 0$), and the last at $\theta = 30$ degrees. In all three cases the geometric and material parameters are carried over from Sec. 2.5.

2.7.2.1 Verification study 1

The dispersion and expansion details discussed previously are used to compute the reflected and transmitted pressure fields Eqs. (21) and (22) and power coefficients Eq. (37) in each of the three cases; only pressure fields will be compared against the numerical model. At the frequency $\omega = 10,000$ rad/s and $\theta = 0$ the numerical procedure described in Sec. 2.5, led to the selection of one propagating Bloch ($k = 5.037$ rad/m) wave and 8 evanescent waves. Both real and imaginary parts of the pressure field are seen in Fig. 11a and here $R_W = 0.168$ and $T_W = 0.832$. Excellent agreement can be seen between the numerical model using an array of 180 unit cells. In this study, and in the next two studies, agreement with modal deafness as discussed in Ref. [49] is observed. The modal deafness implies that Bloch modes which are antisymmetric with respect to the incident plane wave are not excited and thus $t_i = 0$ for these waves.

It was previously asserted that a necessary Bloch wave criterion for an accurate result is $\mathbf{c}_g \cdot \hat{\mathbf{e}}_x > 0$. As an example, the propagating Bloch wave with $k = 5.037$ rad/m is intentionally swapped with its counterpart ($k = -5.037$, a wave with group velocity of opposite sign); the same evanescent waves are used. Here the computed coefficients are $R_W = 5.934$ and $T_W = -4.934$ which is physically incorrect as R_W, T_W

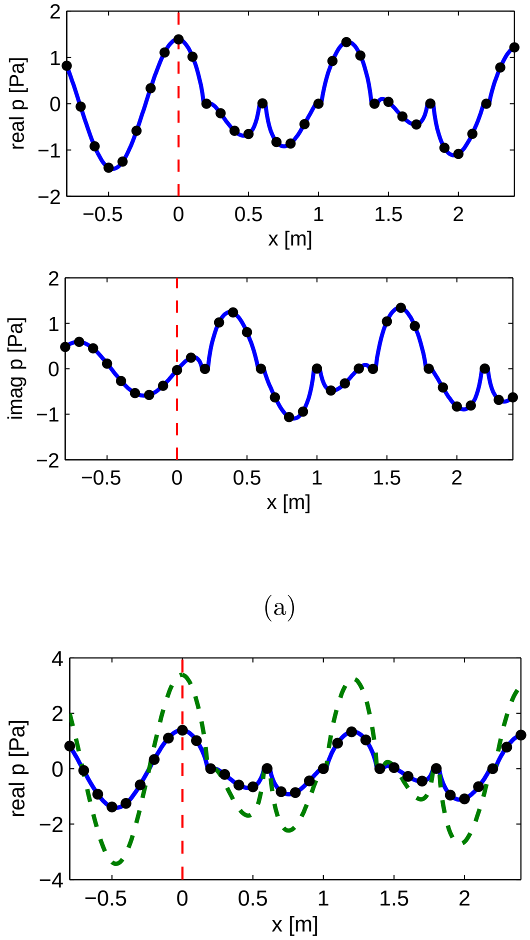

(a)

(b)

Figure 11: A comparison of the (a) real and imaginary components of the pressure field from the Bloch expansion (line) and the numerical model (dots) field, along a horizontal line centered at $y = 0.2$ m. Here $\omega = 10,000$ rad/s and $\theta = 0$ degrees (normal incidence) and the interface is demarcated by a vertical dashed line. Plot (b) compares the real pressure field from (a) with the result of an incorrect Bloch wave expansion intentionally disregarding the group velocity selection criterion (dashed curve).

must be ≤ 1. The incorrect Bloch wave selection is further examined, by comparing the real part of the pressure field versus the correct real part of the expansion and numerical model, in Fig. 11b. The observed mismatch reinforces the assertion that the expansion must contain propagating Bloch waves with group velocity pointing into the medium.

2.7.2.2 *Verification study 2*

A plane wave encounters the PC half-space at normal incidence at $\omega = 5,000$ rad/s, which is a frequency within the first band gap (see Fig. 8). There are no propagating waves at this frequency and the expansion only consists of 2 decaying waves and 8 evanescent waves (see Fig. 8). Figure 12 displays a comparison between the real and imaginary parts of the pressure field versus FEM simulations. The numerical verification model presented in Fig. 10 consists of 15 unit cells within the workable domain. Again, excellent agreement is seen between the results from the Bloch expansion and the numerical model results. Here, as expected, a power reflection coefficient equal to unity is observed.

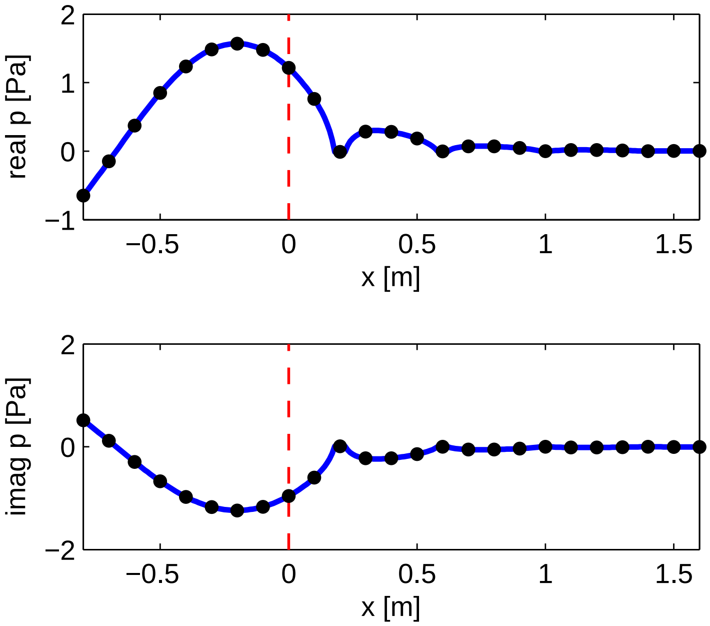

Figure 12: A comparison of the real (top) and imaginary (bottom) components of the pressure field from the Bloch expansion (line) and the numerical model (dots) field, along a horizontal line centered at $y = 0.2$ m. Here $\omega = 5,000$ rad/s and $\theta = 0$ degrees (normal incidence) and the interface is demarcated by a vertical dashed line.

2.7.2.3 Verification study 3

This study for oblique incidence raises the frequency to $\omega = 39,000$ rad/s and $\theta = 30$ degrees. Calculations proceed as before and the real and imaginary parts of the pressure field are compared between the expansion and numerical FEM results in Fig. 13a.

Again excellent agreement is seen in the results utilizing 2 decaying Bloch waves and 7 evanescent waves. At this frequency 3,760 unit cells for the "infinite" PC and over 4.5 million nodal degrees of freedom were employed in the comparison. The comparison simulation time exceeded two hours versus approximately ten minutes elapsed for the Bloch wave expansion. The numerical results indicate perfect acoustic energy reflection for this study. To further explain the acoustic reflection, the plot in Fig. 13b shows the intensity field $I_x(x, 8.2)$. Clearly, after 10 unit cells ($x = 4$ m) the decaying intensity decreases to a very small value. The decaying intensity field, along with Eq. (35), result in perfect acoustic reflection ($R_W = 1$) despite the frequency not residing in a complete band gap, a feature discussed in Sec. 2.8.1.

2.7.3 Verification of the layer BWE

Here the two-dimensional layer BWE is verified against the FEM model. The FEM model discussed in Fig. 10 is used. However, to accommodate a layer model, the right most artificial damping PC layers are replaced with the necessary homogenous media, described by ρ_t, c_t.

For the layer BWE verification study, the incident wave is set to $\omega =$ 10,000 rad/s and $\theta = 0$ degrees and $\rho_i = \rho_t, c_i = c_t$. There are $H = 20$ unit cells used in the model; the PC thickness is 8 m. Using the provided numerical parameters, the layer BWE is computed. There are 5 reflected and transmitted waves, with $N^A = N^B = 5$; subsequent analysis shows that $R_W = 0.21$ and $T_W = 0.78$. Figure 14 displays the pressure field using the layer BWE versus the FEM model. Clearly, excellent

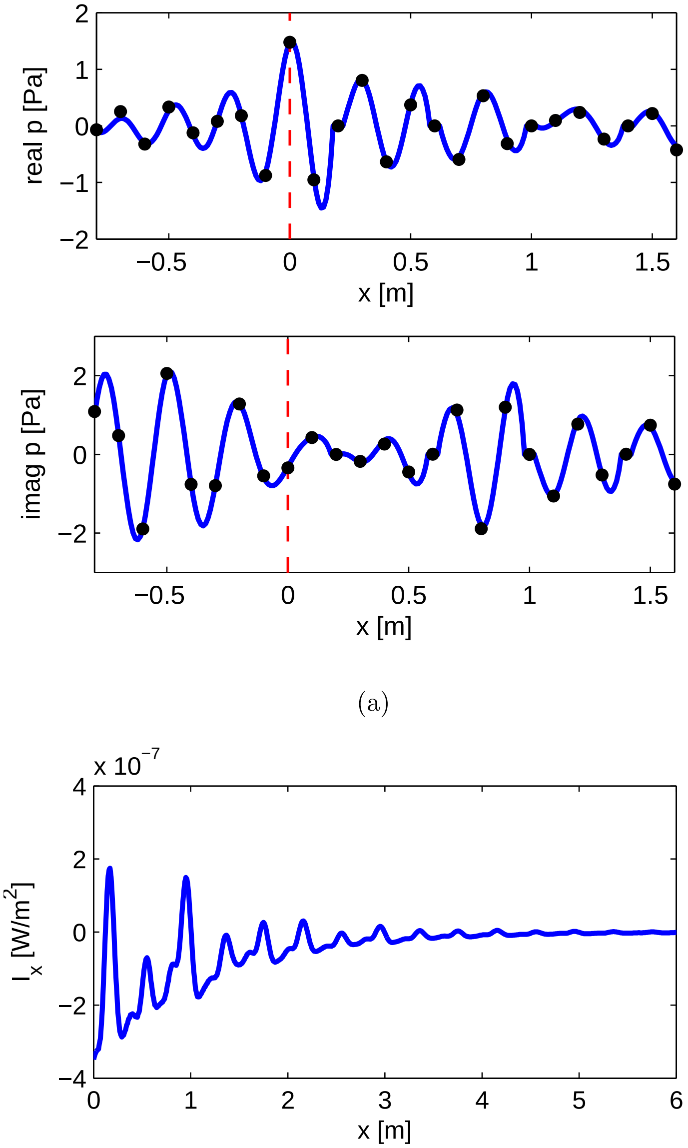

(a)

(b)

Figure 13: A comparison of the (a) real and imaginary components of the pressure field from the Bloch expansion (line) and the numerical model (dots) field, along a horizontal line centered at $y = 8.2$ m. Here $\omega = 39,000$ rad/s and $\theta = 30$ degrees and the interface is demarcated by a vertical dashed line. Plot (b) is the time averaged intensity (note the difference in x-axis limits) in the $\hat{\mathbf{e}}_x$ direction in the PC, plotted along a horizontal line through the PC.

agreement is seen in the numerical results. This plot establishes the accuracy of the layer BWE.

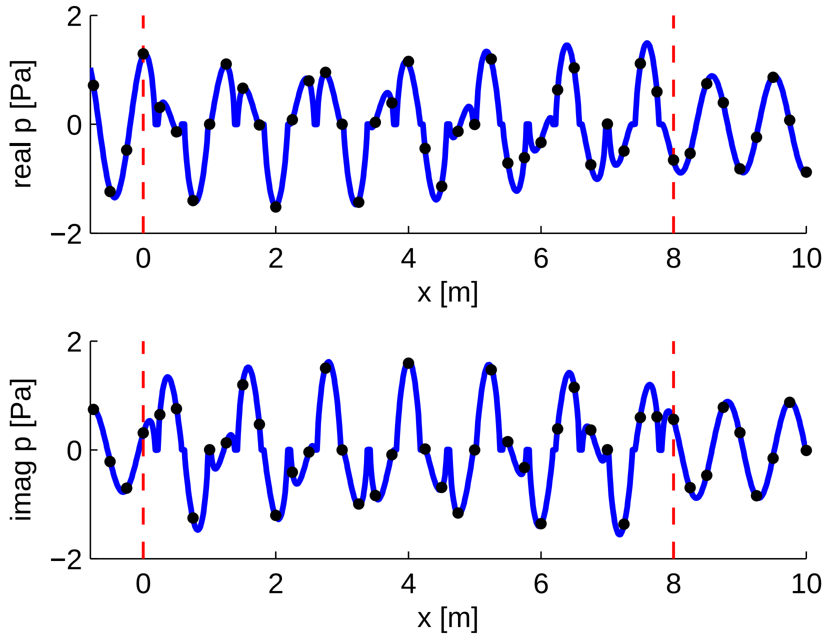

Figure 14: A comparison of the real (top) and imaginary (bottom) components of the pressure field from the layer Bloch expansion (line) and the numerical model (dots) field, along a horizontal line centered at $y = 0.2$ m. Here $\omega = 10,000$ rad/s and $\theta = 0$ degrees (normal incidence) and the interface is demarcated by a vertical dashed line.

2.8 Parametric studies

2.8.1 Angular band gap

In the last verification study of Sec. 2.7.2.3 it was shown that perfect reflection was recorded for a frequency not in a band gap. Analogous to the zero acoustic wave energy transmission into a homogenous fluid this incidence angle is referred to as a critical angle. At a critical angle θ_c and a fixed frequency, there will be no propagating Bloch waves. The Bloch expansion consists solely of decaying and evanescent Bloch waves and the pressure field in the PC will always be attenuated. Accordingly, all acoustic energy will be perfectly reflected from the PC. Romero-Garcia *et al.* [73] provided theoretical and experimental evidence of an attenuated field within the PC. They refer to this dispersion behavior as an angular band gap. This reflection effect is an intrinsic property of the PC, and can be studied by simple geometrical analysis of the dispersion behavior in k-space. To illustrate the result, an isofrequency contour at $\omega(k_x, k_y) = 39{,}000$ rad/s is displayed in Fig. 15a. This dispersion data is calculated by varying θ over the interval $\pm\arcsin(c_i\pi/\omega a_2)$.

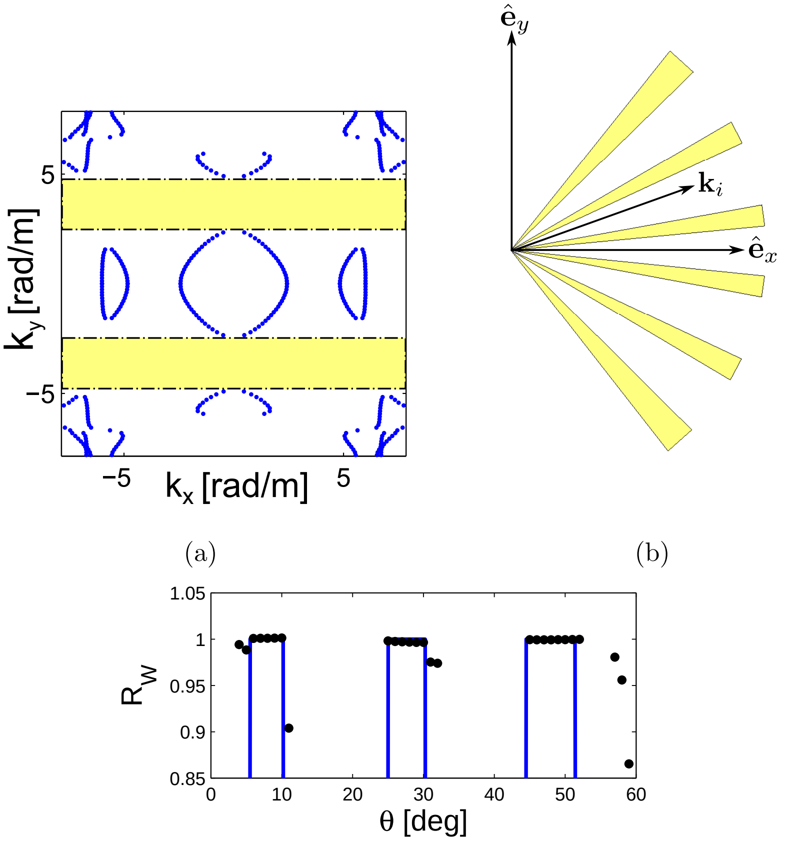

(a) (b)

(c)

Figure 15: (a) An isofrequency contour in k-space at 39,000 rad/s with real wavenumbers as dots and shaded regions, where no real wavenumbers exist, indicating wavenumbers corresponding to critical angles. (b) A graphical display of the critical angles where shaded regions indicate ranges of critical angles. (c) Validation of the critical angle observation versus direct numerical calculation (dots). Solid lines are from wedge regions from (b).

Horizontal regions in k-space, illustrated in Fig. 15a, correspond to incidence angles that yield complex wavenumbers. Let the set of critical wavenumbers, k_c, contain the wavenumbers k_y in the first Brillouin zone that correspond to critical angles (shaded regions in Fig. 15a). Periodicity of the dispersion relationship in k-space amounts to several critical wavenumber regions, all shifted by integer multiples of b_2. Critical angles can be calculated in the range $(-90°, 90°]$ degrees from

$$\theta_c = \arcsin\left[\frac{c_i}{\omega}(k_c + mb_2)\right] \tag{52}$$

for any integer m such that the arcsin argument is ≤ 1. The critical angle data is displayed graphically in Fig. 15b such that any acoustic plane wave with incident wavevector $\mathbf{k}_i$ within a shaded region will be perfectly reflected by the PC half-space.

The assertion that there exists multiple incidence angles where perfect acoustic reflection occurs, as defined by Eq. (37), can be verified by direct numerical evaluation. In Fig. 15c a sweep of angles from 0 to 60 degrees is performed and the power reflection coefficient is computed from the Bloch wave expansion. Symmetry of the PC implies angular symmetry of this data about $\theta = 0°$. At critical angles, derived solely from the geometrical analysis of Fig. 15a, the power reflection agrees favorably from the separate direct calculations. Note, the presented geometrical analysis only indicates angles of perfect reflection. The reflection at intermediate angles can only be determined by direct expansion computations and is not applicable to the analysis in this section. Subsequently, the reflection values in excess of 55° are not of present interest. The results in this figure corroborates the assertion of identification of PC critical angles via inspection of the isofrequency contour. It is noted that the identified critical angles differ from the angles defined by Bragg's diffraction law of $a_2 \cos\theta_c = m\pi c_i/\omega$ for some integer m.

2.8.2 Power reflection

Now the relation between the power reflection and parameters such as frequency and incidence angle is studied. This parametric study will employ the presented, general, expansion technique and serve to detail the acoustic reflection for a variety of incident angles and frequencies.

The harmonic frequency is varied from 500 to 20,000 rad/s and the incidence angle is swept from 0 to 75 degrees. The computed reflection, seen in Fig. 16, displays large regions, particularly at low frequencies, of perfect reflection. The regions of perfect

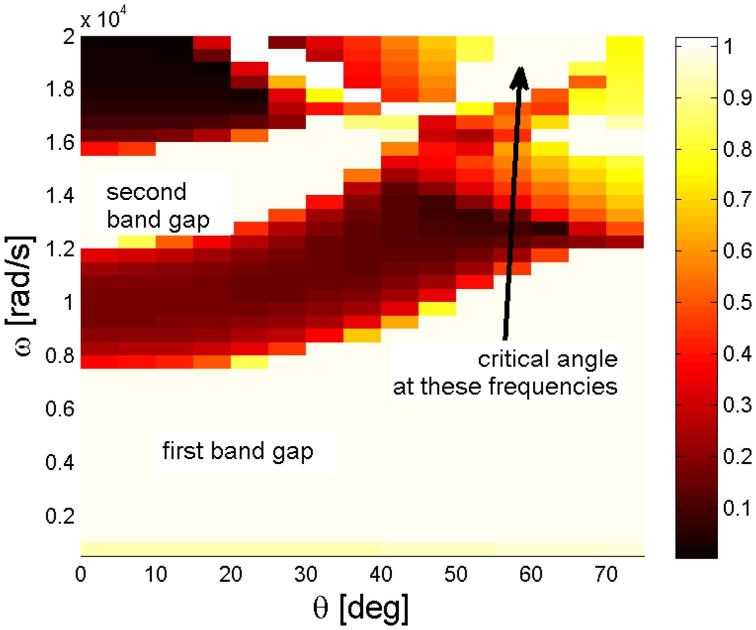

Figure 16: The power reflection coefficient computed versus frequency and incidence wave angle. Specific regions of high reflection are annotated on the plot, as band gaps or critical angle effects. Recall 0° is normal incidence.

reflection, attributed to the first or second band gap or critical angles, are annotated on the plot in Fig. 16. As the frequency increases, the number of wavenumber dispersion surfaces in k-space increases, providing diminishing band gaps and leading to the low reflection at frequencies exceeding 16,000 rad/s. At these higher frequencies the regions of high reflection are attributed to the critical angle effect, discussed earlier, and not complete band gaps as in the low frequencies below 7000 rad/s.

2.9 Conclusion

In this chapter, two-dimensional phononic crystals were considered. In particular a new dispersion technique was introduced and verified; a half-space BWE and layer BWE were introduced and verified; and angular band gaps were discussed. The research contributions of this chapter are as follows: (i) formulation of a dispersion technique, implemented using commercial finite element software; (ii) a Bloch wave selection criterion based on group velocity considerations designed for direct applicability to a Bloch wave expansion; (iii) derivation and verification of a half-space and layer BWE. The next chapter builds upon the current chapter and applies the theory to three dimensions.

CHAPTER III

BLOCH WAVE EXPANSION IN THREE DIMENSIONS

3.1 Overview

In this chapter the three-dimensional half-space and layer BWE will be introduced. The 3D BWE shares many similarities to the 2D version, largely, the use of the FEM for the dispersion relationship and the selection rules leading to a correct expansion. Verification will be performed using Feuillade's SCS code.

3.2 Three-dimensional phononic crystal

Consider a semi-infinite PC half-space ($x \geq 0$) composed of an infinite tessellation of cells; see Fig. 17a. Adjacent ($x < 0$) to the half-space is an incident homogenous medium (here water is used) with density $\rho_i = 1000$ kg/m^3 and speed $c_i = 1500$ m/s. An incident plane wave at frequency ω and wavevector $\mathbf{k}_i$, with angles θ, ϕ (see Fig. 17a), strikes the half-space at $x = 0$. Note normal incidence corresponds to $\theta = 90°, \phi = 0°$.

The three-dimensional $\omega(\mathbf{k})$ dispersion relationship for the PC studied in this chapter is presented in Fig. 18. The technique discussed in Appendix B can be extended in a straight forward manner to three dimensions. The first frequency band gap is complete (exists for all directions of $\mathbf{k}$) and is a local resonance band gap since this frequency is close to the resonance of an individual scattering inclusion. Band gaps of this type are associated with a very fast exponential decay [15] of the internal wave field since only imaginary wavenumbers exist. The second band gap is a Bragg scattering band gap. This frequency coincides with Bragg's law of scattering, namely, that $\lambda_i \approx 2a_1$ where λ_i is the acoustic wavelength in water. A slow decay of the total

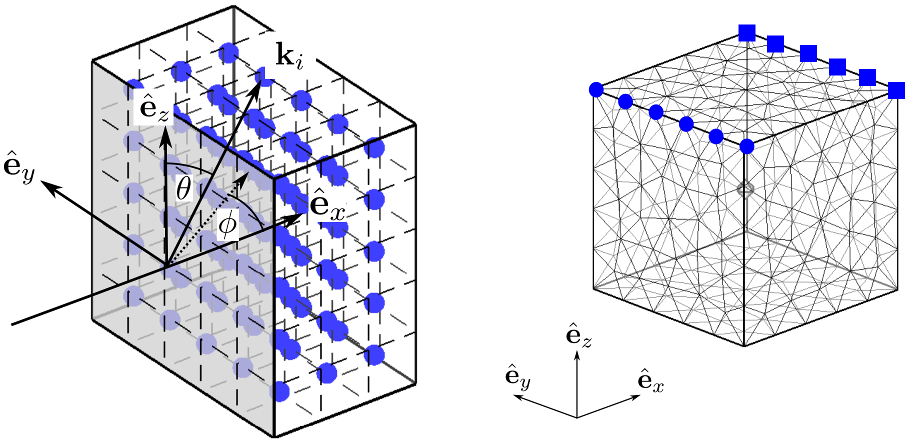

(a) (b)

Figure 17: (a) The coordinate system used in the BWE. A PC half-space resides for $x \geq 0$ and an homogenous medium for $x < 0$. An incident plane wave with wavevector $\mathbf{k}_i$ is incident on the PC (blue spheres represent the bubbles). (b) Mesh of the UC using tetrahedral elements where blue dots and squares denote a few representative degrees of freedom that are related by the periodicity requirement of the unit cell.

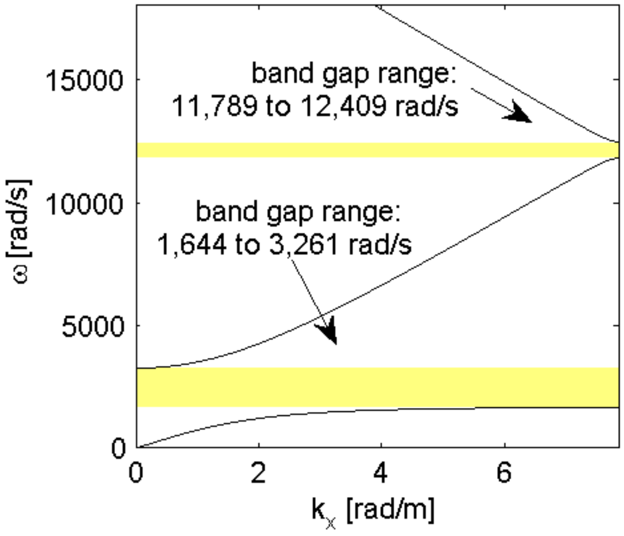

Figure 18: Dispersion diagram $(k_y, k_z = 0)$ for the PC. Band gap frequency ranges are highlighted.

pressure field is observed as the subsequent dispersion analysis predicts a complex Bloch wavenumber with $\mathrm{Re}(k) = \pi/a_1$. This specific wavenumber value indicates a phase change of π radians between adjacent bubbles, which is in accordance with one-half wavelength existing between inclusions.

3.3 Dispersion relationship

The dispersion relationship for the three-dimensional unit cell is governed by the same wave equation as discussed in Sec. 2.4.1. Employing a Galerkin discretization of Eq. (4) and using tetrahedral mesh elements results in a discretized equation of motion similar to the 2D case, namely,

$$\left(-\omega^2\mathbf{M} + \mathbf{K} + ik_x\mathbf{A}_x + ik_y\mathbf{A}_y + ik_z\mathbf{A}_z + (\mathbf{k}\cdot\mathbf{k})\mathbf{B}\right)\mathbf{p} = \mathbf{0} \tag{53}$$

where the individual matrix terms are given by (in component form)

$$M_{mn}^{element} = \int_V \frac{1}{\rho c^2}\psi_m\psi_n \mathrm{d}V \tag{54a}$$

$$K_{mn}^{element} = \int_V \frac{1}{\rho}\nabla\psi_m \cdot \nabla\psi_n \mathrm{d}V \tag{54b}$$

$$A_{mn,x}^{element} = \int_V \frac{1}{\rho}\left(\psi_n\frac{\partial\psi_m}{\partial x} - \psi_m\frac{\partial\psi_n}{\partial x}\right)\mathrm{d}V \tag{54c}$$

$$A_{mn,y}^{element} = \int_V \frac{1}{\rho}\left(\psi_n\frac{\partial\psi_m}{\partial y} - \psi_m\frac{\partial\psi_n}{\partial y}\right)\mathrm{d}V \tag{54d}$$

$$A_{mn,z}^{element} = \int_V \frac{1}{\rho}\left(\psi_n\frac{\partial\psi_m}{\partial z} - \psi_m\frac{\partial\psi_n}{\partial z}\right)\mathrm{d}V \tag{54e}$$

$$B_{mn}^{element} = \int_V \frac{1}{\rho}\psi_m\psi_n \mathrm{d}V. \tag{54f}$$

Here $m, n = 1$ to 10 for quadratic tetrahedral elements, corresponding to the individually numbered nodes of an element, and V is the volume of an element. The six matrices appearing in Eq. 53 are assembled over the domain, using the components given in Eq. (54). Further, inspection of the matrices in Eq. (14) reveals these matrices are dependent on geometry and material properties yet independent of ω, θ, ϕ; this property will be exploited for efficiency in frequency parametric studies.

As before, application of periodicity requires multiplication by the matrix $\mathbf{T}$

$$\left(-\omega^2\tilde{\mathbf{M}} + \tilde{\mathbf{K}} + ik_x\tilde{\mathbf{A}}_x + ik_y\tilde{\mathbf{A}}_y + ik_z\tilde{\mathbf{A}}_z + (\mathbf{k}\cdot\mathbf{k})\tilde{\mathbf{B}}\right)\tilde{\mathbf{p}} = \mathbf{0} \tag{55}$$

where $\tilde{\mathbf{M}} = \mathbf{T}^T\mathbf{M}\mathbf{T}$, $\tilde{\mathbf{K}} = \mathbf{T}^T\mathbf{K}\mathbf{T}$, etc. This matrix enforces periodicity on the governing finite element equations and is used throughout this Thesis. For example,

Figure 17b shows a typical tetrahedral element mesh of the unit cell. The elements of the matrix $\mathbf{T}$ enforce periodicity for the degrees of freedom indicated by the squares and dots. Again, the FEM right hand side boundary terms for the cell, omitted in Eq. (4), equate to zero after premultiplication by the matrix $\mathbf{T}^T$ [19].

Standard boundary conditions for reflection problems apply: conservation of frequency and parallel wavevector, and the matching of pressure and normal particle velocity at the interface [67]. All Bloch waves used in the BWE must have wavevectors where the y, z components (k_y, k_z) match that of the incident wave $k_{iy} = \omega/c_i \sin\theta \sin\phi, k_{iz} = \omega/c_i \cos\theta$. Imposing these wavenumber constraints on the dispersion relationship produces a set of Bloch waves required for an expansion. To impose the parallel wavenumber constraints on the Bloch waves, $\mathbf{k}$ is written as

$$\mathbf{k} = \mathbf{k}_0 + k\hat{\mathbf{e}}_x \tag{56}$$

where $\mathbf{k}_0 = [0\ k_{iy}\ k_{iz}]^T$; here the superscript T denotes the matrix transpose. This scheme allows the complex dispersion relationship to be calculated along the $\hat{\mathbf{e}}_x$ direction in k-space and automatically enforces parallel wavevector conservation.

Inserting Eq. (1) and Eq. (56) into the acoustic wave equation results in a quadratic eigenvalue problem for the dispersion relationship with eigenvalue k (equal to k_x) and eigenvector (corresponding to the mode) $\tilde{\mathbf{p}}$, namely,

$$\left[\mathbf{D}'(\omega) + k\mathbf{A}' + k^2\tilde{\mathbf{B}}\right]\tilde{\mathbf{p}} = \mathbf{0} \tag{57}$$

where

$$\begin{aligned} \tilde{\mathbf{D}}(\omega) &= -\omega^2\tilde{\mathbf{M}} + \tilde{\mathbf{K}} \\ \mathbf{D}' &= \tilde{\mathbf{D}} + i\left(k_{iy}\tilde{\mathbf{A}}_y + k_{iz}\tilde{\mathbf{A}}_z\right) + \left(k_{iy}^2 + k_{iz}^2\right)\tilde{\mathbf{B}}. \\ \mathbf{A}' &= i\tilde{\mathbf{A}}_x \end{aligned} \tag{58}$$

The solution process of the quadratic eigenvalue problem proceeds as before from

Sec. 2.4.1. Conversion to a standard eigenvalue problem is accomplished by introducing $\tilde{\mathbf{u}} = k\tilde{\mathbf{p}}$ and writing

$$(\mathbf{S} - k\mathbf{G}) \begin{bmatrix} \tilde{\mathbf{p}} \\ \tilde{\mathbf{u}} \end{bmatrix} = \mathbf{0} \tag{59}$$

$$\mathbf{S} = \begin{bmatrix} \mathbf{0} & \mathbf{I} \\ -\mathbf{D}'(\omega) & -\mathbf{A}' \end{bmatrix} \tag{60a}$$

$$\mathbf{G} = \begin{bmatrix} \mathbf{I} & \mathbf{0} \\ \mathbf{0} & \mathbf{B}' \end{bmatrix}. \tag{60b}$$

As before, calculation of the group velocity for a particular Bloch wave can be directly obtained from the eigenvalue problem:

$$\frac{\partial k_n}{\partial \omega} = \mathbf{h}_n^H \frac{\partial \mathbf{W}(\omega)}{\partial \omega} \mathbf{q}_n \tag{61}$$

where now the vector $\mathbf{h}_n^H$ is the n^{th} left eigenvector of $\mathbf{W}$ and is scaled such that $\mathbf{h}_n^H \mathbf{q}_n = 1$. Finally, the group velocity for the n^{th} Bloch wave into the PC medium $\mathbf{c}_{gn} \cdot \hat{\mathbf{e}}_x$ is obtained by

$$\mathbf{c}_{gn} \cdot \hat{\mathbf{e}}_x = \mathrm{Re}\left[\left(\frac{\partial k_n}{\partial \omega}\right)^{-1}\right] = \mathrm{Re}\left[\left(\mathbf{h}_n^H \begin{bmatrix} \mathbf{0} & \mathbf{0} \\ -\mathbf{B}'^{-1}\frac{\partial}{\partial \omega}\mathbf{D}'(\omega) & \mathbf{0} \end{bmatrix} \mathbf{q}_n\right)^{-1}\right]. \tag{62a}$$

$$\frac{\partial}{\partial \omega}\mathbf{D}'(\omega) = -2\omega\tilde{\mathbf{M}} + \frac{i}{c_i}\left(\sin\theta \sin\phi \tilde{\mathbf{A}}_y \cos\theta \tilde{\mathbf{A}}_z\right) + 2\frac{\omega}{c_i^2}\left(\sin^2\theta \sin^2\phi + \cos^2\theta\right)\tilde{\mathbf{B}} \tag{62b}$$

3.4 Half-space BWE

In this section a Bloch wave expansion in three dimensions is introduced. As discussed earlier, the expansion is quite similar to the two-dimensional Bloch wave expansion introduced by Laude *et al.* [49] and described and verified in detail in Kulpe *et al.* [42]. Thus, a deeper discussion of the method can be found in the cited works.

3.4.1 Derivation

The Bloch expansion utilizes a set of Bloch modes and wavenumbers identified from the prior dispersion analysis. These are the same rules introduced in Sec. 2.5. It is important to note the following with regard to the solutions obtained from Eq. (57). First, one can identify unique Bloch waves by selecting waves whose wavevectors' real part falls within the first Brillouin zone: $-\pi/a_1 \leq \text{Re}\, k \leq \pi/a_1$ [47]. By virtue of k-space periodicity, wavenumbers with a real part outside of this range yield repetitive Bloch waves. Secondly, eigenvalues k which would produce an exponentially growing Bloch wave are discarded. Thirdly, all propagating waves are chosen such that the wave's group velocity vector $\mathbf{c}_g$ adheres to $\mathbf{c}_g \cdot \hat{\mathbf{e}}_x > 0$. This stipulation implies that steady state acoustic power flows into the PC medium [34]. Lastly, for a necessary truncation of the expansion, complex eigenvalues with imaginary part in excess of a predetermined acceptable maximum can be discarded. After the solution of the eigenvalue problem of Eq. (57), and abiding by the above criteria, there are N Bloch wavevectors $\mathbf{k}_n = k_n\hat{\mathbf{e}}_x + k_{iy}\hat{\mathbf{e}}_y + k_{iz}\hat{\mathbf{e}}_z$ and Bloch mode functions $\tilde{p}_n$.

The transmitted wave field (defined for $x \geq 0$) $p_t(\mathbf{x})$ is expanded as a summation of the Bloch mode functions with unknown modal amplitude coefficients t_n

$$p_t(\mathbf{x}) = \sum_{n=1}^{N} t_n \tilde{p}_n\left(\mathbf{x}\right) e^{i\mathbf{k}_n \cdot \mathbf{x}}. \tag{63}$$

Similarly, the reflected pressure field (defined for $x \leq 0$) $p_r(\mathbf{x})$ is written as an expansion of L x M plane waves with unknown modal reflection coefficients r_{lm} as

$$p_r(\mathbf{x}) = \sum_{l=-L/2}^{L/2} \sum_{m=-M/2}^{M/2} r_{lm} p_{rlm}(\mathbf{x}) \tag{64}$$

where $p_{rlm}(\mathbf{x}) = \exp(i\mathbf{k}_{rlm} \cdot \mathbf{x})$ represents a reflected plane wave of order lm. In the double summation of Eq. (64), L and M correspond to the total number of plane waves in the $\hat{\mathbf{e}}_y$ and $\hat{\mathbf{e}}_z$ directions, respectively. The actual values of L, M, N are based on boundary condition convergence while minimizing computational resources. Just as in two dimensions, periodicity of the unit cell creates a two-dimensional diffraction grating on the interface [49] and therefore the three components of the reflected wavevector $\mathbf{k}_{rlm}$ satisfy

$$\begin{aligned} \mathbf{k}_{rlm} &= k_{lmx}\hat{\mathbf{e}}_x + k_{ly}\hat{\mathbf{e}}_y + k_{mz}\hat{\mathbf{e}}_z \\ k_{ly} &= k_{iy} + lb_2 \\ k_{mz} &= k_{iz} + mb_3 \\ k_{lmx} &= -\sqrt{k_i^2 - k_{ly}^2 - k_{mz}^2} \end{aligned} \tag{65}$$

where $b_j = 2\pi/a_j$, $k_i = \omega/c_i$, and l, m are integers.

To determine the modal amplitudes of the N Bloch waves and LM reflected plane waves, as is typical for half-space reflection problems [67], continuity of pressure and normal particle velocity are imposed on the interface $x = 0$:

$$p_i(0, y, z) + p_r(0, y, z) = p_t(0, y, z) \tag{66}$$

for the pressure field and,

$$v_{ix}(0, y, z) + v_{rx}(0, y, z) = v_{tx}(0, y, z) \tag{67}$$

for the normal particle velocity field. In the preceding equations, $p_i = \exp(i\mathbf{k}_i \cdot \mathbf{x})$ is the assumed form of the incident plane wave, with unit amplitude $P_0 = 1$; the incident v_{ix}, reflected v_{rx}, and transmitted velocity fields v_{tx} can be obtained from Euler's equation of linear acoustics, i.e. $\mathbf{v} = \nabla p / i\omega\rho$.

Each of the two continuity equations is next multiplied by $q_{lm} = \exp\left(-i(k_{ly}y + k_{mz}z)\right)$ and integrated over the $x = 0$ surface of the unit cell, denoted by S. Exploitation of the orthogonality of complex exponentials results in the equations for the modal coefficients

$$i_{lm} + r_{lm} = \sum_{n=1}^{N} t_n M_{lmn}^{p} \tag{68}$$

$$\frac{1}{Z_{ilm}}\left(i_{lm} - r_{lm}\right) = \sum_{n=1}^{N} t_n M_{lmn}^{v}. \tag{69}$$

Here, i_{lm} represents the amplitude of the incident plane wave orders, $i_{lm} = \delta_{l0}\delta_{m0} = \delta_{00}$ (δ_{ij} is the Kronecker delta), and Z_{ilm} is the specific acoustic impedance of the lm-th reflected wave order in the incident medium

$$Z_{ilm} = -\rho_i \omega / k_{lmx}. \tag{70}$$

The quantities M^p_{lmn} and M^v_{lmn} represent, respectively, the two-dimensional Fourier series components of the lm-th harmonic and the n-th Bloch pressure or velocity mode

$$M^p_{lmn} = \frac{1}{S} \int_S \tilde{p}_n(0, y, z) e^{-i(lb_2 y + mb_3 z)} \mathrm{dydz} \tag{71}$$

$$M^v_{lmn} = \frac{1}{S} \int_S \tilde{v}_{nx}(0, y, z) e^{-i(lb_2 y + mb_3 z)} \mathrm{dydz}. \tag{72}$$

Here $\tilde{v}_{nx}$ represents the x-component of the n-th periodic Bloch mode particle velocity ($\tilde{\mathbf{v}}_n = \left(\nabla \tilde{p}_n + i\mathbf{k}_n \tilde{p}_n\right) / i\omega\rho(\mathbf{x})$) and $S = a_2 a_3$ is the interface surface area of the unit cell. Equations (68) and (69) represent a set of linear equations which can be solved by rearrangement of r_{lm} and t_n into vectors $\mathbf{r}$ and $\mathbf{t}$ resulting in

$$\begin{aligned} \mathbf{r} &= \left[r_{-\frac{L}{2}-\frac{M}{2}} \;\; \dots \;\; r_{\frac{L}{2},-\frac{M}{2}} \;\; r_{-\frac{L}{2},-\frac{M}{2}+1} \;\; \dots \;\; r_{\frac{L}{2},\frac{M}{2}} \right]^T \\ \mathbf{t} &= \left[t_1 \;\; t_2 \;\; \dots \;\; t_N \right]^T. \end{aligned} \tag{73}$$

The linear set of equations are posed in matrix form,

$$\begin{bmatrix} \mathbf{I} & -\mathbf{M}^p \\ -\mathbf{I} & -\mathbf{Z}_i \mathbf{M}^v \end{bmatrix} \begin{bmatrix} \mathbf{r} \\ \mathbf{t} \end{bmatrix} = \begin{bmatrix} -\mathbf{i} \\ -\mathbf{i} \end{bmatrix}. \tag{74}$$

In the above equation, $\mathbf{I}$ denotes the identity matrix while the matrices $\mathbf{Z}_i, \mathbf{M}^p, \mathbf{M}^v$ contain the entries of Eqs. (70), (71), and (72) after being partitioned following the scheme of Eq. (73). Note that the top and bottom rows, respectively, enforce pressure and particle velocity continuity. The impedance matrix for the incident medium $\mathbf{Z}_i$ is diagonal and of size LM x LM while the matrices $\mathbf{M}^p$ and $\mathbf{M}^v$ are of size LM x N.

In practice, it is often difficult to obtain a high number of numerically satisfactory Bloch modes from the eigenvalue problem of Eq. (57). Usually $N < 10$ for the physical parameter set used in this Thesis and depending on the frequency, typical values of L, M will be taken to be between 15 and 21. Often the Bloch mode functions $\tilde{p}_n(0, y, z)$ exhibit rapid spatial variation on the unit cell surface. Therefore, in order to satisfy the boundary condition with high accuracy, a high number of reflected plane waves are required to match the spatial variations. Thus it is required that $LM \gg N$ and Eq. (74) must be solved in a least squares sense. Otherwise, an unsatisfactory low number of reflected plane wave orders is used to match the pressure and velocity conditions at the 2D interface of the PC. Also, since the Bloch modes are linearly independent, the individual $\mathbf{M}$ matrices are of full rank and therefore a unique solution can be obtained to Eq. (74).

Lastly, an average power reflection and transmission coefficient can be defined as

$$R_W = -\frac{\int \mathbf{I}_r(0, y, z) \cdot \hat{\mathbf{e}}_x \mathrm{d}y\mathrm{d}z}{\int \mathbf{I}_i(0, y, z) \cdot \hat{\mathbf{e}}_x \mathrm{d}y\mathrm{d}z}. \tag{75}$$

$$T_W = 1 - R_W \tag{76}$$

where $\mathbf{I}_r$ and $\mathbf{I}_i$ represent the time averaged intensity vector fields of the reflected and incident waves, respectively. The minus sign is required since the reflected waves carry energy away from the PC interface. Note that, acoustic waves incident on the half-space in a complete frequency band gap, or appropriate incidence angles in an angular band gap, result in perfect acoustic reflection, i.e. $R_W = 1$ [42, 34]. For the parameters discussed in this dissertation, the three-dimensional angular band gaps exist at frequencies beyond that which can be capture by the verification techniques and thus are not studied.

3.4.2 Least squares solution for Bloch wave amplitudes

As a numerical illustration of the accuracy of the least squares solution, consider a wave at ω = 8,000 rad/s normally incident on the PC. The expansion procedure results in $N = 8$ Bloch waves; 8 Bloch waves are chosen for the boundary condition convergence. The least squares solution uses 225 ($L = M = 15$) reflected plane waves versus 8 ($L = 4, M = 2$) hence, $LM = N$ plane waves for the square system. The real part of the BWE surface pressure is plotted in Fig. 19a for the least squares system and in Fig. 19b for the square system; the imaginary part of the pressure field follows a similar trend. Additionally the incident plus reflected pressure field, on the interface, is plotted. These results allow one to compare the accuracy of the pressure continuity boundary condition of Eq. (66). One can clearly see the BWE pressure, determined by the least squares approach, matches very well to the incident plus scattered field with a root mean square relative error of 0.001. In comparison, the two pressure fields in Fig. 19b obtained for the square system, show poor agreement

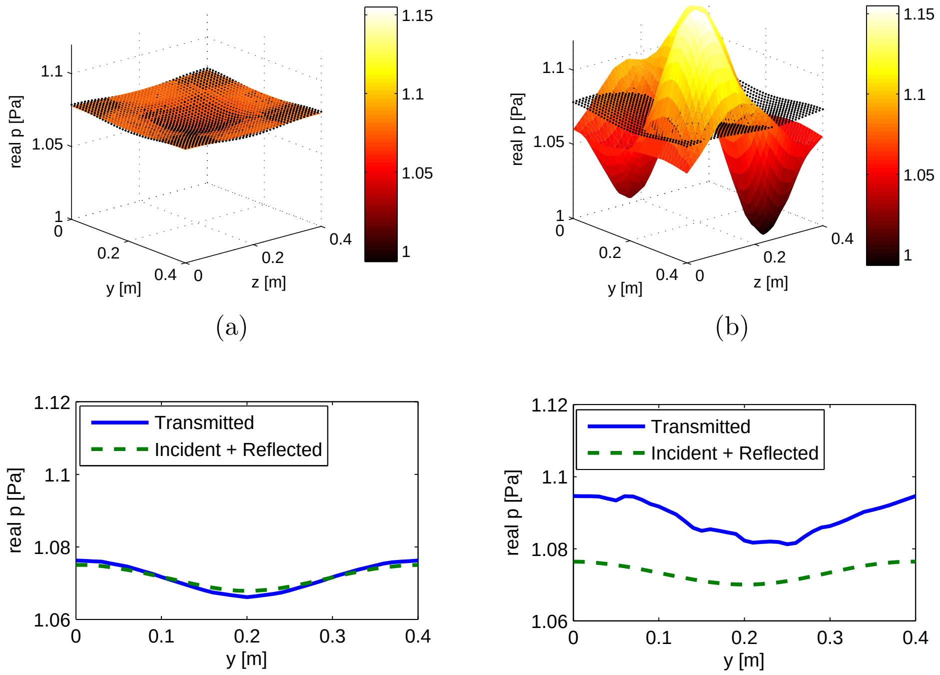

(a) (b)

(c) (d)

Figure 19: The real part of the transmitted Bloch wave expansion solution (surface) versus the incident plus reflected wave solution (dots). The two pressure fields are plotted for (a) the least squares solution and (b) the square system. The real part of the pressure field along a line $x, z = 0, a_3/2$ for the (c) least squares (d) and square system.

to the field in Fig. 19a, and to each other. A root mean square relative error of 0.047 is observed. In fact the square system leads to an incorrect expansion altogether. Furthermore, the pressure fields plotted along a line in Fig. 19c and Fig. 19d exhibit similar differences between the results of the least squares and square system.

3.5 Layer BWE

In this section the Bloch expansion for a layered phononic medium is introduced. The 3D version is very similar to the 2D version outlined in Sec. 2.6. The technique is motivated for study of finite length PCs, for any frequency. This BWE technique, which, to the best of the author's knowledge has not been presented elsewhere, shares many similarities with the half-space BWE. The phononic crystal medium considered is infinite in extent in the $\hat{\mathbf{e}}_y$, $\hat{\mathbf{e}}_z$ directions, but finite in the $\hat{\mathbf{e}}_x$ direction.

Similar to the 2D layer BWE, to find the B wave set, first, examine the unit cell in the inset of Fig. 9. Imagine the inset unit cell rotated 180 degrees - it would identically resemble the unit cell (assuming two dimensions for the sake of discussion) in Fig. 17b. Also by the wavenumber conservation principle, the y, z components of the B waves must be conserved throughout the entire PC medium. Hence, to find the quantities $\mathbf{k}^B, \tilde{p}^B$ one would evaluate Eq. (57) for the rotated version of the 'forward' unit cell, but with the input wavenumber parameters $k^B_{iy} = -k_{iy}, k^B_{iz} = -k_{iz}$. This prescription of the wavenumber in the B coordinate system is a direct result of the choice of coordinate system from Eq. (39). As before for the A wave set, the waves of the B wave set must decay exponentially ($k^B_x > 0$) and possess group velocity such that $\mathbf{c}^B_g \cdot \hat{\mathbf{e}}_{x^B} = \mathbf{c}_g \cdot \hat{\mathbf{e}}_x > 0$. If the inclusion within the cell is rotationally symmetric, implementation efficiency is achieved since $k^B_x = k^A_x, k^B_{y,z} = -k^A_{y,z}$ and $\tilde{p}^A(\mathbf{x}) = \tilde{p}^B(\mathbf{x}^B)$; thus, only the values for the A waves need be stored in memory following solution of the eigenvalue problem.

The expansion of the pressure field for the layered system proceeds as before. The reflected field is expanded in plane waves with unknown coefficients r_{lm} as in Eq. (64). The pressure field within the PC is expanded in the A and B waves, with unknown modal coefficients A_n, B_n as

$$p_{layer}(\mathbf{x}) = \sum_{n=1}^{N^A} A_n \tilde{p}_n^A(\mathbf{x})\, e^{i\mathbf{k}_n^A\cdot\mathbf{x}} + \sum_{n=1}^{N^B} B_n \tilde{p}_n^B\left(\mathbf{x}^B\right) e^{i\mathbf{k}_n^B\cdot\mathbf{x}^B}. \tag{77}$$

The field within the transmitted medium is also expanded as a set of plane waves, with coefficients t_{lm}, as

$$p_t(\mathbf{x}) = \sum_{l=-L/2}^{L/2} \sum_{m=-M/2}^{M/2} t_{lm} \exp\left(i\mathbf{k}_{tlm}\cdot\left(\mathbf{x} - Ha_1\hat{\mathbf{e}}_x\right)\right) \tag{78}$$

where the wavenumbers in the transmitted medium satisfy

$$\begin{aligned} \mathbf{k}_{tlm} &= k_{tlmx}\hat{\mathbf{e}}_x + k_{ly}\hat{\mathbf{e}}_y + k_{mz}\hat{\mathbf{e}}_z \\ k_{tlmx} &= \sqrt{k_t^2 - k_{ly}^2 - k_{mz}^2}. \end{aligned} \tag{79}$$

Due to the diffraction grating effect and wavenumber conservation in the transmitted medium, the y, z components are specified to be, respectively, k_{ly} and k_{mz}. Similar to the half-space BWE, continuity of pressure and normal particle velocity must be enforced at both interfaces.

After multiplication by q_{lm} and integrating the pressure and velocity continuity equations at $x = 0$ are written as

$$i_{lm} + r_{lm} = \sum_{n=1}^{N_A} A_n M_{lmn}^{pA0} + \sum_{n=1}^{N_B} B_n M_{lmn}^{pB0} \tag{80}$$

$$\frac{1}{Z_{ilm}}\left(i_{lm} - r_{lm}\right) = \sum_{n=1}^{N_A} A_n M_{lmn}^{vA0} + \sum_{n=1}^{N_B} B_n M_{lmn}^{vB0}. \tag{81}$$

The continuity relations at $x = Ha_1$ are written as

$$t_{lm} = \sum_{n=1}^{N_A} A_n M_{lmn}^{pAH} + \sum_{n=1}^{N_B} B_n M_{lmn}^{pBH} \tag{82}$$

$$\frac{t_{lm}}{Z_{tlm}} = \sum_{n=1}^{N_A} A_n M_{lmn}^{vAH} + \sum_{n=1}^{N_B} B_n M_{lmn}^{vBH}. \tag{83}$$

In the preceding four equations, N_A and N_B are the respective number of A and B Bloch waves used for the expansion and the impedance quantity Z_{tlm} is defined similar to Eq. (70) as

$$Z_{tlm} = \rho_t \omega / k_{tlmx}. \tag{84}$$

To incorporate the Bloch wave information within the prior continuity equations, eight new quantities are introduced that contain the two-dimensional Fourier series components of the respective Bloch modes. For example, at $x = 0$, two new quantities are

$$M_{lmn}^{pA0} = \frac{1}{S} \int_S \tilde{p}_n^A(0, y, z) e^{-i(lb_2 y + mb_3 z)} \mathrm{dydz} \tag{85}$$

and

$$M_{lmn}^{pB0} = \frac{1}{S} \int_S \tilde{p}_n^B(Ha_1, -y, -z) e^{ik_{nx}^B Ha_1} e^{-i(lb_2 y + mb_3 z)} \mathrm{dydz}. \tag{86}$$

For brevity, the other six terms M_{lmn} terms are not presented, but follow similarly to Eq. (85) and Eq. (86). The superscripts offer terms with p (v) for pressure (velocity), A(B) for the A waves (B waves), and 0 (H) for $x = 0$ (Ha_1). One will also note that because of the coordinate system choice for the B waves, a negative sign appears in front of M_{lmn}^{vB0} and M_{lmn}^{vBH}, i.e.

$$M_{lmn}^{vB0} = -\frac{1}{S} \int_S \frac{1}{i\omega\rho_1} \frac{\partial}{\partial x^B} \left(\tilde{p}_n^B(\mathbf{x}^B) e^{i\mathbf{k}_n^B \cdot \mathbf{x}^B} \right) e^{-i\left(k_{ly} y + k_{mz} z\right)} \mathrm{dydz} \tag{87}$$

Note also that M_{lmn}^{pA0} and M_{lmn}^{vA0} are identical to the quantities defined in Eqs. (71) and (72).

Finally, after computing the above quantities for different values of l, m and n, the four interface continuity conditions can be assembled into a large set of linear matrix equations

$$\begin{bmatrix} \mathbf{I} & -\mathbf{M}^{pA0} & \mathbf{0} & -\mathbf{M}^{pB0} \\ -\mathbf{I} & -\mathbf{Z}_i \mathbf{M}^{vA0} & \mathbf{0} & -\mathbf{Z}_i \mathbf{M}^{vB0} \\ \mathbf{0} & -\mathbf{M}^{pAH} & \mathbf{I} & -\mathbf{M}^{pBH} \\ \mathbf{0} & -\mathbf{Z}_t \mathbf{M}^{pvH} & \mathbf{I} & -\mathbf{Z}_t \mathbf{M}^{vBH} \end{bmatrix} \begin{bmatrix} \mathbf{r} \\ \mathbf{A} \\ \mathbf{t} \\ \mathbf{B} \end{bmatrix} = \begin{bmatrix} -\mathbf{i} \\ -\mathbf{i} \\ \mathbf{0} \\ \mathbf{0} \end{bmatrix}. \tag{88}$$

In Eq. (88), all vectors and matrices are partitioned according to the scheme in Eq. (73) and $\mathbf{0}$ is a vector or matrix of zeroes of requisite size.

This section is closed with a discussion of the layer BWE's limitations. Since the layer BWE only considers reflection from the boundary at $x = Ha_1$ and does not model the y, z limits, the technique can be inaccurate for an incident oblique plane wave on a finite PC. For band gap frequencies, however, this limitation is a non-issue due to the decay of the Bloch waves. Future work could consider modification of the layer BWE technique for oblique incidence in non-band gap frequencies.

3.6 Self-consistent scattering

In the remainder of the Thesis the self-consistent scattering technique [20, 22] (SCS) is used extensively to verify the presented Bloch wave formalism. The technique, first developed to compute scattering from arrays of bubbles, is very similar to the well known equations of multiple scattering presented by Foldy [23] and only a terse summary is given hereafter. These classical techniques are restricted to low frequency, $k_i R \ll 1$.

Consider now an array of NB arbitrarily spaced bubbles. Each individual bubble property is sub-scripted by u. The self-consistent multiple scattering technique [20] enforces that the internal pressure of the u-th bubble is equal to the incident pressure at location u plus the scattered pressure from all other bubbles. Given the position of each bubble, $\mathbf{x}_u$, one can form a set of linear equations that describe the coupling of the internal and external pressure. In matrix form, the equations read $\mathbf{Qw} = \mathbf{p}_{inc}$ where $\mathbf{w}$ is a vector containing the unknown complex differential (instantaneous minus equilibrium) volumes of the individual bubbles. The diagonal elements of the matrix $\mathbf{Q}$ describe the resonance behavior of the bubble itself while the off-diagonal terms correspond to the radiation coupling between the other bubbles [20, 22]. The components of $\mathbf{Q}$ are

$$\begin{aligned} Q_{uv} &= s_u - \omega^2 m_u - i\omega b_u, u = v \\ Q_{uv} &= -\omega^2 \rho_i \frac{e^{ik_i r_{uv}}}{4\pi r_{uv}}, u \neq v \end{aligned} \tag{89}$$

where r_{uv} is the distance between bubble u and v. The diagonal terms in $\mathbf{Q}$ are composed of the effective bubble mass $m_u = \rho_i/4\pi R_u$, the radiation damping coefficient $b_u = m_u \omega k_i R_u$, the adiabatic bubble stiffness $s_u = \omega_{Mu}^2 m_u = 3\gamma P_A/4\pi R_u^3$, the radius of the bubble R_u, the ratio of specific heats in air $\gamma = 1.4$, and the ambient pressure $P_A = 100$ kPa. The monopole resonance of a single bubble is known as the Minnaert resonance $\omega_M = \sqrt{3\gamma P_A \rho_i}/R = 1{,}024$ rad/s here [13, 58]. The vector $\mathbf{p}_{inc}$ represents the incident pressure on each bubble with $p_{inc,u} = -e^{i\psi_u}$ where the minus sign in $p_{inc,u}$ is because an increase in pressure causes a decrease in differential volume. Again, an incident wave of unit amplitude is assumed. The phase, ψ_u, on each bubble is equal to $\psi_u = \mathbf{k}_i \cdot \mathbf{x}_u$.

The steady state differential volume amplitude vector can be solved simply by $\mathbf{w} = \mathbf{Q}^{-1}\mathbf{p}_{inc}$. If the number of bubbles is not excessive ($NB < 10,000$), the matrix solution can be found as formulated. The fast multipole method (FMM) [27] is an efficient algorithm for solving the scattering problem for larger bubble PCs, even for $NB > 50,000$; see Appendix C for more details. This algorithm can quickly compute the matrix-vector product $\mathbf{Qw}$. An iterative technique is used to uniquely find $\mathbf{w}$ such that $\mathbf{Qw} = \mathbf{p}_{inc}$. The scattered field is found by summing the contribution of all NB bubbles

$$p_s(\mathbf{x}) = -\omega^2 \rho_i \sum_{u=1}^{NB} w_u G\left(\mathbf{x}, \mathbf{x}_u\right) \tag{90}$$

The scattered velocity vector is immediately found from Euler's equation of linear acoustics.

Acoustic scattering from objects can be quantified into a single metric, the differential scattering cross section $\Delta\sigma$ (which has units of area). In a scattering problem $\Delta\sigma(\omega)$ quantifies the intensity $I_s(r)$ backscattered by an object normalized by unit of incident intensity I_i [67, 58] and $1/r^2$. Unless noted, it is assumed that scattering measurements are made in a monostatic configuration, where the source and receiver are collocated, hence the use of the term *back*scattering. The well known target strength is defined as $TS = 10\log(\Delta\sigma/1\ [\mathrm{m}^2])$. The target strength can be calculated from the backscattered intensity, or using a simplification of the SCS formula, the following

$$TS = 10\log\Delta\sigma = 10\log\left(\frac{|p_s(\mathbf{x})|^2 r^2}{P_0^2}\right) = 10\log\left(\frac{\omega^4\rho_i^2|\sum_{u=1}^{NB} w_u e^{i\psi_u}|^2}{4\pi P_0^2}\right) \tag{91}$$

In the above, P_0 is the amplitude of the incident wave; it is assumed unity throughout this work. Note that since $\Delta\sigma = I_s(r)r^2/I_i$, where r is the distance from the object to the receiver, the target strength has the *same* frequency dependence as the backscattered far field intensity I_s. A object's target strength is important because, in experiments, TS, can be used to infer acoustical properties of the scattering object using appropriate acoustical models [58].

3.7 Verification

3.7.1 Verification of SCS vs. FEM

In this section the SCS technique is verified against a finite element model, specifically COMSOL Multiphysics. In this section, and after, the verification frequency ω is arbitrary. However, to illustrate different principles, a distinction is made between band gap and non-band gap frequencies. One consideration in the applicability of the SCS model is the assumption of non-decaying incident amplitude $p_{inc,u}$. Feuillade *et al.* [22] recognize, but do not address, that for large bubble PCs (fish schools in their work) the incident pressure amplitude may not be the same on all bubbles; the phase may vary as well. Geometric and material attenuation can cause the incident wave's amplitude to decay as the wave passes through the PC. Their work circumvents this problem by considering small PCs (of, say, 150 fish) [22] and sets $p_{inc,u}$ to have a constant amplitude and phase ψ_u. It is further noted that in Foldy's multiple scattering theory [23] (which is very similar to Ref. [22]), there is no specific mention regarding difficulty in determining the extent to which the incident wave reaches all scatterers. In the following sections, the incident wave is considered in band gap and non-band gap frequencies. Additionally, PCs with up to 95,000 bubbles are considered. Thus, the main purpose of this section is to show that the SCS technique accurately predicts the pressure field within a band gap, and even a decaying total wave field, despite its assumption that all scatterers see the incident pressure without any loss of amplitude or phase.

The total (incident plus scattered) field is compared at three different frequencies $\omega = \{3,000, 8,000, 12,000\}$ rad/s for field points both outside and inside a cubic PC of 1,000 individual bubbles arranged in a simple cubic structure. 1,000 bubbles is selected as high enough to illustrate the band gap effect yet be numerically feasible with reasonable effort. As a rule of thumb, about 10 unit cells are necessary for the finite PC to show a similar dispersion trend dictated by the dispersion diagram of the infinite PC; this unit cell requirement is satisfied for this cubic PC arrangement. The real part of the total pressure field is computed and compared in Fig. 20 (the imaginary part shows a similar trend) for three different frequencies. Frequency domain FEM models for larger PCs ($>$ 1,000) become computationally intensive and are not pursued.

Further comments are in order regarding the results of Fig. 20. First, in Figs. 20a and 20c, the incident wave's frequency resides in a band gap of the infinite PC and thus a spatially decaying total wave field must be observed; the FEM and SCS results corroborate this statement. The first frequency ($\omega =$ 3,000 rad/s) resides in a local resonance band gap (this frequency is close to the individual ω_M) and thus a very fast exponential decay is observed as there exists only purely imaginary Bloch wavenumbers. For the second frequency ($\omega =$ 8,000 rad/s), see Fig. 20b, a relatively high pressure value is predicted for $x > 4$ and perfect transmission ($T_W = 1$) into the

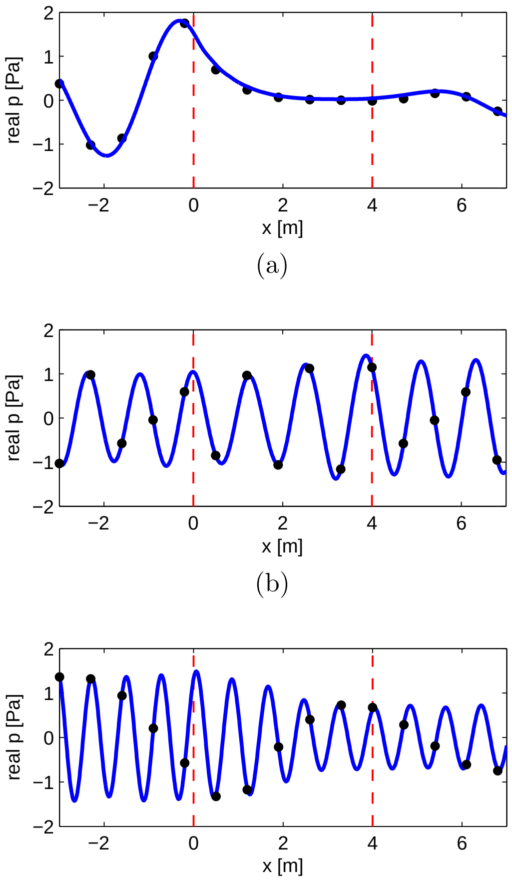

(a)

(b)

(c)

Figure 20: Real part of the total (incident plus scattered) pressure field versus x with $y, z = 0$ for the SCS technique (blue line) and FEM simulations (black dots). The calculations are performed at three frequencies: (a) 3,000 rad/s, which is in a band gap, (b) 8,000 rad/s, and (c) 12,000 rad/s, which is also in a band gap. The PC extent is from $x = 0$ to 4 m and demarcated by red vertical lines.

PC is observed. The third frequency (ω = 12,000 rad/s) resides in a Bragg scattering band gap. This frequency coincides with Bragg's law of scattering, namely, that $\lambda_i \approx 2a_1$ where λ_i is the acoustic wavelength in water. A slow decay of the total pressure field is observed as the dispersion analysis predicts a complex Bloch wavenumber with $\mathrm{Re}(k) = \pi/a_1$. The incident plus scattered field from all bubbles combine in such a way as to produce a total field that decays in space. For all three frequencies, the SCS technique also correctly predicts the pressure field at the back side of the cubic PC for $x > 4$. It is found that the SCS model is adequate for predicting the external pressure field scattered by large PCs, even though the incident pressure amplitude is assumed constant among all bubbles. The results further demonstrate modeling accuracy of the low frequency SCS technique despite the higher frequency of $\omega =$ 12,000 rad/s. At this frequency, the product $k_i R = 0.16$ which isn't necessarily very small.

3.7.2 Verification of the BWE vs. SCS

Having established the validity of the SCS technique, the half-space and layer BWE are compared directly against the SCS technique. The finite PC considered has dimensions (x, y, z) of 6.4 x 15.2 x 15.2 m ($H = 16$) and consists of 23,104 bubbles. The PC dimensions are chosen to comply with the assumptions for the layered medium: long in two directions and of finite width in the $\hat{\mathbf{e}}_x$ direction.

First the total pressure field results are shown at $y, z = 0$ as x is varied. Two frequencies considered are $\omega =$ 3,000 and 10,000 rad/s, respectively, for verification of the half-space BWE and layer BWE. For band gap frequencies, if the value of H is large enough such that the Bloch waves significantly decay before reaching the back interface at $x = Ha_1$, the half-space BWE is appropriate for modeling the internal pressure field of the finite PC. Since the layer BWE considers reflection from the back interface, it is appropriate for any frequency. However, the half-space BWE is more attractive (in band gap frequencies) than the layer BWE in terms of execution speed and numerical storage requirements. At $\omega =$ 3,000, the real components of the pressure field using the half-space BWE and SCS are compared in Fig. 21a. The total pressure field is in excellent agreement. In the band gap, the preceding dispersion equations predict an evanescent Bloch wave with $k = -1.18i$ rad/m and $R_W = 1$. Along the interface at $x = 0$, the total pressure field predicted by the half-space is shown in Fig. 21c. In both plots, agreement is seen between the BWE and SCS techniques. The imaginary part of the wave field shows similar trends.

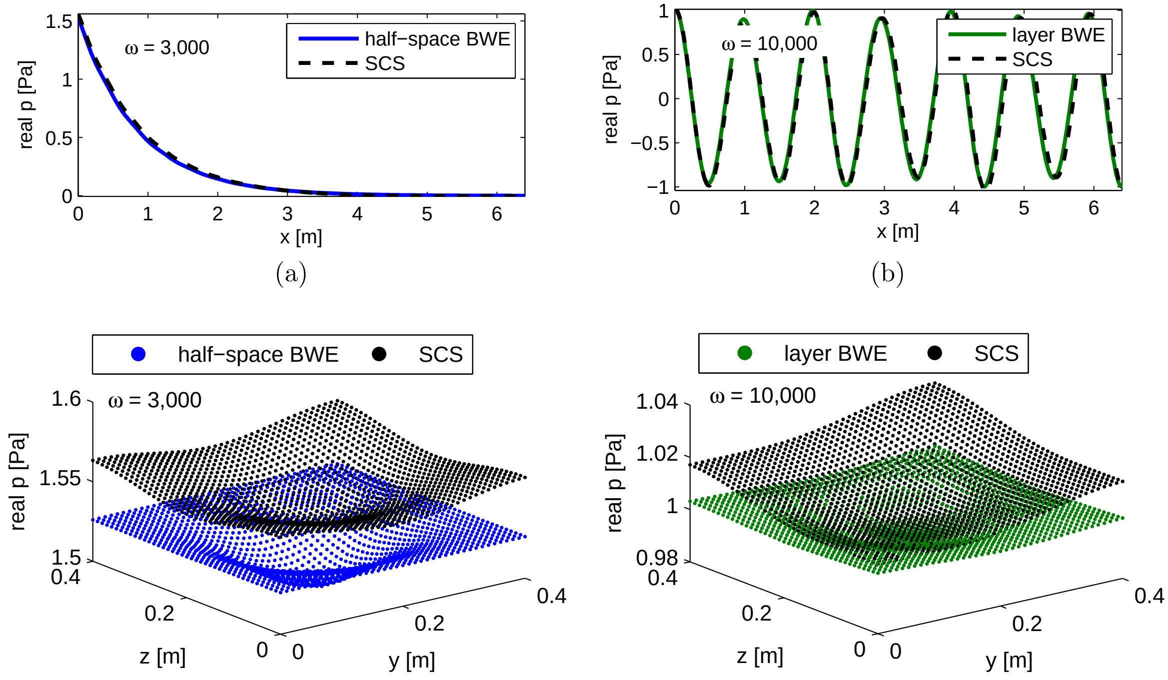

(a) (b) (c) (d)

Figure 21: (a) Real part of the total (incident plus scattered) pressure field predicted by the half-space BWE versus the SCS technique. (b) Real part of the total pressure field predicted by the layer BWE versus the SCS technique. (c) Real total field by the half-space and (d) layer BWE versus the SCS technique. In all plots: blue lines/dots represent the half-space BWE, green lines/dots for the layer BWE, and the black lines/dots for the SCS values.

At ω = 10,000, the real components of the pressure field (using the layer BWE) are compared in Fig. 21b. Again, excellent agreement is seen in the pressure field. At this frequency the primary (only one propagating in the expansion) Bloch wave propagates at $k = 6.42$ rad/m and then reflects at the edge of the PC at $x = Ha_1$. This reflection process continues to occur ad infinitum - the resulting field is that described by the layer BWE. Along the interface at $x = 0$, the total pressure field predicted by the layer BWE is shown in Fig. 21d. In both plots, agreement is seen between the BWE and SCS techniques. The imaginary part of the wave field shows similar trends. Subsequent results, not shown in Fig. 21, indicate the error on the interface pressure calculations decreases with increasing PC size. This observation supports the change from 8,000 to 23,104 bubbles. The preceding results establish the validity of approximating the internal and interface pressure fields using the half-space BWE (for a band gap) and layer BWE (for non-band gap) for a finite PC.

3.8 Conclusion

In this chapter, three-dimensional phononic crystals were considered. The dispersion technique introduced in Ch. 2 was again utilized in 3D. The half-space and layer BWE were subsequently introduced and verified. The research contributions of this chapter are as follows: (i) a half-space and layer BWE introduced for reflection and transmission of acoustic waves and (ii) Verification of both approaches versus the SCS technique. The next chapter uses the 2D and 3D BWE to determine scattering from finite PCs.

CHAPTER IV

SCATTERING FROM FINITE PHONONIC CRYSTALS

4.1 Overview

The previous two chapters discussed the 2D and 3D BWEs and their role in determination the reflection and transmission from a semi-infinite PC half-space or layer. In this chapter, the Helmholtz-Kirchhoff integral will be introduced and integrated with the BWE to discuss scattering from 2D and 3D phononic crystals. The theory will be introduced and then verified versus FEM (in 2D) and SCS (in 3D). The BWE and HKI presents an efficient and accurate approach to study the scattering from PCs. Note, as discussed in Sec. 1.3, *internal* scattering within a PC has been discussed and, ultimately, gives rise to the PC's dispersion relationship. This chapter differs from most of the literature by focusing on *external* scattering; that is, the scattered field observed at a point outside of the PC.

4.2 Helmholtz-Kirchhoff integral

Upon ensonificaiton of the PC by a harmonic plane wave, the BWE yields the pressure and velocity of the PC's surface. These quantities can be used with the HKI to predict the external scattered field.

The exterior form of the Helmholtz-Kirchhoff integral [85, 86] can be used to predict external scattering from finite objects. This analytical integral method, which is valid for two or three dimensions, requires evaluation of a surface integral of the pressure and normal velocity along an oscillating surface. Invoking a small wavelength approximation (wavelength much smaller than the PC's y, z dimensions), it is assumed that the pressure field, as determined by the BWE, accurately describes the actual pressure field for a finite PC. Under this assumption, the HKI utilizes the pressure and normal velocity as inputs to the surface integral. For example, in two dimensions, the finite PC studied is envisioned as being 'cut-out' from an semi-infinite half-space. Thus, as discussed above, the 2D BWE solution (valid for a semi-infinite half-space) can be used to describe the pressure field on the surface S. Kulpe *et al.* [40] introduced the HKI to studying the scattering from 2D PCs and excellent agreement was demonstrated against finite element simulations. Paralleling the development from Ref. [40], the application of the HKI to two or three-dimensional finite PCs is discussed next.

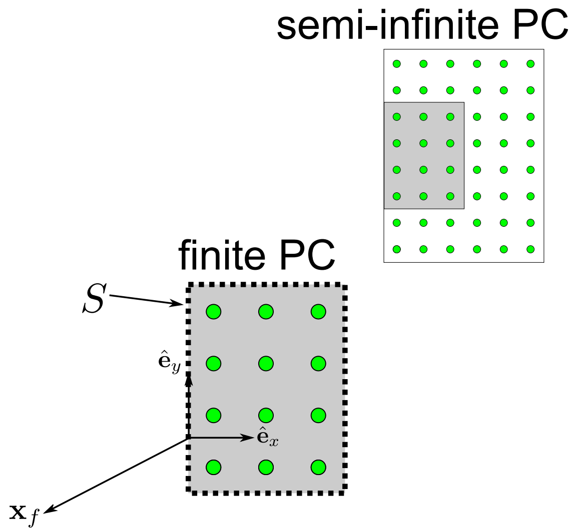

Figure 22: A semi-infinite PC with a shaded region indicating the finite PC of interest.

The Helmholtz-Kirchhoff integral computes the scattered pressure field at any field point $\mathbf{x}_f$ from knowledge of the pressure and normal velocity on a simple, closed surface S with *inward* unit normal $\hat{\mathbf{n}}$ as

$$p_s\left(\mathbf{x}_f\right) = \int_S \left[G\nabla p - p\nabla G\right]\cdot\hat{\mathbf{n}}\ \text{dS}. \tag{92}$$

where the distance from the surface point $\mathbf{x}_s$ and field point is $r = |\mathbf{x}_s - \mathbf{x}_f|$, and $k_i = |\mathbf{k}_i|$ is the wavenumber in the incident domain, and G is the applicable 2D or

3D free space Green's function

$$\left.\begin{aligned} G\left(\mathbf{x}_s|\mathbf{x}_f\right) &= \frac{i}{4}H_0^{(1)}(k_i r) \\ \nabla G\left(\mathbf{x}_s|\mathbf{x}_f\right) &= \frac{-ik_i}{4}\frac{\left(\mathbf{x}_s-\mathbf{x}_f\right)}{r}H_1^{(1)}(k_i r) \end{aligned}\right\} \quad \text{for 2D} \tag{93}$$

and

$$\left.\begin{aligned} G\left(\mathbf{x}_s,\mathbf{x}_f\right) &= \frac{1}{4\pi}\frac{\exp(ik_i r)}{r} \\ \nabla G\left(\mathbf{x}_s,\mathbf{x}_f\right) &= \frac{1}{4\pi}\frac{ik_i r-1}{r^2}\left(\mathbf{x}_s-\mathbf{x}_f\right)\frac{\exp(ik_i r)}{r} \end{aligned}\right\} \quad \text{for 3D} \tag{94}$$

In the two-dimensional Green's function, $H_0^{(1)}$ and $H_1^{(1)}$ are the Hankel functions of the first kind and, respectively, order 0 and 1. Recall, the pressure and velocity vector solution to the BWE $(p_{BWE}, \mathbf{v}_{BWE})$ of the half-space or layer technique are used for the pressure and it's gradient on S, i.e. $p(\mathbf{x}_s) = p_{BWE}(\mathbf{x}_s)$ and $\nabla p(\mathbf{x_s}) = i\omega\rho_1\mathbf{v}_{BWE}(\mathbf{x}_s)$. The total pressure field p (incident plus scattered) is found by adding the incident plane wave $p_i = \exp(i\mathbf{k}_i\cdot\mathbf{x}_f)$ to Eq. (92) [85]. In the case where $\mathbf{x}_f$ is on the surface S, a factor of $\frac{1}{2}$ must be multiplied onto the right hand side in Eq. (92) [85].

4.3 Verification in two dimensions

To verify the presented formalism of scattering from a finite PC, two computational results [40] are presented in this section. The phononic crystals used for both results, Fig. 23, contain $M_1 = 30$ x $M_2 = 30$ unit cells perfectly placed in an array; the overall PC dimensions are 18 x 18 m. As before, the inclusion is a cylinder of radius $R = 2$ cm; the lattice constant is changed to $a = 60$ cm. A finite element model, employed for comparison, is created with the same array of 900 unit cells and represents the finite PC studied herein. The verification model contains an incident harmonic plane wave and simultaneously allows scattered acoustic radiation to leave the computational domain via built-in specialized radiation boundary conditions. Increased accuracy in the radiation boundary conditions for the FEM model is obtained by having a large homogenous domain surrounding the PC, yielding some 3 million degrees of freedom.

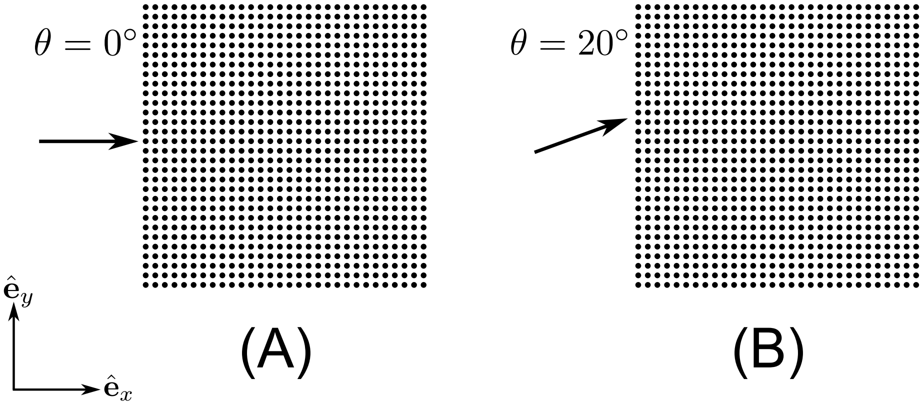

Figure 23: Two large finite PCs used for (a) result 1 and (b) result 2. The frequency of the incident wave is the same. The direction of the incident wave, indicated by the arrow, is varied for result 1 and result 2.

For comparison of the pressure field, the FEM software performs a post-processed numerical evaluation of the HKI, using Eq. (92) and the obtained FEM solution. Hence, the scattered pressure field can be compared, at any field point, between the BWE informed HKI and the finite sized PC.

4.3.1 Study 1

The Bloch wave expansion is computed for $\omega = 9000$ rad/s and $\theta = 0$ degrees (normal incidence). This frequency resides in a band gap, thus there are no propagating Bloch waves used in the expansion and all $N = 6$ of the waves decay into the PC. Alternatively, all incident acoustic energy is perfectly reflected [42] and the scattered wave is of high amplitude. At this frequency, the parallel wavelength $\lambda_i / \cos\theta = 2\pi/(k_i \cos\theta) = 1.04$ m and the length of the finite PC ($M_2 a_2$) is 17.3 times larger, which conforms with the short wavelength assumption.

Numerical results comparing the real and imaginary parts of the pressure field along the line $(x, 0)$ for $x \in$ [-10,0] are displayed in Fig. 24. The pressure results of the BWE and application of the HKI from Eq. (92) (2 minute solution time, on an

Intel quad-core i5 PC, 2.66 GHz, 16 GB RAM) compares excellently with the pressure results of the FEM model (30 minute solution time). Note the results in Fig. 24 are in the acoustic near field. The far field is not reached until about x_f = -12.7 m with a peak amplitude of 1.29 Pa following a sharp decline in pressure amplitude due to cylindrical spreading. For completeness, the comparison of the acoustic pressure field is compared over a rectangular region and shown in Fig. 25. Good agreement is noted between the spatial characteristics and amplitude of the BWE and FEM solutions. The maximum relative error between the comparison plots is about 20%.

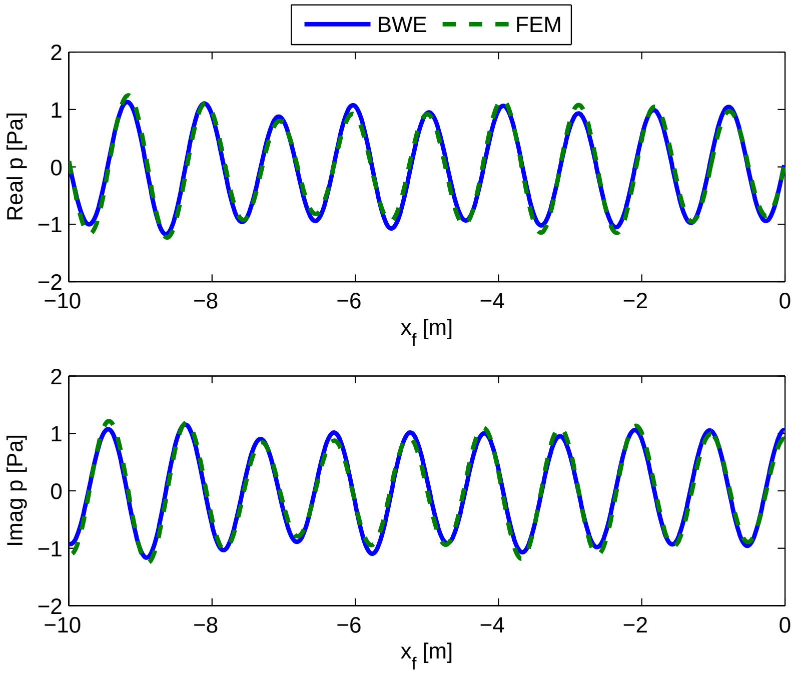

Figure 24: Result 1: Comparison of the real (top) and imaginary (bottom) parts of the scattered acoustic near field pressure for the BWE+HKI versus the FEM model.

4.3.2 Study 2

The Bloch wave expansion is computed for $\omega = 9000$ rad/s and $\theta = 20$ degrees. At this frequency, the parallel wavelength $\lambda_i / \cos\theta = 2\pi/(k_i \cos\theta) = 1.11$ m and the length of the finite PC ($M_2 a_2$) is 16.1 times larger which, again, conforms with the short wavelength assumption. Similar to the prior case, numerical results comparing the

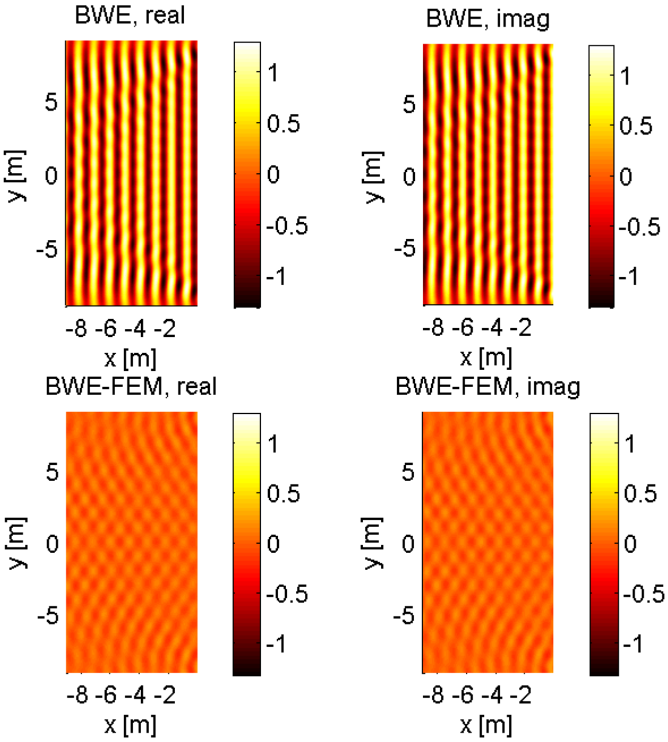

Figure 25: Result 1: (Top) The real and imaginary parts of the scattered acoustic pressure field (in Pascals) for the BWE using the HKI. (Bottom) The difference between the Bloch and FEM results

.

real and imaginary parts of the pressure field along the line $(x, 0)$ for $x \in$ [-10,0] are displayed in Fig. 26 for the near field. Excellent agreement is seen, between the BWE and FEM models, of Fig. 26. As done previously, the comparison of the acoustic pressure field is compared over a rectangular region and shown in Fig. 27. Again, good agreement between is noted between the spatial characteristics and amplitude of the BWE and FEM solutions. The maximum relative error between the comparison plots is about 25%. In this particular study, the frequency is low enough such that there exists only one reflected propagating plane wave order (see Eq. (65)), therefore the reflection is specular. The reader can see that in Fig. 27 that the wave field, implemented using the HKI, conforms with the specular reflection as predicted by the BWE.

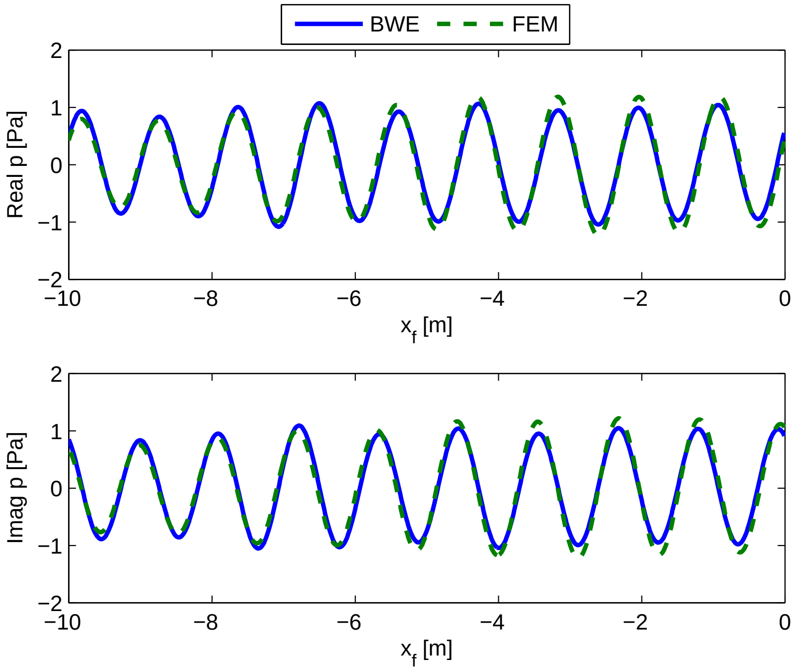

Figure 26: Result 2: Comparison of the real (top) and imaginary (bottom) parts of the scattered acoustic near field pressure for the BWE+HKI versus the FEM model.

4.4 Verification in three dimensions

In this section, the external scattered pressure field is computed for a set of cubic PCs and different frequencies by integrating the BWE and HKI techniques.

4.4.1 Scattered pressure

Again, consider a PC of 8,000 bubbles with size 8 x 8 x 8 m. In the rest of this chapter, a = 40 cm. This PC size is chosen as a compromise between adequate error in scattering results and computation time. A plane wave at ω = 12,000 rad/s is normally incident (θ, ϕ = 90°,0°) on the PC. The frequency is specifically chosen to coincide within the Bragg band gap. The presented theory, even with the layer BWE, is expected to offer best performance, versus the SCS technique, in band gap frequencies since the Bloch waves decay and any wave interaction with the edge ($x = Ha_1$) of the PC is minimal.

The real and imaginary parts of the scattered field are compared in, respectively,

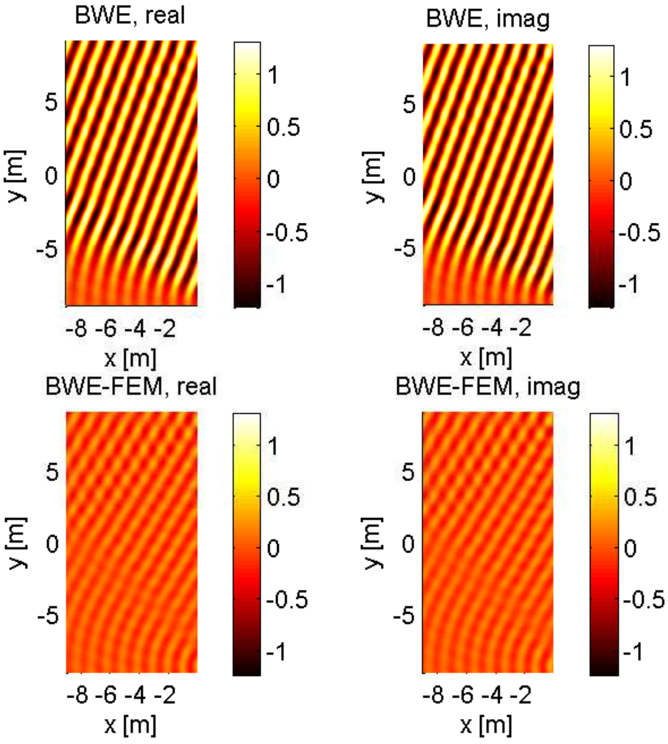

Figure 27: Result 2: (Top) The real and imaginary parts of the scattered acoustic pressure field (in Pascals) for the BWE+HKI. (Bottom) The difference between the Bloch and FEM results

.

Figure 28a and Figure 28b. Firstly, one can observe good agreement in the comparison between the HKI technique (using the half-space BWE pressure) versus the SCS technique. In the far field, the relative error between the BWE+HKI and SCS amplitudes converges to approximately 10%. These numerical results indicate good agreement between the scattered pressure field arrived at from the BWE versus the SCS technique.

Further comparison in the plane $z = 0$ for amplitude are respectively shown in Fig. 29a and Fig. 29b. Most notably, the spatial variation of the pressure amplitude qualitatively agrees very well between the two techniques. In fact, the BWE+HKI technique fully captures the near field amplitude, the forward scatter ($x > Ha_1$) behavior, and the $y \neq 0$ axis behavior. Quantitatively, the BWE+HKI compared against the SCS technique demonstrates good agreement in the far field, with a relative error in amplitude less than 20%. Furthermore, the results on Fig. 29a indicate one can expect good agreement in the scattered pressure over a wide range of field points, anywhere around the PC.

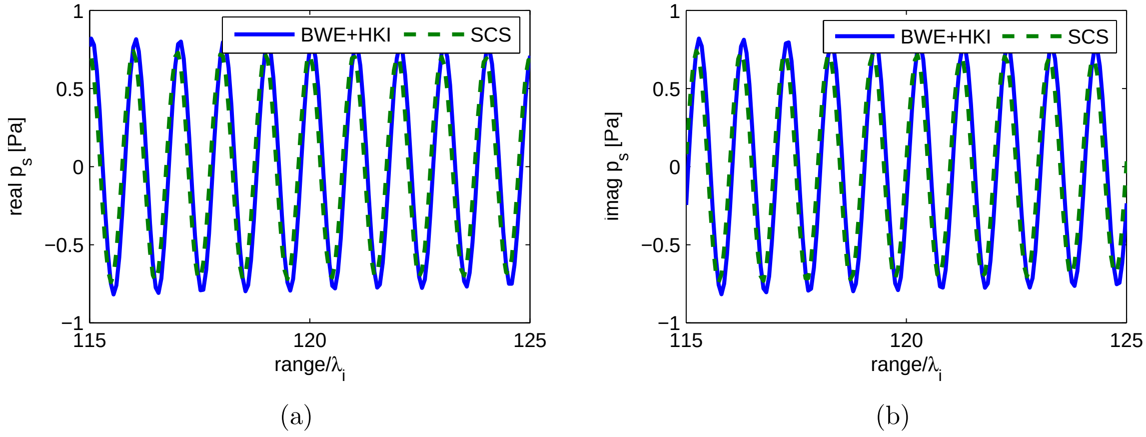

Figure 28: A comparison of the real part (a) and imaginary part (b) of the scattered pressure field by the BWE+HKI (blue line) and the SCS technique (dashed green line). The range is normalized by the incident wavelength λ_i and $y, z = 0$.

Based on the good agreement between the BWE+HKI and SCS, especially in the acoustic far field, the acoustic far field radiation pattern for the PC for plane wave incidence is computed next. For the HKI and SCS techniques, the target strength TS is computed from

$$TS(\mathbf{x}) = 10 \log \left(\frac{|p_s(\mathbf{x})|^2 r^2}{P_0^2} \right). \tag{95}$$

or alternatively for Eq. (91) for the SCS technique. The frequency is set to $\omega =$ 3,000 rad/s. The target strength is plotted over a sphere with arbitrarily large radius $r = 10^6$ m for the BWE+HKI technique in Fig. 30a and the SCS technique in Fig 30b. Since the beam pattern is defined in the acoustic far field, any arbitrary range value can be used as long as the acoustic far field is achieved. First, one will note excellent qualitative agreement between the beam patterns computed from the BWE+HKI and SCS. One can distinguish a very strong backscattered component ($TS > 30$ dB).

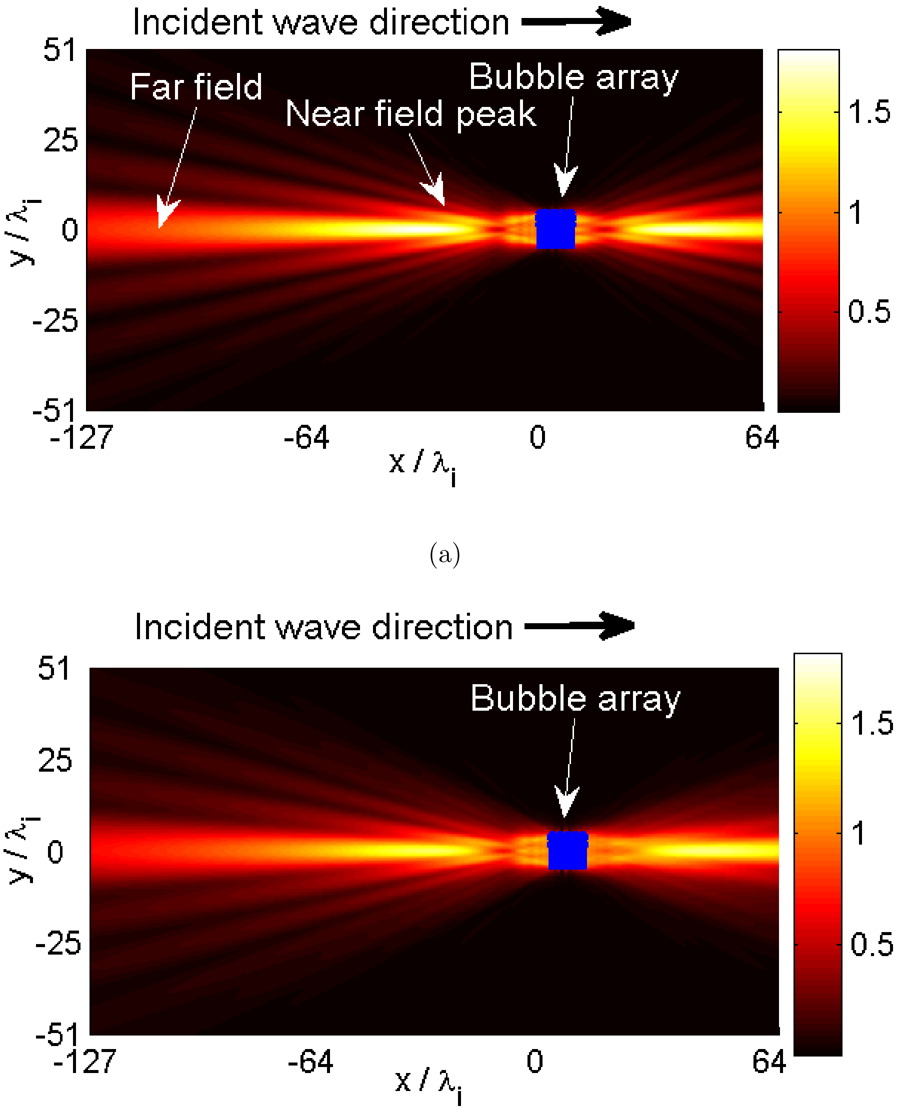

(a)

(b)

Figure 29: Amplitude of the scattered pressure field for (c) BWE+HKI and (d) SCS. The bubble array is colored in blue for clarity. The incident plane wave at ω = 12,000 rad/s strikes the PC in the direction shown and the range is normalized by the incident wavelength λ_i.

Several nulls (local minima in the beam pattern) can be identified, more pronounced in Fig. 30a, by the black lines. The results presented in this section demonstrate the very good agreement in overall scattering computations between the Bloch wave expansion and HKI when compared against the SCS technique.

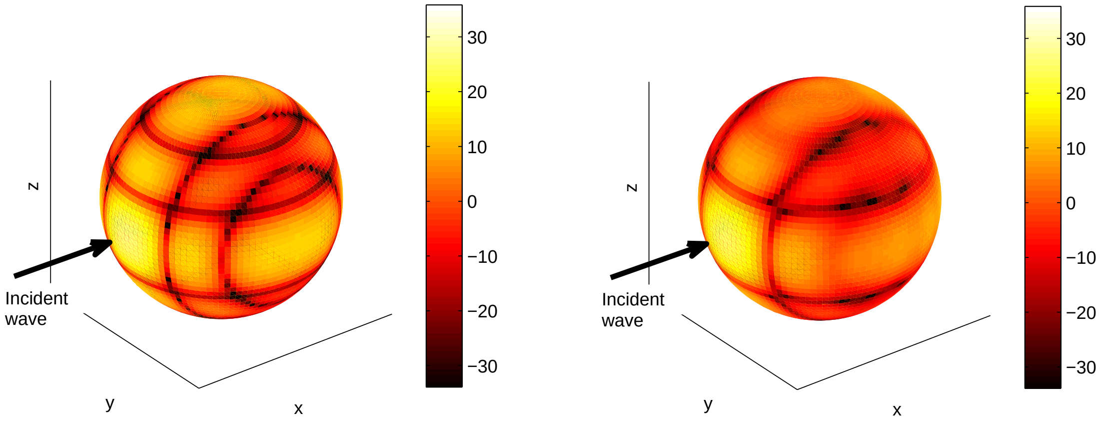

(a) (b)

Figure 30: Beam pattern for the finite PC using (a) BWE+HKI and (b) SCS techniques. The incident wave travels along the $\hat{\mathbf{e}}_x$ direction as indicated.

4.4.2 PC length convergence study

The variation of accuracy in the scattered solution versus the PC size is explored next. Here, at two distinct band gap frequencies $\omega = \{3,000, 12,000\}$ rad/s, the scattered pressure is measured, using the layer BWE and compared directly from the SCS technique. It is anticipated that greater accuracy in the scattered pressure will occur for field points within the main backscattered acoustic beam, thus, $NP = 250$ field points are chosen (in the far field) in the xy plane. These points (denoted by line 1) are along the -$\hat{\mathbf{e}}_x$ direction. For comparison, NP points are chosen in (denoted by line 2) within the xy plane at $\theta = 90°, \phi = 150°$. Namely, the first set of points resides within the main backscattered acoustic beam. The second set of points are not typically in the main beam since the size of the main beam varies with frequency and PC size. The PC length, with fixed aspect ratio and lattice constant a, is varied at each simulation step within the range of 0.8 m to 18.8 m; the number of bubbles vary from 8 to 97,336. To quantify results, at each of the NP sample points, the amplitude and phase of the pressure field is computed. Two relative error metrics, for either set of field points, for amplitude and phase are introduced as

$$E_{amp} = \left(\frac{\sum_{u=1}^{NP} \left(|p_{u,BWE}| - |p_{u,SCS}| \right)^2}{NP \cdot \max |p_{SCS}|^2} \right)^{1/2} \tag{96a}$$

$$E_{phase} = \left(\frac{\sum_{u=1}^{NP} \left(\arg(p_{u,BWE}) - \arg(p_{u,SCS}) \right)^2}{NP \cdot \pi^2} \right)^{1/2} . \tag{96b}$$

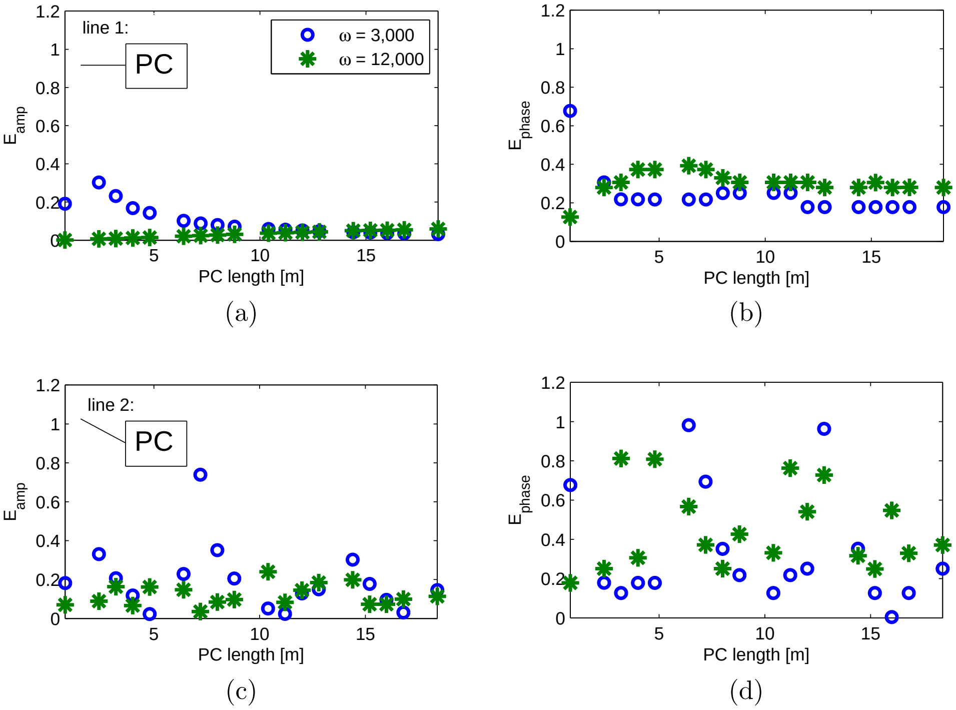

(a) (b)

(c) (d)

Figure 31: Relative error in (a) amplitude and (b) phase as defined by Eq. (96) for the points on line 1: within the main scattered beam. Relative error in (c) amplitude and (d) phase for the points on line 2: outside the main backscattered beam. In each of the four plots, the incident wave frequency is at $\omega = 3000$ rad/s (blue dots) and 12,000 rad/s (green stars). The diagram on the top left hand side of (a) and (c) indicates the direction of, respectively, line 1 and line 2 (but not the direction of the incident wave).

The relative error in amplitude and phase, as defined above, are respectively displayed in Fig. 31a and Fig. 31b for line 1 and Fig. 31c and Fig. 31d for line 2. First, in Fig. 31a and Fig. 31c, one can clearly see excellent agreement in the BWE and SCS approaches in amplitude for the band gap frequencies of 3,000 rad/s and 12,000 rad/s. Similarly, Fig. 31b indicates low phase error for the two band gap frequencies. Although prediction of the field within band gap frequencies is of primary interest, studies outside of the band gaps still indicate, generally, reasonable accuracy. Secondly, the scattered field outside of the main beam, line 2, shows some higher error in amplitude and phase. Furthermore, a comparison of line 1 versus line 2 amplitude and phase results indicate a trend: for both frequencies, low error in amplitude and phase is observed when the field point is within the main backscattered beam (field points close to the PC normal, $\approx$ 15-30 degrees); larger discrepancy is observed for points far outside of this region. The higher error exhibited out of the PC's main beam can be explained by the BWE predicting lower TS values than the SCS technique in the beam pattern nulls, which are sensitive to interference effects. The error outlier of Fig 31c with length 7.2 m is explained by this interference effect.

More remarkably, the amplitude and phase error for small PCs (PC length / $\lambda_i \approx 1$) is very low. For a PC of this size, say less than 216 bubbles, the BWE pressure field, a priori, is not accurate as the PC is not large enough to be considered 'infinite'. Despite the error in the BWE field for the small PCs, the scattered field using the HKI agrees very well. Hence, this result indicates that, even though the PC may be 'small' (compared to the wavelength), the scattered field amplitude computed, using the above approach, can be quite accurate over a wide range of field points within the backscatter direction of the PC. Lastly, with regard to oblique incidence, as expected from the discussion at the end of Sec. 3.5, there is good agreement in the scattered field when the selected frequency is in a band gap, and higher error when it is not.

4.5 Scattering of a broadband pulse

Consider a source located at $\mathbf{x}$ = (-1000, 0, 0) m that emits a sinusoidally modulated Gaussian pulse $p_{inc}(t)$ described by

$$p_{inc}(t) = Ae^{-\frac{1}{2}\eta^2 t^2} \sin \omega_0 t \tag{97}$$

with amplitude $A = 1$ Pa, modulation parameter $\eta = 500$ 1/s and carrier frequency ω_0. The fractional bandwidth of the input signal is 0.54. An example input signal ($\omega_0 = 3{,}000$ rad/s) and it's spectrum are, respectively, shown in Fig. 32a and Fig. 32b Examination of the spectrum indicates that a large portion of the input signal exists

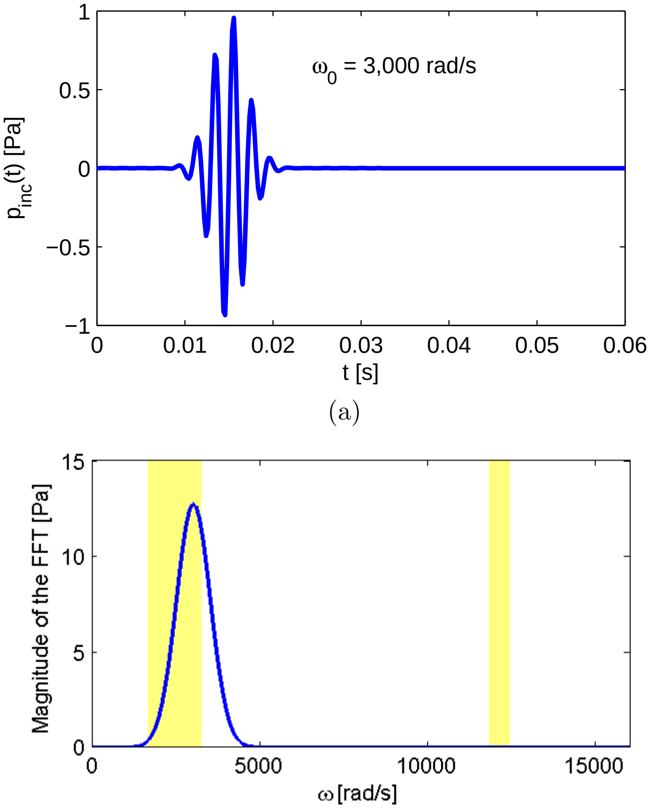

(a)

(b)

Figure 32: (a) The input pulse from Eq. (97) with $\omega_0 = 3{,}000$ rad/s. (b) The magnitude of the fast Fourier transform of (a). The band gap ranges are highlighted.

within the first band gap.

The incident wave travels and interacts with the cubic PC of 8,000 bubbles. The amplitude of the complex frequency response (from the layer and SCS techniques) is displayed in Fig. 33. Notably, over the frequency range of the study, the scattered amplitude agrees well between the BWE and SCS techniques. As concluded in Sec. 4.4.2, even though the wavelength is small compared to the PC size, positive agreement between the scattered pressure field is still observed. Also, due to Bragg scattering, the frequency response amplitude is very high within the second band bap. For several frequencies between the two band gaps, $T_W \approx 1$ which corresponding to minima of the scattered pressure amplitude. Here the wavenumber of the propagating Bloch wave satisfies $k(\omega)Ha_1/\pi = n$ for integer n. This quantity appears in classical acoustics regarding perfect transmission for a homogenous layered medium [36] and is an example of the phase-closure principle discussed within structural vibrations [57]. Similarly, the local scattered pressure amplitude maxima occur at frequencies with the wavenumber satisfying $k(\omega)Ha_1/\pi = 2(n-1)/2$.

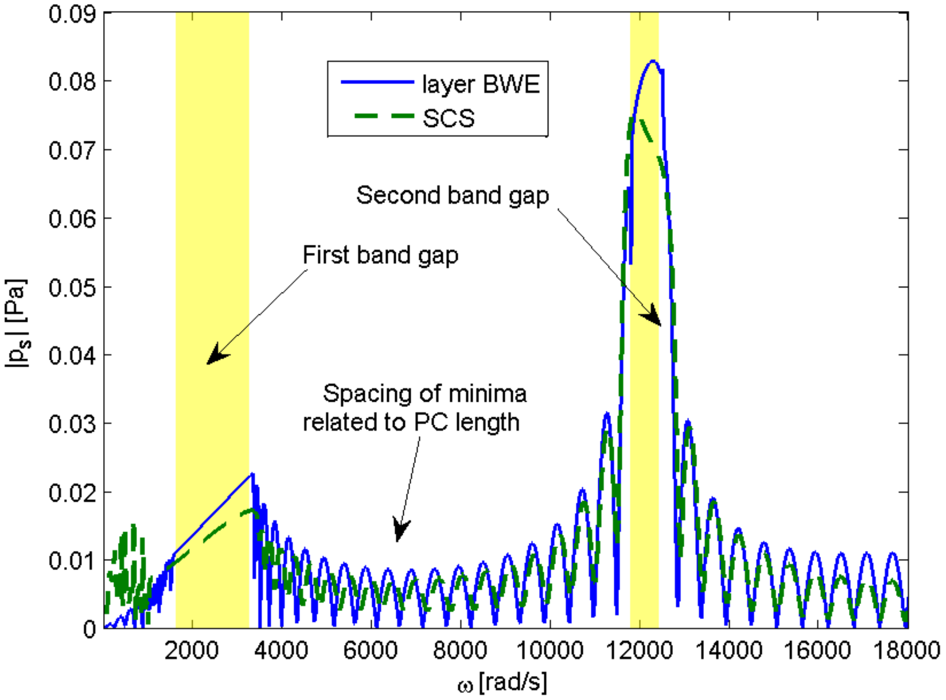

Figure 33: Amplitude of the complex scattered pressure field experienced at the receiver location for the layer BWE (blue line) and SCS (dashed green line). The two frequency band gaps are indicated by yellow boxes.

Consider a receiver co-located at the source. The discrete fast Fourier transform of Eq. (97) ($\Delta\omega = 25$ rad/s) and the PC's frequency response (at the receiver location) are multiplied together; the transient response is obtained through an inverse fast Fourier transform of this product. Of note, there is zero padding or filtering done in the signal processing of the transient results and the length of the time window ([0 0.06] seconds) is driven by the chosen frequency discretization. Also, because an $\exp -i\omega t$ time convention is used, to have increasing t yield a propagating wave, the frequency response is conjugated before the inverse Fourier transform is applied. This conjugation converges the time convention from $\exp -i\omega t$ to $\exp i\omega t$; this step is only done for the sake of presentation for the transient results. The transient results are calculated for pulses of three different carrier frequencies $\omega_0 = \{3{,}000,\ 6{,}000,\ 12{,}000\}$ rad/s and Figure 34 shows the scattered pressure signal at the receiver. Notably, there is a clear overall agreement between the BWE and SCS pressure signals for each of the three chosen carrier frequencies. At $\omega_0 = 6{,}000$ rad/s there are two arrivals: the primary scattered pulse and a secondary scattered pulse. The secondary pulse is a result of the Bloch waves reflecting from the homogenous boundary at $x = Ha_1$, see Fig. 9, and then scattering sound back to the receiver. Phase errors in the layer BWE contribute to the misalignment of the secondary pulse versus the SCS technique. Dispersion effects within the PC result in an altered shape between the primary and secondary scattered pulses (see Fig. 34). The travel distance of the propagating Bloch wave in the PC is twice the PC length = 16 m. Division of this distance by the calculated group velocity for the primary Bloch wave at ω_0 (see Eq. (61)) yields a delay time of 12.5 ms. This time, calculated using the dispersion relationship inherent to the PC, agrees fairly well with the measured primary-secondary pulse separation time of 12.9 ms. At $\omega_0 = 12{,}000$ there is general overall agreement, but some discrepancy of the BWE and SCS pressure signals is observed; note also the high pressure amplitude here as well.

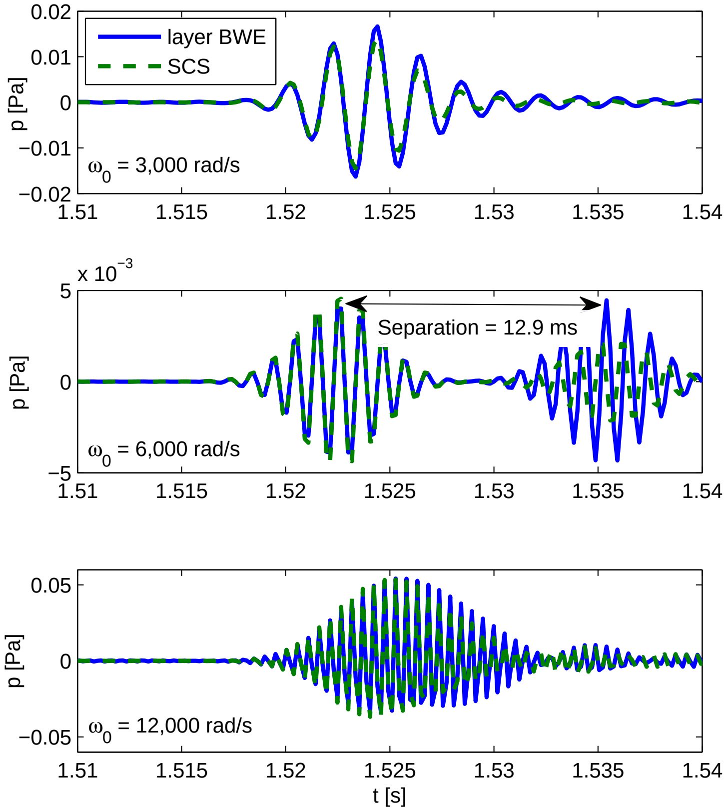

Figure 34: Time history of the pulse scattered by the finite PC using the layer BWE (blue line) and SCS (dashed green line) techniques. The results are calculated for three carrier frequencies: ω_0 = (a) 3,000, (b) 6,000, and (c) 12,000 rad/s. Note the horizontal time axes includes the travel time between the source and receiver; note also the difference in range of the vertical axes.

4.6 Facet scattering formalism

The scattering from rectangular phononic crystals has been discussed in the prior sections and at length in the prior work of Ref. [43]. Now a more ambitious scattering computation is performed - the scattering from more generally shaped phononic crystals.

4.6.1 Derivation

To approximate the scattering from an object with a complicated geometry, the object's surface can be partitioned into a set of planar facets - each facet contributes to the scattered field. The Kirchhoff approximation [58] assumes the plane wave reflection and transmission coefficients (for a traditional homogenous fluid half-space problem) can be used to calculate the pressure field on the facets. This technique does not, however, encompass the diffraction effects of the incident wave around each facet, but rather only the backscattering from each facet. Since, under the Kirchhoff approximation, the surface pressure and velocity are known, the backscattering from each facet can be computed (using the HKI) in a straight forward manner and the scattered field is a summation over the facets [58].

In this work, the scattering from a phononic crystal with geometric complexity, in analogy with the prior discussion, is formulated as a summation of the scattering from many facets. For a large phononic crystal, each facet will locally appear to contain a tessellation of unit cells. In accordance with the PC scattering discussed in Sec. 4.2, it is assumed that for large facets (facet dimension $> \lambda_i$) the Bloch wave expansion technique can be employed to calculate the pressure and velocity terms necessary for the HKI. Finally the total scattered field is found via summation over the facets. Two requisite assumptions must be satisfied for this facet scattering approach to be valid: (1) each facet is larger than the wavelength and (2) there are more than 10 unit cells along the direction of the facet's normal. The first criteria can be achieved by adjusting the frequency; the second criteria is typically trivially satisfied for large phononic crystals. Satisfaction of these assumptions ensure that the Bloch wave expansion can be used as, locally, the facet resembles a semi-infinite phononic crystal half-space.

As an example, a spherical PC geometry is shown in Fig. 35a. The corresponding periodic array of $NB = 104{,}312$ bubbles is displayed in Fig. 35b. Using a commercial package, a triangular surface mesh of the PC in Fig. 35a is generated and shown in Fig. 35c. Following meshing, the geometrical properties of each facet (denoted by superscript j) can be determined: the rotation matrix $\mathbf{R}^j$, centroid coordinate $\mathbf{q}^j$, and *inward* normal $\hat{\mathbf{n}}^j$. This rotation matrix transforms the local basis vectors, e.g. $\hat{\mathbf{e}}_x^j = \mathbf{R}^j \hat{\mathbf{e}}_x$. Points on the j-th facet, denoted by $\mathbf{y}^j$, are related by $\mathbf{x} = \mathbf{q}^j + \mathbf{R}^T \mathbf{y}^j$. By convention, and in accordance with the half-space geometry in Fig. 17a, let $\hat{\mathbf{e}}_x^j = \hat{\mathbf{n}}^j$; see Fig. 35d. Following Ref. [58], only facets ensonified by the incident plane wave, i.e. $\hat{\mathbf{n}}^j \cdot \mathbf{k}_i > 0$, are used in the summation. This set of ’ensonified facets’ is denoted Γ and contains NF facets.

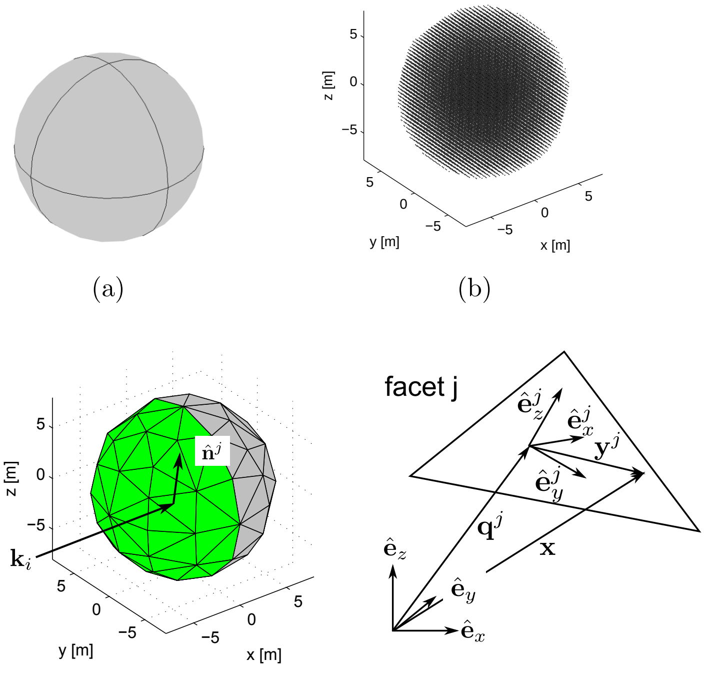

(a) (b)

(c) (d)

Figure 35: (a) General phononic crystal shape. The radius of the sphere is 12 m. (b) The spherical phononic crystal containing 104,312 bubbles evenly spaced with period $a = 0.4$ m. (c) The surface mesh of the PC decomposed into facets. The ensonified facets are shaded green. (d) Definition of the global and local coordinate system for facet j.

To begin with the scattering solution, the incident wavevector is transformed into the facet's local coordinate system

$$\mathbf{k}_i^j = \mathbf{R}^j \mathbf{k}_i. \tag{98}$$

Similarly let $P_0^j = \exp i\mathbf{k}_i \cdot \mathbf{q}^j$ be the complex amplitude of the incident wave (assuming unit amplitude) on the j-th facet. For each facet in Γ, the Bloch wave expansion can be calculated in the local coordinate system of Fig. 35d using the frequency ω and wavenumber parameters $\{k_{iy}^j, k_{iz}^j\} = \{\mathbf{k}_i^j \cdot \hat{\mathbf{e}}_y^j, \mathbf{k}_i^j \cdot \hat{\mathbf{e}}_z^j\}$ as inputs. In practice, the fields from the BWE process can be stored *a priori* and then later accessed as a look-up table operation. Furthermore, for computational time savings, symmetry of the facets can be exploited where applicable.

Following the solution of the BWE for all NF facets, the pressure and particle velocity fields are calculated on each facet at global facet surface points $\mathbf{x}_S^j$. One must remember, due to the coordinate transform, that the scalar pressure transforms as $p(\mathbf{x}_S^j) = p(\mathbf{y}^j)$ and the gradient transforms as $\nabla p(\mathbf{x}_S^j) = \mathbf{R}^T \nabla p(\mathbf{y}^j)$. The scattered pressure from the set of facets is an extension from Eq. (92)

$$p_s\left(\mathbf{x}_f\right) = \sum_{j=1}^{NF} P_0^j \int_{\Gamma^j} \left[G\left(\mathbf{x}_f | \mathbf{x}_S^j\right) \nabla p\left(\mathbf{x}_S^j\right) - p\left(\mathbf{x}_S^j\right) \nabla G\left(\mathbf{x}_f | \mathbf{x}_S^j\right)\right] \cdot \hat{\mathbf{n}}^j \;\, \mathrm{d}\Gamma^j. \tag{99}$$

The equations in Sec. 3.4 assume an incident wave of unit amplitude; the value P_0^j in Eq. (99) scales the fields on each facet correctly. The theory in this section is closed by noting that the FMM software package in Ref. [27] can also be used to evaluate Eq. (99) (and equivalently Eq. (92)); see Appendix C. An experimental speedup of 20 to 50 times has been observed using the FMM as opposed to performing the numerical integration directly.

4.6.2 Verification

To verify the facet formalism, the geometry considered is trivial (in terms of complexity): a cube. The cubic PC of 8,000 bubbles will be used for verification. See for verification of the regular BWE and HKI versus SCS for the same geometry. Construction of a surface mesh yields 72 facets with 12 active; the surface mesh element size was arbitrarily set. Setting $\omega = 3{,}000$ rad/s the scattered pressure is computed using the 12 facets. All 12 facets posses $\hat{\mathbf{e}}_x^j = \hat{\mathbf{e}}_x$ and the BWE discussed in Ch. 3 with $\theta = 90°, \phi = 0°$ can be used. Further, since all 12 facets posses $\hat{\mathbf{e}}_x^j = \hat{\mathbf{e}}_x$, only one BWE calculation needs to be performed; thus, exploitation of the geometry symmetry allows a computational time savings. The facet formalism is compared directly against the SCS technique; the amplitude is shown for the facet and SCS results, respectively, in Fig. 36a and Fig. 36b.

Clearly, the facet technique shows a very similar scattered field amplitude versus SCS; even the near field behavior is accurately predicted. The facet size (square root of area) is less than a wavelength, which is contrast with an assumption discussed in Sec. 4.6.1. Nevertheless, the facet results indicate positive agreement. Therefore, depending on the geometry, the facet size may be on the order of a wavelength and still yield an accurate scattered field. This property, for example, may be exploited to achieve accuracy with complex geometry requiring small surface mesh elements.

4.6.3 Limitations

It serves the reader to discuss a limitation of the presented facet theory. A modeling feature not captured by the above formulation is that the actual PC possesses bubbles arranged on the global axes $\{\hat{\mathbf{e}}_x, \hat{\mathbf{e}}_y, \hat{\mathbf{e}}_z\}$ while each facet treats the bubbles arranged on the *local* axes $\{\hat{\mathbf{e}}_x^j, \hat{\mathbf{e}}_y^j, \hat{\mathbf{e}}_z^j\}$. Figure 37 illustrates this idea: for facet j, the modeled geometry possess an inward normal equal to $\hat{\mathbf{e}}_x^j$ yet the *actual* PC model contains bubbles oriented as shown in Fig. 17a. In a cubic PC, the global and local axes coincide perfectly and the results in Sec. 4.6.2 confirmed the facet technique agrees very well with the direct HKI implementation and SCS technique. In the facet approach, applied to the example geometry in Fig. 35a and many other PC geometry

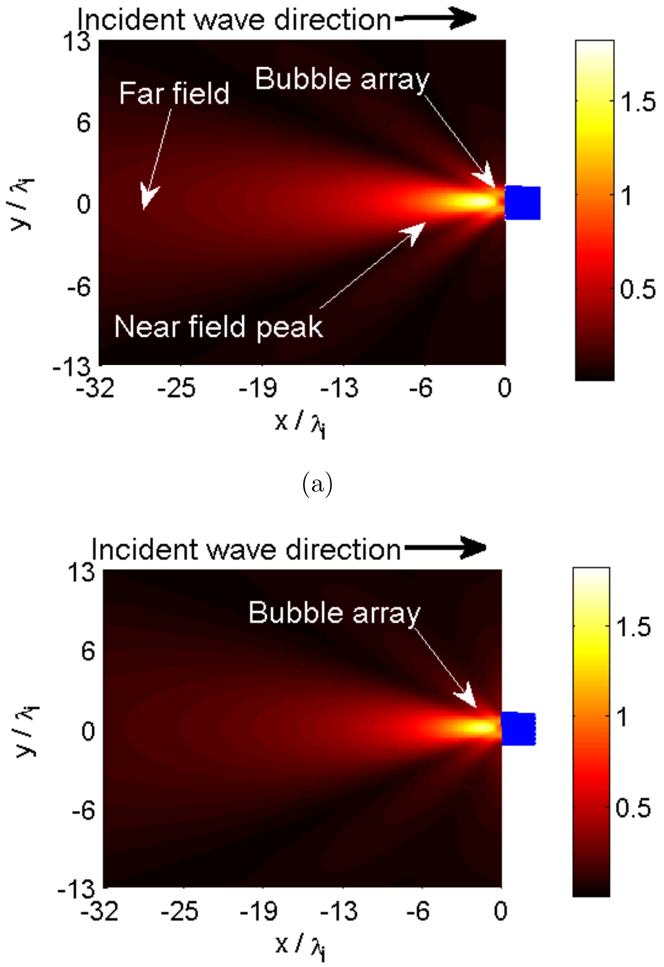

(a)

(b)

Figure 36: Amplitude of the scattered pressure field for (a) facet and (b) SCS. The bubble array is colored in blue for clarity and only backscattering is considered, thus $x < 0$. The incident plane wave at $\omega = 3{,}000$ rad/s strikes the PC in the direction shown and the range is normalized by the incident wavelength λ_i

possibilities, the two sets of axes do not align for most facet orientations.

For the present formulation to work, the frequency ω must be within the first band gap of the PC. Since this band gap is complete (band gap exists for all incident wave directions), the field will be decay in space regardless of the orientation of the local facet axes. This decaying field feature aids in the determination of the scattered pressure, via the facet approach, despite this axis orientation issue. Despite this facet orientation limitation, the facet scattering approach and results (see Sec. 6.3)

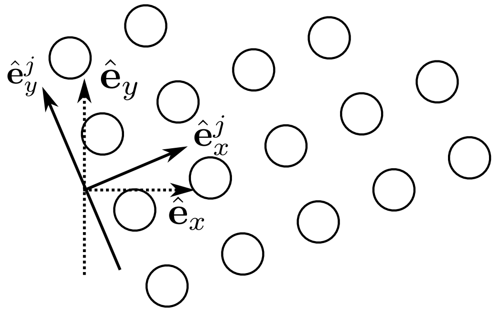

Figure 37: The modeled PC for facet j contains bubbles arranged as shown with the coordinate system $\hat{\mathbf{e}}_x^j$ and $\hat{\mathbf{e}}_y^j$. This coordinate system does not agree, in general, with the *actual* alignment of the PC axes $\hat{\mathbf{e}}_x$ and $\hat{\mathbf{e}}_y$.

demonstrate a promising direction for scattering computations from arbitrary PCs. Future work would address modification of the presented theory to be applicable to a set of ensonified facets while the orientation of the bubble inclusions is correctly represented along the PC's axes.

4.7 Conclusion

In this chapter, the scattering from finite PCs was discussed at length. The Helmholtz-Kirchhoff integral combined with the 2D or 3D Bloch wave expansion allows the scattering to be determined. Several verification studies were presented in both 2D (versus FEM) and 3D (versus SCS). Further, the BWE+HKI was found to be most accurate for field points within the main backscattered beam and when ω resides in a frequency band gap. The transient scattering of the PC from an incident broad band pulse was also discussed. Extending to non-cubic geometries, the facet formalism was introduced and verification examples were presented. The contributions of this chapter to the literature are (i) introduction of the BWE+HKI to study scattering from 2D and 3D finite PCs; (ii) the layer BWE being applied, with the HKI, to study transient scattering from Fourier superposition; and (iii) the capability to study scattering from PCs with complicated geometry via the facet formalism applied when

ω is within the local resonance band gap. Different from the current and previous two chapters, the next chapter discusses the BWE and scattering when the underlying PC contains weak disorder.

CHAPTER V

WEAK INTERNAL DISORDER

5.1 Overview

In this work the application to the previously discussed theory will be for the application to disordered PCs. Along with the BWE+HKI, the content from this chapter pushes the theory forward to be able to study scattering from realistic fish schools. First, in 2D and 3D, the BWE+HKI (strictly valid for a perfectly ordered system) will be applied directly to describe the scattered pressure field from a *real* PC with weak internal disorder; several verification studies are presented. Next, a newly developed perturbation formalism, which may offer the ability to correct the BWE fields for disordered systems, will be introduced.

5.2 Description of disorder

In this work, weak disorder is considered and characterized by the quantity τ. In the respective FEM and SCS models, explicitly, contain weak disorder in the position and radius of the scattering inclusions. In each disordered PC the position and size (radii) of each cylindrical (or spherical) inclusion is chosen to follow a Gaussian distribution with, respectively, mean of a, R and a standard deviation of $\tau a, \tau R$. For convenience, and without loss of generality, the material properties are not altered in this work. For example, Fig. 38 shows two disordered PCs. Of note, the 'strength' of disorder is indeed relative to the wavelength. Physically, the wave field inside the PC may be strongly affected by disorder when ω is high versus a case when ω is low. Lastly, in all studies in this work dealing with the scattering from disordered phononic crystals, only one realization of the disordered PC is considered. Thus, there is no averaging

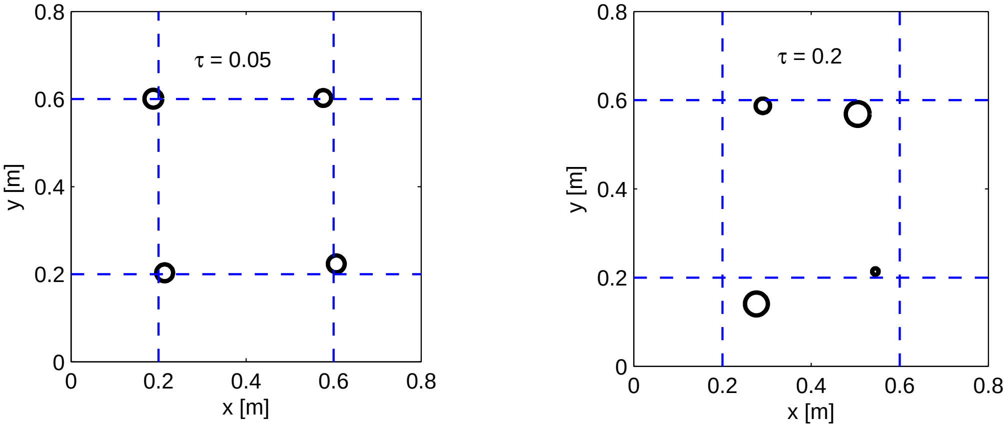

(a)
(b)

Figure 38: A representative two-dimensional disordered PC with (a) $\tau = 0.05$ and (b) $\tau = 0.2$. The intersection of the dashed blue lines indicate the ideal cylinder positions.

of any of the results for different configurations.

5.3 Scattering from disordered PCs

In this section the scattered field is computed using the previously discussed 2D and 3D tools for varying frequencies and disorder levels. Recall, the Bloch theorem, and associated BWE strictly apply to perfectly disordered PCs. However, for *weakly* disordered PCs, the scattered field, predicted using the appropriate BWE and HKI technique, is compared directly to the disordered PC. That is, to approximate the scattered field from a weakly disordered PC the Bloch wave expansion may be used. The following 2D and 3D verification sections qualitatively explore the error exhibited using this approximation. If the disorder is strong enough, the Bloch theorem and HKI technique may yield erroneous results; thus, higher disorder is not studied in this work.

5.3.1 Verification in two dimensions

In this effort the acoustic scattering is determined form a finite phononic crystal with weak internal disorder. The disordered PC consists of cylindrical air-filled inclusions placed in a water background; positional and size disorder of the cylinders is considered. The approach presented herein serves as a formalism for calculating the scattered acoustic pressure from a large finite PC with weak internal disorder.

To establish the validity of the formalism the scattered field from a finite PC, with varying degrees of weak internal disorder, is compared against the scattered field of an ideal PC. An incident plane wave, of unit amplitude, is normally incident on the PC and the frequency $\omega = 13{,}000$ rad/s is within a band gap of the 2D infinite PC. Finite element models are constructed to model the scattering from the disordered PCs and a numerical implementation of the Helmholtz-Kirchhoff integral produces the desired scattered field of the finite disordered PC. A two-dimensional PC is considered that contains 400 air-filled cylinders in water where, in the ideal case, each cylinder is arranged on a square lattice with periodicity $a = 40$ cm and radius $R = 2$ cm.

The scattered acoustic field is illustrated in Figure 39 for field points $x_f \in [-5,\ 0]$ and $y_f = 0$. Similarly, the scattered field is compared for field points within a rectangular region in Figure 40. The scattered acoustic field of the ideal PC, determined by the BWE and Eq. (92), is compared to the scattered pressure from three PCs with varying degrees of disorder characterized by τ and favorable agreement is demonstrated in all results. Additionally, the results for $\tau = 0.1$ in Figure 40, indicate some divergence in spatial scattering character versus the ideal BWE approach. For both results in Fig. 39 and Fig. 40 , the imaginary component of the scattered pressure field follows a similar trend. For the values of τ considered the max deviation from the mean for position, normalized by the wavelength in water $\lambda_i = 0.72$ m, is $\{0.0471,$ $0.08, 0.16\}$ for position and $\{0.0026\ 0.0047\ 0.005\}$ for inclusion radii. In particular, at $\tau = 0.1$ the normalized positional deviation of 0.16 certainly challenges the notion of 'weak' disorder. Further investigation of the scattered field results indicate that the ratio of scattered power to incident power is $\{95\%, 94\%, 88\%\}$. Nearly all acoustic power will be reflected by the PC because the frequency ω is in a band gap [42];

the BWE yields a power ratio of 99.9%. The very high ratios presented for all three disordered PCs corroborate with the predicted qualitative behavior. It is also noted,

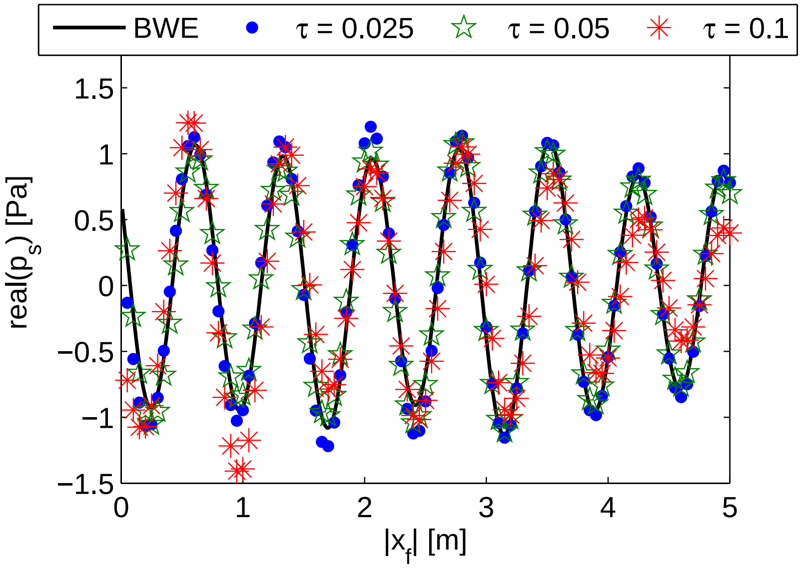

Figure 39: Comparison of the real component of the scattered pressure field over a line with $y_f = 0$ for three PCs with varying internal disorder.

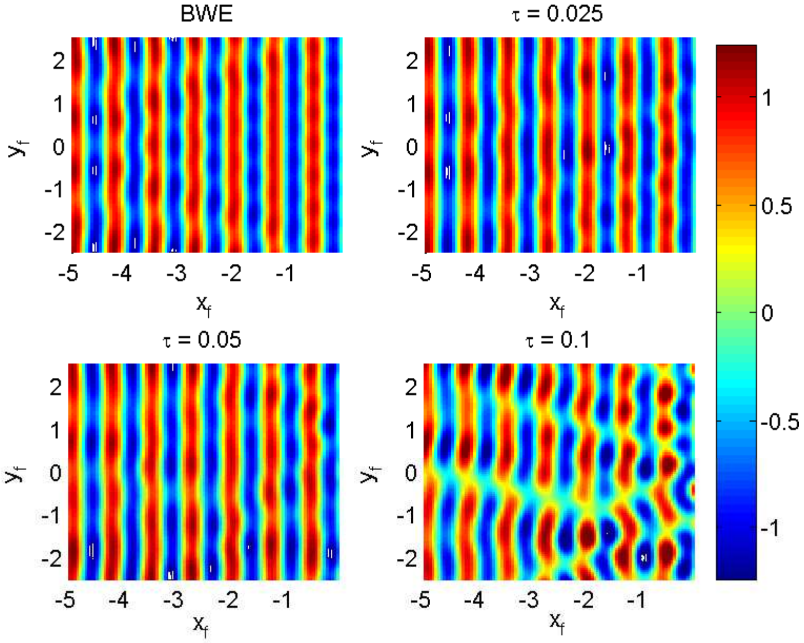

Figure 40: Comparison of the real component of the scattered pressure field over a rectangular region in the xy plane for the BWE solution applied to a ideal PC and three PCs with varying internal disorder.

in the acoustic far field on the line $y_f = 0$ for $x_f <$ -100 m, the real scattered pressure between the ideal PC and PCs with $\tau = 0.025$ and 5% agree excellently in amplitude and phase. The $\tau = 0.1$ PC exhibited an amplitude error of about 17% with a very good agreement in phase.

The results presented herein indicate very good agreement between the scattered pressure from an ideal PC, using the BWE solution, and three PCs with varying levels of weak internal position and size disorder. The results indicate, at this frequency, the degree of internal disorder is small enough such that the BWE combined with the Helmholtz-Kirchhoff integral can adequately predict the scattered pressure from a finite PC with weak disorder. The approach is considered promising for future research and applications into determination of acoustic scattering from finite PCs with varying shape effects and internal disorder.

Next, the two-dimensional half-space BWE is used to compute the scattered pressure field over a large frequency range and the results are compared against the FEM model. The relative error in scattered amplitude at a single point 10 m from the PC is shown in Fig. 41. Notably, for all three disordered PCs the error is lowest in the first band gap. The increased error as τ increases, in the second band gap is a result of the higher frequency. Clearly, outside of the band gap range, the half-space BWE predicts very high error. Application of the layer BWE does not significantly alter the results. A conclusion is seen: the best agreement in the scattered field is found when ω is in a frequency band gap. Here the decaying nature of the internal wave field aids in the BWE+HKI approximating the pressure scattered by the disordered PC. Thus, the BWE+HKI approach is most robust in a frequency band gap for determination of the scattered pressure field from a disordered PC.

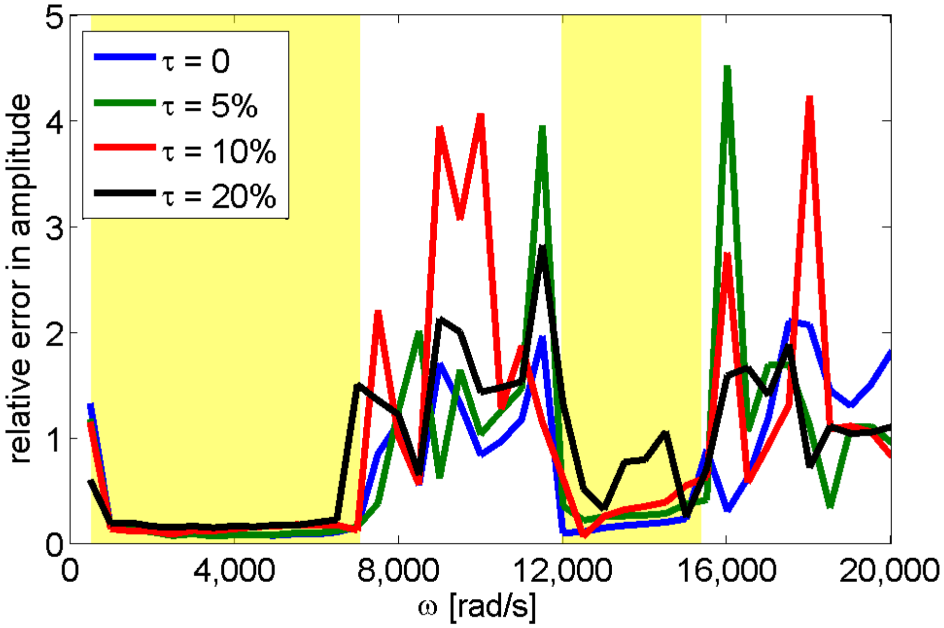

Figure 41: Comparison of the relative error versus frequency in the scattered pressure at a single point using the BWE+HKI versus the FEM applied directly to four disordered PCs with varying τ. The band gap ranges are highlighted.

5.3.2 Verification in three dimensions

Of first interest is exploring how the SCS predicted TS values are altered by the presence of disorder. To explore the robustness of the target strength values within the first and second band gaps, a parametric study is performed using a PC with weak disorder. Consider the cubic PC of 8,000 bubbles, but with varying τ varying from 0 to 0.2. For three values of $\tau = \{0, 0.1, 0.2\}$ the target strength is shown for the first and second band gaps in, respectively, Fig. 42a and Fig. 42b. At each disorder level, only a single realization of the PC is considered. Negligible differences between the ideal τ $= 0$ and disordered TS curves are observed in Fig. 42a. The local resonance band gap is more robust to phase differences caused by disorder than the Bragg scattering band gap. A separate numerical experiment has confirmed, for a positional disorder level of $\tau = 0.5$, the internal scattered field and the target strength are changed little from disorder. The Bragg band gap depends on the phase interference of the incident and

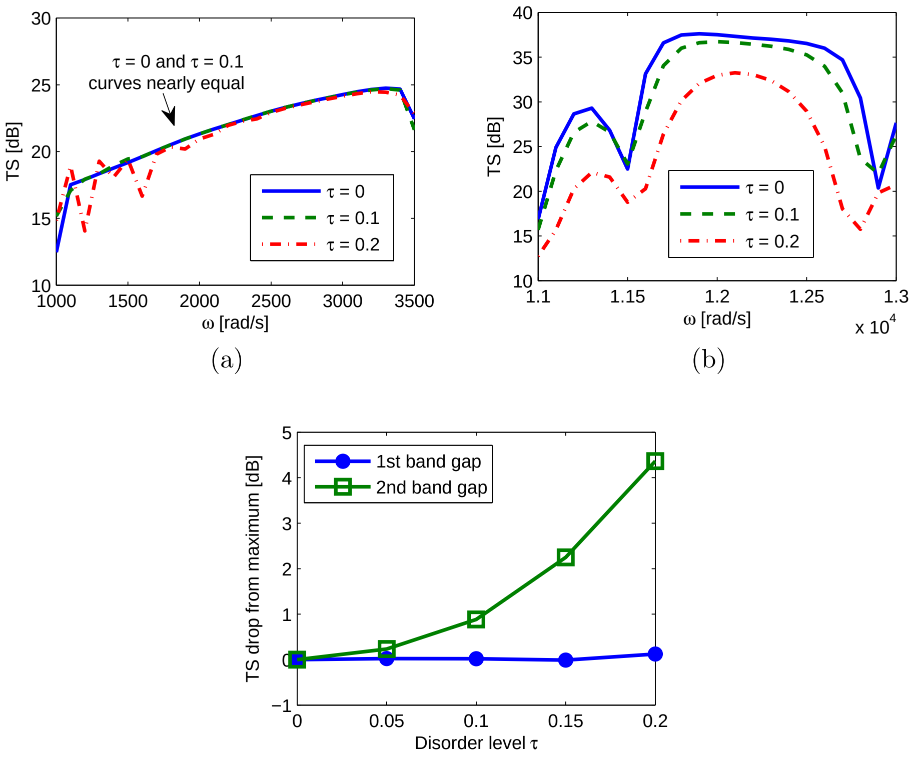

(a) (b)

(c)

Figure 42: The target strength for PC A with varying levels of weak position and size disorder; τ characterizes the standard deviation from the ideal PC. The (a) first and (b) second band gap frequency range is studied. (c) As τ is increased, the difference between the ideal and disordered PC in the first (blue) and second (green) band gap frequency range.

scattered wave; disorder can break this wave interference. In Fig. 42b, in the second band gap, the $\tau = 0.2$ curve is lower than the ideal case by approximately 5 dB. Over five τ values, the decrease in the TS maximum from the ideal case is illustrated in Fig. 42c. Again, negligible change in the TS is observed in the first band gap range. The introduction of weak disorder clearly alters the maxima for the target strength within the second (Bragg) band gap. Extrapolation from Fig. 42c suggests that a large decrease in target strength in the second band gap, for instance over 30 dB, can be observed for PCs with τ increasing beyond 0.5; this circumstance is no longer considered 'weak' disorder.

Next, at two band gap frequencies, the scattered pressure field is computed at NP

= 1,000 field points using the BWE+HKI technique and compared directly against the SCS technique applied to the disordered PCs. It was concluded in Ch. 4 and Ref [43] that the best BWE+HKI performance, for accuracy in the amplitude and phase of the scattered field, occurs when the field points are within the main backscattered beam. Thus, the points reside within the xy plane, in the acoustic far field, along the $\hat{\mathbf{e}}_x$ direction. At each frequency (ω = 3,000 and 12,000) an error in amplitude (E_{amp}) and phase (E_{phase}) can be computed from Eq. (96)

The error is computed for the ideal PC (using the BWE) and the four disordered PCs (using SCS) and shown for amplitude and phase in, respectively, Fig. 43a and Fig. 43b. In the first band gap, the amplitude error is constant at 0.08 and the phase increases to an error of 0.7. In the second band gap, the amplitude error increases to a maximum of 0.28 whereas the phase error increases to 1 (phase difference of π). This error study informs one of a key fact: the pressure field amplitude predicted via the BWE+HKI, compared to the actual field scattered by a disordered PC, exhibits lowest error in the first band gap. This statement is in accordance with the conclusion in the prior section.

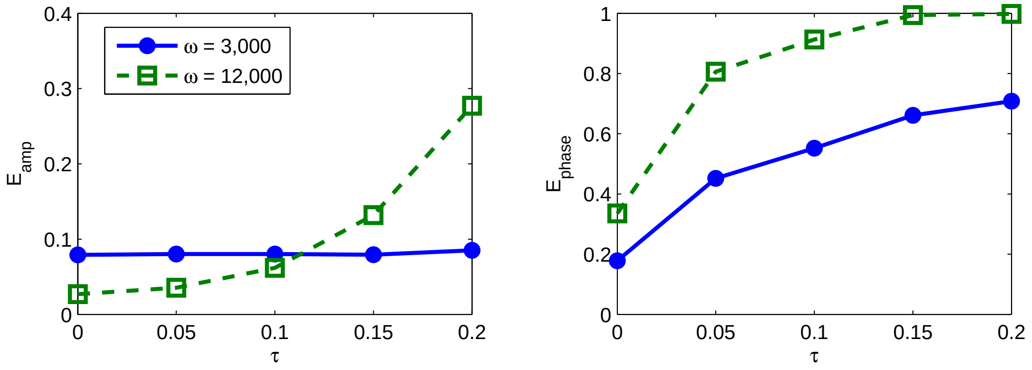

(a)

(b)

Figure 43: Error in (a) amplitude and (b) phase for the scattered field computed with the BWE+HKI techniques versus the SCS technique applied to disordered PCs. The computations are performed at two band gap frequencies.

5.4 Perturbation formalism

In the growing field of phononic crystals (and the electromagnetic equivalent, photonic crystals) there is a great wealth of literature regarding different dispersion techniques and the experiments for certain applications. However, presently, to a smaller degree, exists literature describing the wave propagation within the weakly disordered structures. At this point a brief review of some other techniques is useful. Caleap *et al.* [7], via a complex theoretical technique, investigated the low frequency effective properties of acoustic metamaterials with random disorder. Both Collins and Thompson [10] and Shinozuka and Astill [76] considered the effect of random disorder on the eigenvalues of ordinarily ordered structural systems. In photonic crystals, Li *et al.* [54] considered the effect of disorder on the $\omega(\mathbf{k})$ dispersion relationship via averaging over a set of cells. Bendiksen [4] studied localization phenomena in structural dynamics. His work contains theoretical treatment into the differential equations governing systems with 'almost' periodic coefficients and provides a review of perturbation methods applied to said systems.

In this section a perturbation formalism for weakly disordered phononic systems is introduced. Strictly, the Bloch theorem does not apply to disordered systems. However, as pointed out in Bendiksen [4] and originally by Anderson (known for his work on Anderson localization) [2], a perturbation formalism can be applied to the nominal, perfect, system. A multiple-scales analysis has been applied to nonlinear periodic systems [62]. In the spirit of that work, a multiple-scales analysis is applied to a *linear* system with weak disorder. In this light, the perturbation is introduced into the mass and stiffness matrices that govern the system. Depending on the frequency, a correction to the $\omega(\mathbf{k})$ dispersion relationship is sought after. Thus, it is anticipated a perturbation technique can be used to accurately study the steady state wave propagation within the weakly disordered material. The theoretical development for one-dimensional (1D) and multi-dimensional (2D and 3D) systems will be presented next.

5.4.1 One-dimensional Periodic System

5.4.1.1 Equations of motion

First, consider a one-dimensional, infinitely long, and periodic chain with ND degrees of freedom per unit cell. The development herein is intended to be for arbitrary ND one-dimensional systems. For the sake of presentation, and without loss of generality, the development is presented with $ND = 2$; thus the system is a diatomic chain. See Fig. 44 for an example.

The time harmonic differential equations governing the system dynamics are

$$\begin{aligned} -\omega^2 m_1 u_j + (k_1 + k_2)u_j - k_2 v_{j-1} - k_1 v_j = 0 \\ -\omega^2 m_2 v_j + (k_1 + k_2)v_j - k_1 u_j - k_2 u_{j+1} = 0 \end{aligned} \tag{100}$$

where the j-th unit cell contains masses m_1, m_2, springs k_1, k_2 and displacement u_j, v_j; see Fig. 44. The interaction of the neighbors at the $j-1$ and $j+1$ cell is contained within the equations. In matrix form, the system reads:

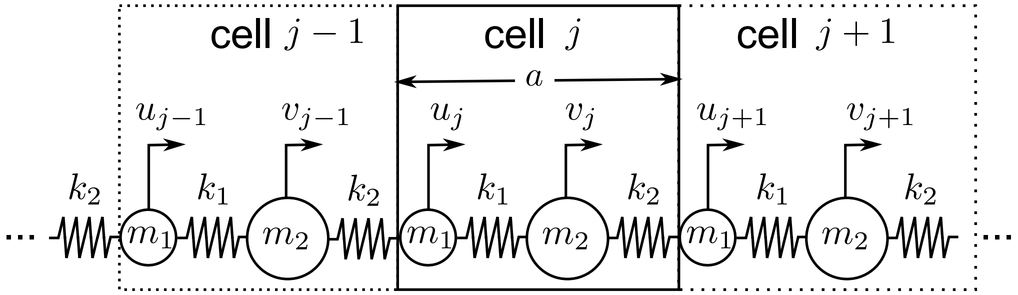

Figure 44: Diagram of the diatomic chain model. Each unit cell contains two masses m_1, m_2 and springs k_1, k_2. The displacement of the two masses in the j-th unit cell are respectively described by u_j and v_j. The reference cell j is drawn with it's left $j-1$ and right $j+1$ neighboring cells.

$$\begin{aligned} -\omega^2 \begin{bmatrix} m_1 & 0 \\ 0 & m_2 \end{bmatrix} \begin{bmatrix} u_j \\ v_j \end{bmatrix} + \begin{bmatrix} 0 & -k_2 \\ 0 & 0 \end{bmatrix} \begin{bmatrix} u_{j-1} \\ v_{j-1} \end{bmatrix} + \\ \begin{bmatrix} k_1+k_2 & -k_1 \\ -k_1 & k_1+k_2 \end{bmatrix} \begin{bmatrix} u_j \\ v_j \end{bmatrix} + \begin{bmatrix} 0 & 0 \\ -k_2 & 0 \end{bmatrix} \begin{bmatrix} u_{j+1} \\ v_{j+1} \end{bmatrix} = \begin{bmatrix} 0 \\ 0 \end{bmatrix}. \end{aligned} \tag{101}$$

The equations are further manipulated into matrix form

$$\sum_{j=-1}^{1} \left(-\omega^2 \mathbf{M}_j + \mathbf{K}_j\right) \mathbf{v_j} = \mathbf{0}. \tag{102}$$

where $\mathbf{M}_j, \mathbf{K}_j$ are the mass and stiffness for cell j and $\mathbf{v}_j = [u_j \ v_j]^T$. Based on the matrix equation in Eq. (101), the terms in Eq. (102) can be readily identified. Note, since the identity of the j-th cell is arbitrary, it is sufficient to define the summation for $j = -1, 0, +1$. The benefit to the specific form of the prior matrix equation will be seen shortly.

For an ideal periodic system, the Bloch theorem from Eq. (1) can be written in matrix form as

$$\mathbf{v}_j = \mathbf{q} \exp i\mu j \tag{103}$$

where μ is a (possibly) complex propagation constant and can also be written as $\mu = ka$ where a is the width of the unit cell and $\mathbf{q}$ is the Bloch eigenvector. It is of note, this matrix form of the Bloch theorem is similar to the $\omega(\mathbf{k})$ dispersion technique presented in Appendix B. Insertion of the Bloch theorem in Eq. (102) yields the following equation that governs the wave dynamics in the perfectly periodic chain

$$\sum_{j=-1}^{1} \left(-\omega^2 \mathbf{M}_j + \mathbf{K}_j\right) \mathbf{q} \exp i\mu j = \mathbf{0}. \tag{104}$$

With $\mu = ka$, the ND eigenvalues ω and eigenvectors $\mathbf{q}$ describe the $\omega(k)$ dispersion relationship of the diatomic chain.

5.4.1.2 Capturing dispersion change via perturbation

With constant masses and springs, the dispersion relationship of the one-dimensional system is given by Eq. (104). However, now disorder will be introduced into the mass and springs. In particular, let,

$$\begin{aligned} m_j &= m_j^0 + \epsilon m_j^1 \\ k_j &= k_j^0 + \epsilon k_j^1 \end{aligned} \tag{105}$$

In the preceding equation, the uniform mass and stiffness are respectively given by m_j^0, k_j^0. In the following development in this Chapter, the superscript '0' denotes the uniform quantities and the superscript '1' denotes an additional perturbation of the mass/stiffness. The quantity ϵ is a small non-dimensional constant. Note also that the disorder is allowed to vary for different cells, indicated by the subscript on m_j^1, k_j^1. Since a cell's neighbors will be used in the calculation and the reference cell location is arbitrary, it is implied that a disorder-induced phase difference will be valued for the j-th cell. Further, the local wave propagation can be described the the phase difference associated with the j-th cell. The computations can be repeated for various cells, with different mass and springs disorder values, to give an overall phase picture of the chain.

Building from the previous disordered mass and stiffness, let the matrices of the system follow a similar trend with

$$\begin{aligned} \mathbf{M}_j &= \mathbf{M}_j^0 + \epsilon \mathbf{M}_j^1 \\ \mathbf{K}_j &= \mathbf{K}_j^0 + \epsilon \mathbf{K}_j^1 \end{aligned} \tag{106}$$

Next, insert the perturbed matrices into the governing matrix equation (Eq. (102)) for the j-th cell and it's neighbors. The result is

$$\sum_{j=-1}^{1} \left[-\omega^2 \left(\mathbf{M}_j^0 + \mathbf{M}_j^1 \right) + \left(\mathbf{K}_j^0 + \mathbf{K}_j^1 \right) \right] \mathbf{v_j} = \mathbf{0}. \tag{107}$$

In an ideal linear system, the phase change stipulated by the Bloch theorem (in matrix form) can be written as

$$\mathbf{v}_j = \mathbf{q}e^{i\mu j} = \begin{bmatrix} e^{i\mu j} & 0 & 0 & 0 \\ 0 & e^{i\mu j} & 0 & 0 \\ 0 & 0 & ... & 0 \\ 0 & 0 & 0 & e^{i\mu j} \end{bmatrix} \mathbf{q} \tag{108}$$

As stated earlier, it is assumed that the presence of weak disorder alters the Bloch phase, which leads to a change in dispersion; the eigenvector $\mathbf{q}$ is unaltered. The change in dispersion - the dispersion correction - is the sought after quantity. Since the system is linear, the frequency ω does not change; however, the phase that exists between neighboring cells will change. When $ND = 1$, this phase can be considered to have a perturbed component as $\mu_j = \mu^0 + \epsilon\mu_j^1$. However, for $ND > 1$, there must be a phase change for *each* degree of freedom. For example, for $ND = 2$, the perturbed phase is $\mu_1 = \mu^0 + \epsilon\mu_1^1$ and $\mu_2 = \mu^0 + \epsilon\mu_2^1$. In this light, the Bloch theorem for the weakly disordered mechanical system is taken as

$$\mathbf{v}_j = \begin{bmatrix} \exp i(\mu^0 + \epsilon\mu_1^1)j & 0 & 0 & 0 \\ 0 & \exp i(\mu^0 + \epsilon\mu_2^1)j & 0 & 0 \\ 0 & 0 & ... & 0 \\ 0 & 0 & 0 & \exp i(\mu^0 + \epsilon\mu_{ND}^1)j \end{bmatrix} \mathbf{q} \tag{109}$$

where it is clear that the phase of the ideal model μ^0 does not vary by node; μ_j^1 does vary by node. If the disorder is weak, the exponential term an be *linearized* and the j-th phase term can be written as

$$\exp i(\mu^0 + \epsilon\mu_j^1)j \approx \left(1 + i\epsilon\mu_j^1 j\right) \exp i\mu^0 j \tag{110}$$

Insertion of this form into the prior matrix equation gives the result

$$\mathbf{v}_j = (\mathbf{I} + \epsilon ij\mathbf{\Lambda}) \exp i\mu^0 j \tag{111}$$

In the above equation, the matrix $\mathbf{\Lambda}$ is diagonal with components $\Lambda_{mn} = \mu_m^1\delta_{mn}$. Insertion of Eq. (111) into the general expression of Eq. (102) results in an ordered equation in powers of ϵ. At zeroth order, the dispersion relationship from Eq. (104) is obtained and can be solved for $\omega(\mu^0)$ and $\mathbf{q}(\mu^0)$. At first order, the matrix equation reads

$$O(\epsilon^1): \underbrace{\sum_{j=-1}^{1} \left(-\omega^2 \mathbf{M}_j^1 + \mathbf{K}_j^1\right) \exp i\mu^0 j\, \mathbf{q}}_{\mathbf{D}^1} + \underbrace{\sum_{j=-1}^{1} i \left(-\omega^2 \mathbf{M}_j^0 + \mathbf{K}_j^0\right) j \exp i\mu^0 j\, \mathbf{q}'}_{\mathbf{D}^0} = \mathbf{0}. \tag{112}$$

which can be further simplified to

$$\mathbf{D}^1(\mu^0)\mathbf{q} + \mathbf{D}^0(\mu^0)\mathbf{q}' = \mathbf{0} \tag{113}$$

where the vector $\mathbf{q}' = \mathbf{\Lambda q}$. This matrix equation can then be solved, e.g. $\mathbf{q}' = -(\mathbf{D}^0)^{-1}\mathbf{D}^1\mathbf{q}$. Finally, since the matrix $\mathbf{\Lambda}$ is diagonal, the phase perturbation for each degree of freedom can be obtained simply by $\mu_j^1 = q_j'/q_j$. In equation form this process reads

$$\mu_j^1 = \frac{\left(-(\mathbf{D}^0)^{-1}\mathbf{D}^1\mathbf{q}\right)_j}{q_j} \tag{114}$$

where the subscript j in the numerator indicates the j-th component of the vector. The disorder-induced change, for node j, to the dispersion relationship can be reconstructed from the prior perturbation analysis

$$\mu_j = \mu^0 + \epsilon \mu_j^1 \tag{115}$$

5.4.1.3 Results

At present, only results for a monatomic chain exist. Thus, the result presented here is merely a snapshot of the above theory applied to a simple monatomic ($ND = 1$). The dispersion perturbation analysis from Eq.(113) simplifies and the first order phase perturbation reads

$$\mu_j^1 = \frac{m_j^1 \omega^2 - 2k_j^1 \left(1 - \cos \mu^0\right)}{2k_j^0 \sin \mu^0} \tag{116}$$

The verification study considers a monatomic chain with the forcing frequency $\omega = 1$ rad/s, a mass equal to 2 kg, stiffness equal to 1 N/m, and, without loss of generality, variations in the stiffness along the chain. Over the length of 600 cells, the stiffness values are fixed at a range of 20 cells; there are 30 groups of cells with varying stiffness. Verification [51] was accomplished by considering a spectrogram of a direct numerical implementation of the differential equation; see Fig. 45. The predicted wavenumber ($k = k^0(\omega) + \epsilon k^1$) is overlaid on top.

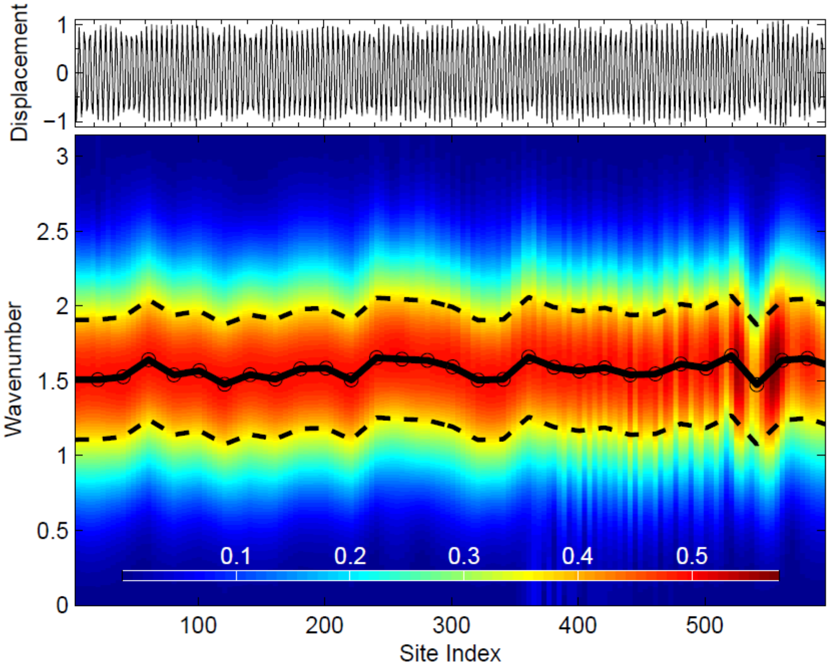

Figure 45: Spectrogram for the monatomic random chain. The perturbation result is shown as a solid line with and the dotted lines are used to bound the wavenumber peak predicted from the perturbation analysis. The site index corresponds to the j-th cell along the chain. Image courtesy of M. Leamy and M. Ruzzene [50]

Clearly, the wavenumber perturbation results match with what is predicted by the numerical values. Although the results are for a monatomic case, it is expected the outlined procedure may be verified via a similar path with $ND > 1$. This verification is left to future work.

5.4.1.4 Overview

At present, there is no full verification available for the chain when $ND > 1$. However, when $ND = 1$, analysis of the chain's spectrogram has demonstrated an accurate result. For the diatomic case, and other systems, it is anticipated that the spectrogram or comparison of the spatial amplitude of the wave may provide a means of verification versus direct numerical evaluation of the system's differential equations. This is intended for future work.

Having discussed the intended verification studies, a few questions still remain about the theory's applicability. These will be mentioned here but not explored. First, what is the amount of disorder to consider before the theory breaks? Secondly, numerical experiments (with unsatisfactory results) have revealed the possibility of complex first order phase perturbation results. Since the variation is considered locally, it is expected that unbounded exponential decay will be a non-issue. Thirdly, if the case arises where $q_j = 0$, or the matrix $\mathbf{D}^0$ is singular, then how can the phase correction (see Eq. (114)) be solved for? Lastly, will the presented phase correction work in a frequency band gap? These issues and their resolution must be addressed in order for a disorder-induced phase variation to be accurately captured by this perturbation formalism.

5.4.2 Two-dimensional Periodic System

The extension of the above dispersion correction formalism can be easily extended to 2D or 3D; the 2D case will be presented herein. As in the 1D case, a local dispersion correction (via the phase) for each node is desired.

In analogy with the 1D equation of motion presented in Eq. (102), the equations of motion for a 2D dynamical system consisting of a reference unit cell and 8 neighbors can be represented as

$$\sum_{m=-1}^{1} \sum_{n=-1}^{1} \left(-\omega^2 \mathbf{M}_{mn} + \mathbf{K}_{mn}\right) \mathbf{v}_{mn} = \mathbf{0}. \tag{117}$$

Here the different combinations of indices refer to the reference cell $(m, n = 0)$ and the neighbors, see Fig. 46; this form is an extension from the 1D form presented earlier. In this form, the Bloch theorem takes the form of

$$\mathbf{v}_{mn} = \mathbf{q} \exp i \left(m\mu_x + n\mu_y \right) \tag{118}$$

with the phase components of the Bloch wave, μ_x, μ_y, in the respective x and y directions.

As before, under weak disorder, the Bloch phase components will be perturbed and the first order correction is arrived at after solution of the ordered equation set. However, since there is one matrix equation of motion, it is not possible to arrive at a solution for $\mu^1_{x,j}$ and $\mu^1_{y,j}$ together. Instead, the x and y disorder perturbations are considered separately. That is, the x phase correction will rely on positional disorder *only* in the x direction. It is supposed that a weighted sum of the independently calculated x and y corrections can be used in the case of general positional and size disorder of the inclusion. The following derivation considers only x disorder with the y disorder being identical in formulation.

5.4.2.1 Implementation

Consider a finite element mesh of the ideal model in Fig. 46. The mass and stiffness matrices $\mathbf{M}^0_{mn}$ and $\mathbf{K}^0_{mn}$ can be formulated. Also in Fig. 46, an example disordered model contains a unit cell with the circular inclusion shifted to the right (x disorder). One must remember that there are nine matrix terms (27 in 3D) and each one can have a different realization of the inclusion geometry. From this disordered model one can formulate the matrices $\mathbf{M}_{x,mn}$ and $\mathbf{K}_{x,mn}$. Note the subscript indicates the change is related only to the x direction. Since the quantities of interest are the first order matrix corrections (equivalent of m^1_j in the prior 1D section), one can subtract:

$$\begin{aligned} \mathbf{M}^1_{x,mn} &= \frac{1}{\epsilon} \left(\mathbf{M}_{x,mn} - \mathbf{M}^0_{mn} \right) \\ \mathbf{K}^1_{x,mn} &= \frac{1}{\epsilon} \left(\mathbf{K}_{x,mn} - \mathbf{K}^0_{mn} \right) \end{aligned} \tag{119}$$

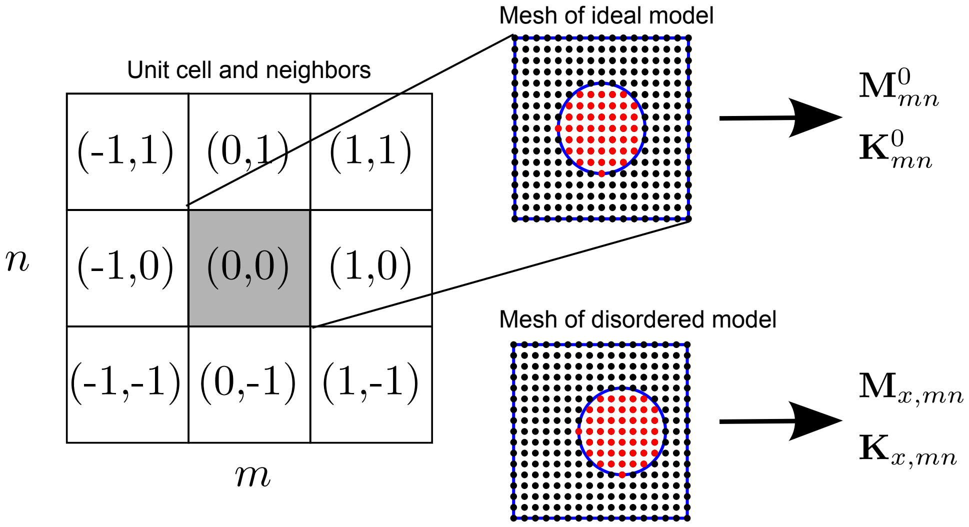

Figure 46: In the 2D model, there is a reference unit cell (shaded gray) and 8 neighboring cells. The indices m, n are listed for reference. A mesh of the ideal and disordered model using square finite elements. The element's nodes are black for material 1 (water host) and red for material 2 (air inclusion). The ideal model yields mass and stiffness matrices $\mathbf{M}^0_{mn}, \mathbf{K}^0_{mn}$. The disordered model features the circular inclusion moved to the right; $\mathbf{M}_{x,mn}, \mathbf{K}_{x,mn}$ can then be formulated.

Note this requires a specific value of ϵ.

A key difference between this 2D disorder formulation and the finite element analysis in the remainder of the Thesis is the mesh of the unit cell. Since a subtraction operation must occur for identification of the first order matrices, the finite element nodal degrees of freedom *must* overlap between the meshes of the ideal and disordered geometry. This stipulation requires a finite element model that contains rectangular elements. Thus, for node j, corresponding mass and stiffness terms for the disordered and ideal models can be obtained. To incorporate a circular inclusion will require a fine spatial resolution of the mesh. In Fig. 46, the two meshes shown are of square elements; clearly the ideal and disordered meshes overlap perfectly. This mesh requirement will extend to three dimensions as well.

5.4.2.2 Capturing dispersion change via perturbation

Expanding on the independence of x and y disorder, and in accordance with the linearization principle discussed in Sec. 5.4.1.2, the first order disorder-induced phase change of the system can be represented in matrix form

$$\mathbf{v}_{mn} = (\mathbf{I} + \epsilon im\mathbf{\Lambda}_x) \exp i(\mu_x^0 m + \mu_y^0 n) \tag{120}$$

where, again, the diagonal matrix $\mathbf{\Lambda}_x$ contains the ND first order phase variations $\mu_{x,j}^1$ valid at each node of the discretized model. The prior equation is for the x disorder; y disorder is allowed by replacing ϵim with ϵin and $\mathbf{\Lambda}_x$ with $\mathbf{\Lambda}_y$. Insertion of this form into the governing matrix equation of Eq. (117) and equating the separate zeroth and first order terms to zero gives a matrix equation

$$\begin{aligned} \mathbf{D}_x^1\mathbf{q} + \mathbf{D}_x^0\mathbf{q}_x' &= \mathbf{0} \\ \mathbf{D}_y^1\mathbf{q} + \mathbf{D}_y^0\mathbf{q}_y' &= \mathbf{0}. \end{aligned} \tag{121}$$

For completeness, the matrix equation leading to the y dispersion change is listed as well. The other matrix terms are

$$\mathbf{D}_x^0(\mu_x^0, \mu_y^0) = \sum_{m=-1}^{1}\sum_{n=-1}^{1} \left(-\omega^2\mathbf{M}_{x,mn}^0 + \mathbf{K}_{x,mn}^0\right) im \exp i(\mu_x^0 m + \mu_y^0 n) \tag{122a}$$

$$\mathbf{D}_x^1(\mu_x^0, \mu_y^0) = \sum_{m=-1}^{1}\sum_{n=-1}^{1} \left(-\omega^2\mathbf{M}_{x,mn}^1 + \mathbf{K}_{x,mn}^1\right) \exp i(\mu_x^0 m + \mu_y^0 n) \tag{122b}$$

$$\mathbf{D}_y^0(\mu_x^0, \mu_y^0) = \sum_{m=-1}^{1}\sum_{n=-1}^{1} \left(-\omega^2\mathbf{M}_{y,mn}^0 + \mathbf{K}_{y,mn}^0\right) in \exp i(\mu_x^0 m + \mu_y^0 n) \tag{122c}$$

$$\mathbf{D}_y^1(\mu_x^0, \mu_y^0) = \sum_{m=-1}^{1}\sum_{n=-1}^{1} \left(-\omega^2\mathbf{M}_{y,mn}^1 + \mathbf{K}_{y,mn}^1\right) \exp i(\mu_x^0 m + \mu_y^0 n). \tag{122d}$$

And as before, $\mathbf{q}_x' = \mathbf{\Lambda}_x\mathbf{q}$ and then $\mu_{j,x}^1 = q_{j,x}'/q_j$; the same equation holds for $\mu_{j,y}^1$. Finally, the disorder-induced change, for node j, to the dispersion relationship can be reconstructed from the prior perturbation analysis

$$\begin{aligned} \mu_{x,j} &= \mu_x^0 + \epsilon\mu_{x,j}^1 \\ \mu_{y,j} &= \mu_y^0 + \epsilon\mu_{y,j}^1 \end{aligned} \tag{123}$$

Although the perturbation analysis has been presented in two dimensions, the theory should extend well to three dimensions, with the introduction of another summation for the 26 neighbors of a unit cell and the introduction of the phase $\mu_{z,j} = \mu_z^0 + \epsilon\mu_{z,j}^1$.

5.4.2.3 Overview

As in the 1D case of Sec. 5.4.1, at present, there is no independent verification study for the 2D perturbation correction approach. As indicated earlier, it is anticipated that analysis of the system's spectrogram, or direct comparison of the displacement variation with the disordered system, may provide an avenue for verification. Within this multi-dimensional disorder framework, the same questions raised in Sec. 5.4.1.4 are at play here. It was speculated but not verified: can inclusion size (and not position) be captured via a sum of the x and y phase corrections. These issues are documented for reference and should be explored in future work.

5.5 Conclusion

In this chapter, the application of the presented theory to weakly disordered PCs was discussed. In two and three dimensions, the applicable BWE and HKI theory for the ideal PC was compared directly against scattering computations for a model with disorder. Several verification studies were presented in both 2D (versus FEM) and 3D (versus SCS). This approach yielded an accurate scattered field predictions; the best agreement was found in the band gap range. Also, the foundation of a perturbation formalism for a correction of the dispersion relationship was presented for 1D and 2D systems. Although verification was not presented, this formalism is anticipated to be useful for future scattering computations. Within this chapter, the (1) scattering from 2D and 3D disordered PCs through using the Bloch wave formalism and (2) a perturbation formalism included with the Bloch theorem for weakly disordered PCs was contributed to the literature.

Pending verification, it is expected that the 2D and 3D perturbation formalism will be combined into the BWE. Thus, the pressure along the surface will be described by the Bloch wave expansion, and feature local adjustments corresponding to the disorder effects. Then the corrected BWE fields may be re-inserted into the HKI and, hopefully, enable improved accuracy for the scattering from disordered PCs. Since the next chapter, with application to fish, uses the BWE directly, this combination of the BWE and perturbation framework is not discussed further but, rather, deferred to future work.

CHAPTER VI

APPLICATION TO FISH SCHOOLS

6.1 Overview

Finally, in this chapter, the scattering from large fish schools will be discussed with regard to the Bloch wave formalism. As emphasized in Ch. 1, the PC is *not* considered to be a fish school. Rather, the previously mentioned tools will aid in the determination of the acoustic scattering. Specifically, the facet formalism of Sec. 4.6 and the concepts discussed in Sec. 5.3 will be combined to yield a complete theory whereby the scattering can be calculated, at an arbitrary point, for a school with fish approximately arranged in a simple cubic packing. First, the frequency dependent target strength will be covered with application to ideal and disordered PCs of shapes; shapes which may represent a fish school. Next, the scattering from a spherical shaped school and a, more complicated, bean-shaped school will be considered. Both studies consider the harmonic and transient scattering using the facet formalism applied to the realistic, weakly disordered school.

Within this chapter there are several tacit assumptions made regarding the fish schools considered. First, all fish are assumed to have identical material properties. Since the scattering is dominated solely by the air-filled swimbladder, more complicated fish bio-acoustic properties are not used (see Refs [56, 21]) as these effects are negligible at within the frequency range considered and omitted for the sake of numerical efficiency. Of typical swimbladder bearing fish, the ratio of the fish's swimbladder to the body is approximately 0.05 [56, 58]. Additionally, the fish body itself is typically modeled as a fluid that is very similar to water [56]. Secondly, weak disorder is considered for the swimbladder's radius and position within the school.

The Bloch formalism may not work with high amounts of disorder. Thirdly, all fish are assumed to have the same heading and orientation and not be swimming. Since the fish body itself is not explicitly modeled; the heading is not important. Also, the fish's movement is very small compared to the speed of sound c_i, thus any Doppler effects attributed to this motion will be negligible. Lastly, depth dependent effects of the air-filled swimbladder are *not* included in the model. This addition is deferred to future work.

6.2 Target strength studies

The results in this section concern the target strength of a PC (or fish school) when the frequency is within a band gap. These results are pertinent for gaining qualitative understand of the target strength for a fish school with varying size and shape. To connect the target strength with physical quantities relevant to the phononics crystals community, it is useful to first explore the pressure and intensity near the PC surface.

6.2.1 Connection between power reflection and target strength

First, a parametric study with respect to ω is done with $NB = 8{,}000$ bubbles in a cube of side length 8 m. At each frequency, the layer BWE [43] is computed and the predicted scattered pressure is compared directly against the SCS technique. The pressure reflection coefficient ($R_P = |p_s/p_i|$) is shown in Fig. 47a where p_i is the complex value of the incident pressure at the interface. The power reflection coefficient, Eq. 75, is shown in Fig. 47b. The plot indicates similar frequency dependent behavior with R_P. Since there is no energy transfer into the PC in the band gap frequencies, the pressure and power reflection coefficients are predicted to be unity in the two band gaps; the numerical data confirms this. When the frequency is lower than 1,200 rad/s, the wavelength in water λ_i is greater than the PC length and the pressure/power reflection coefficient, computed with the SCS technique, is greater than one. Figure 47c illustrates the frequency dependent target strength. Notably, the target strength in the first band gap is greater than that of the second band gap. The higher TS in the second versus first band gap does not conflict with the notion that $R_W = 1$ in both band gaps. Rather, the pressure/power reflection coefficients are related to a semi-infinite half-space phononic crystal, while the target strength is related to the a finite sized PC. As discussed in Ch. 4, the alternating maxima/minima between the band gaps are related to the PC length; this observation is an example of the phase closure principle [57]. Further exploration and observation of the target strength is explored next.

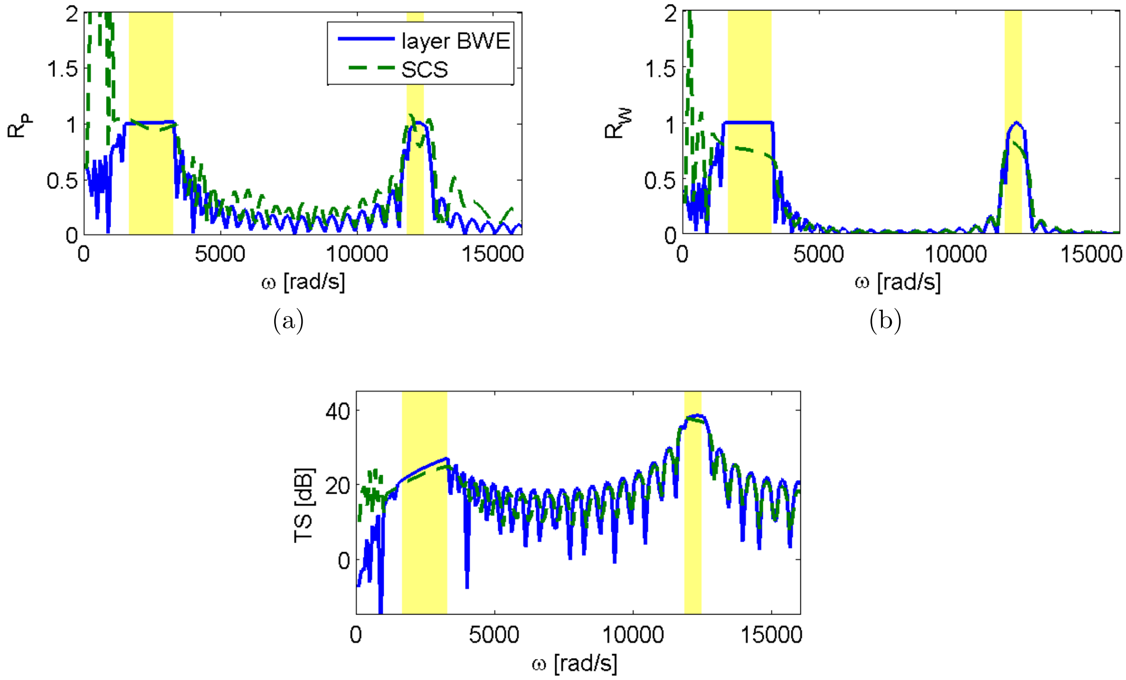

(a)

(b)

(c)

Figure 47: The frequency dependent (a) pressure reflection coefficient, (b) power reflection coefficient, and (c) target strength for a PC containing 8,000 bubbles. The data is computed with the layer BWE (blue) and SCS (dashed green line). The two frequency band gaps are highlighted in yellow.

6.2.2 Parametric studies

The target strength will be evaluated for five different PCs with varying size and shape. The size and number of bubbles is, rather, arbitrary; the shape is a main factor varied. The properties of each PC is listed in Table 1 and a few example PCs are illustrated in Fig. 48. Each PC contains NB air-filled bubbles with fixed a but varying topology and orientation. The PCs considered herein are cubic, spherical, and ellipsoidal in shape; the lengths are L_x, L_y, L_z in the respective x, y, z directions (dimensions are of the PC's bounding box). The incident plane wave's wavevector $\mathbf{k}_i$ is oriented along the $\hat{\mathbf{e}}_x$ direction with $\theta = 90°, \phi = 0°$.

Table 1: The geometrical properties of the five phononic crystals considered herein.

PC	A	B	C	D	E
body	cubic	cubic	spherical	ellipsoidal	ellipsoidal
NB	8,000	46,656	13,992	16,168	16,168
L_x, L_y, L_z [m]	8, 8, 8	14.4, 14.4, 14.4	12, 12, 12	20, 10, 10	10, 20, 10
volume $[m^3]$	512	2,986	905	1,047	1,047

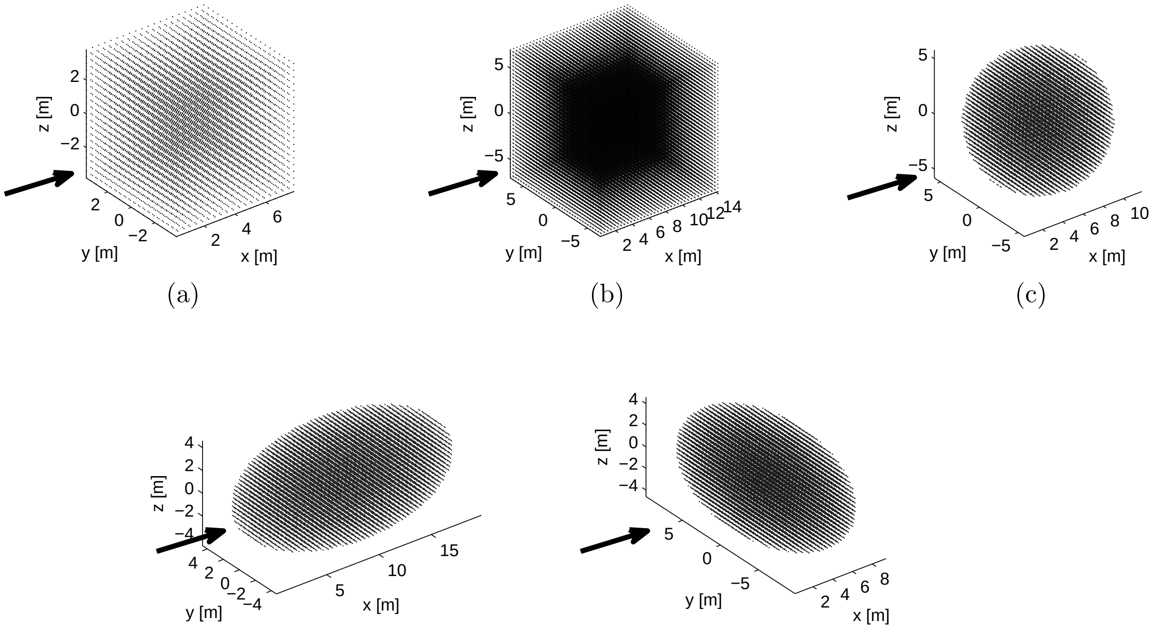

(a) (b) (c)

(d) (e)

Figure 48: Five PCs examined in this section: (a) PC A, (b) PC B, (c) PC C, (d) PC D, (e) PC E. Each PC has properties listed in Table 1. In each plot, the black arrow represents the direction of the incident plane wave.

The frequency dependent target strength for the five PCs is displayed in Fig. 49. A few remarks can be made regarding the target strength plots: (i) Due to Bragg scattering, the maximum TS occurs at a frequency such that $\pi c_i/\omega \sin\theta \cos\phi \approx a$. This frequency coincides within the second band gap. Additional band gaps are not present of the PC studied herein, even at additional frequencies that satisfy Bragg's law. This observation has been reported elsewhere, e.g. Ref. [66]. (ii) Below the first band gap, peaks in the TS occur at the collective resonance frequency of the PC. As cited in the literature, multiple scattering effects diminish the scattered field of the single bubble [81, 84], and instead the PC can exhibit a resonance frequency specific to the inherent structure, i.e. collective resonance [28]. (iii) The target strength within the first band gap does not exhibit a global maxima. Furthermore, since the Bloch waves do not propagate into the medium in this band gap frequency range there is minimal wave interaction at the back of the PC and the TS is approximately linear within the first band gap range. (iv) Depending on the PC's orientation and shape, the TS values within the first band gap can be less or greater than the target strength values for the frequency range exclusively between the first and second band gaps. Comparison of PC A and B indicates an increasing TS value within the first band gap, a result of an increase in the number of bubbles. The spherical PC, C, shows a mild target strength in the first band gap range, compared to the second band gap range. Due to the orientation change, the target strength in the first band gap of PC E is higher than that of PC D. It is predicted that, within the first band gap, the TS of PC D is higher than that of E since PC D exhibits a larger area parallel to the incoming plane wave direction. (v) The alternating local maxima/minima occur at frequencies that depend on the x length of the PC. These target strength results conclude: the Bragg band gap contains the maximum TS; the target strength within the first band gaps is approximately linear in frequency and can be of high magnitude, relative to other frequencies, as the PC size increases. Lastly, it is noted that the target strength computed with the BWE and HKI agrees very well for the cubic PCs A and B. It is important to note, the following observations can also be applied to a fish school of similar size and shape. Whether the size/shape observations translate to weakly disordered schools with complicated shape remains an open question.

6.3 Scattering from a spherical school

In this section the acoustic backscattering is considered, in both the frequency and time domain, for a spherical fish school. The purpose of this section is two-fold. First, the facet formalism introduced in Sec. 4.6 may be verified (for the ideal PC case) versus SCS. Secondly, by adding disorder, the spherical PC becomes a fish school, and the transient scattered response can be determined by using Fourier superposition with the facet formalism.

The PC geometry introduced for the facet formalism will be reused. For convenience, the school is reproduced in Fig. 50. The spherical PC is ideal; disorder is added explicitly later for the SCS. The school contains $NB = 104{,}312$ fish and the radius of the school is 12 m. Hahn [28] also examined the scattering from spherical shaped fish schools, albeit at a much lower frequency than the present study as his work was focused on the school's collective resonance.

6.3.1 Harmonic scattering

Here an explicit example is considered where a wave at $\omega = 3{,}000$ rad/s strikes the spherical phononic crystal (radius is 12 m) seen in Fig. 35a. Following the surface mesh, there are 148 total facets and of this set $NF = 76$ are ensonified. The mesh density was chosen to best approximate the actual spherical shape yet not yield very small facets. Each facet is (based on the square root of the triangle's area) slightly larger than the wavelength. There are approximately 60 unit cells in the direction of each facet's normal. The half-space BWE is calculated and the scattered pressure field is calculated directly from Eq. (99); one could also use the layer BWE. However, the band gap frequency of 3,000 implies, for large enough PCs, the half-space and layer BWE fields are identical.

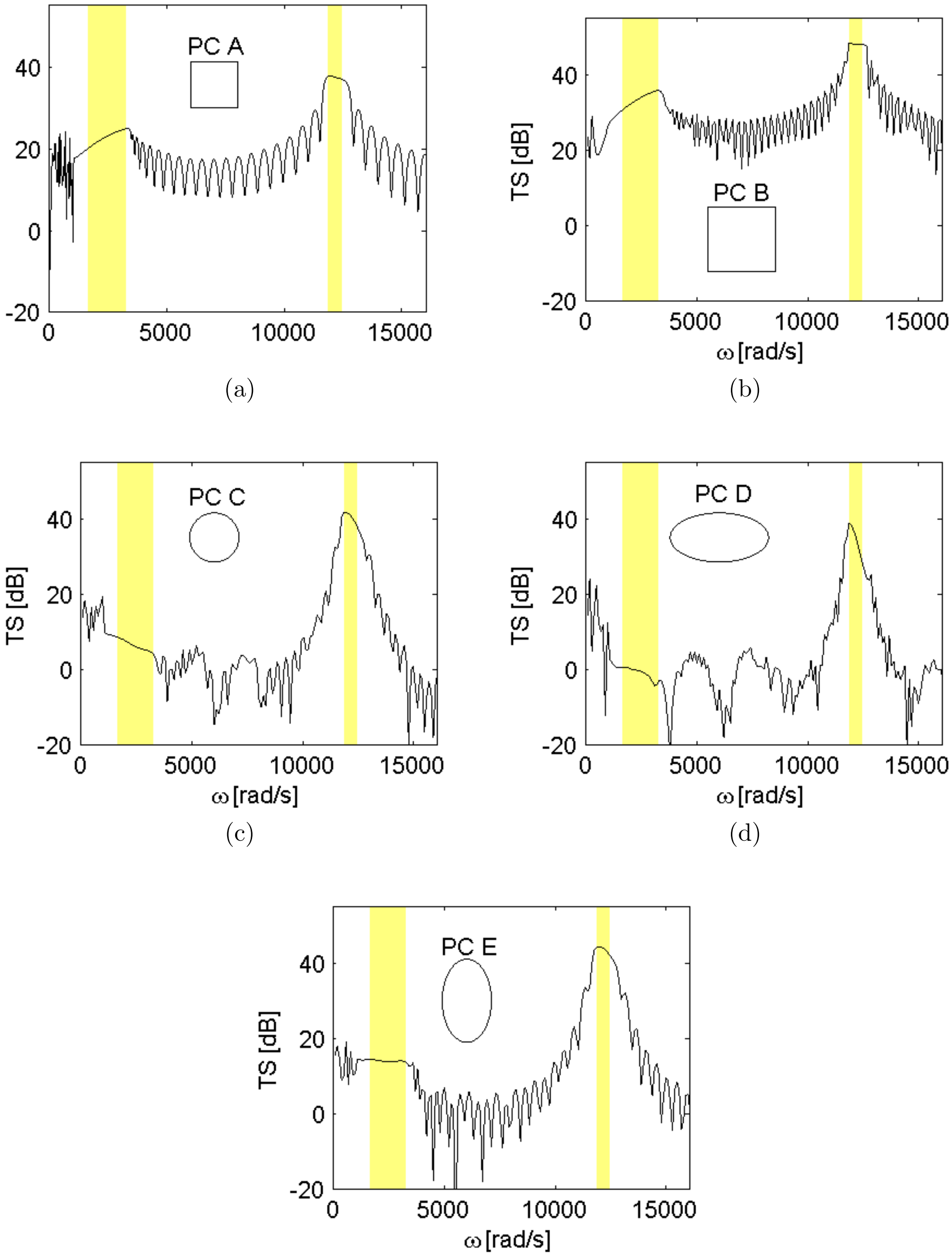

(a)

(b)

(c)

(d)

(e)

Figure 49: The frequency dependent target strength (note in dB) for (a) PC A, (b) PC B, (c) PC C, (d) PC D, and (e) PC E. In each plot, the two band gaps are highlighted in yellow.

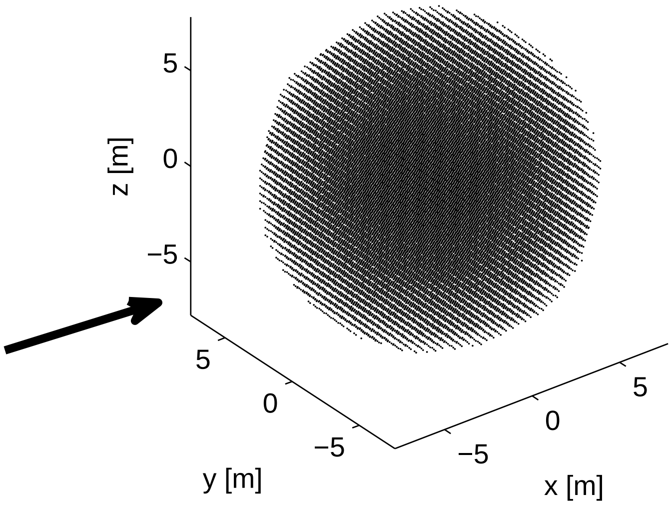

Figure 50: A spherical fish school of $NB = 104{,}312$ fish positioned in a simple cubic array with spacing $a = 0.4$ m; the outer radius of the school is 12 m. The incident wave is pointed in the direction shown by the arrow.

The real and imaginary components of the scattered pressure are compared against the facet approach versus the direct SCS calculation and shown in Fig. 51a and Fig. 51b. In the far field, toward the right hand side of the plots, there is excellent agreement in the real and imaginary parts of the scattered pressure. In both real and imaginary comparison plots there is a small, constant, phase error; the facet results leads the SCS results by approximately 0.4 rad. After adjusting for this phase offset, the magnitude of the complex relative error converges to 2% in the far field.

As before, the scattered pressure amplitude is compared using the facet technique versus the SCS technique, and respectively shown in Fig. 52a and Fig. 52b. Again, very good agreement is seen in the qualitative spatial behavior of the scattered pressure field between the two techniques. The near field peaks, close to the PC, are captured by the facet technique. Note the results presented in these two figures are backscattered pressure fields ($x < 0$). The forward scattered pressure fields do not agree as only facets with $\hat{\mathbf{n}}^j \cdot \mathbf{k}_i > 0$ are used. Also, as discussed, the facet formalism does not incorporate acoustic diffraction around each facet; the results, nevertheless, indicate positive agreement. Lastly, for ease on the computational resource requirements for the SCS technique, the PC's facets are about the size of a wavelength. A larger PC and larger facets is predicted to yield a more accurate scattering result; however, the presented facets and the approach still indicate positive results.

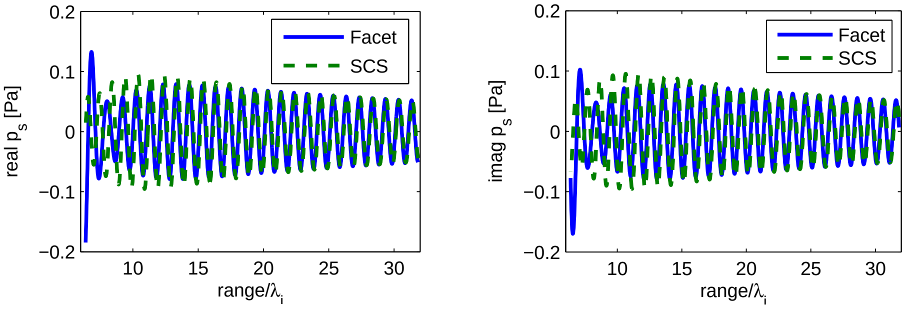

(a) (b)

Figure 51: (a) A comparison of the real part of the scattered pressure field by the facet (blue line) and the SCS technique (green line) versus normalized range. (b) A comparison of the imaginary part of the scattered pressure field by the facet (blue line) and the SCS technique (green line) versus normalized range.

6.3.2 Broadband pulse

Again, consider a source (and co-located receiver) at $\mathbf{x}$ = (-1000, 0, 0) m. The source emits the pulse (Eq. (97)) with modulation parameter $\eta = 250$ 1/s and carrier frequency $\omega_0 = 2460$ rad/s; see Fig. 53. The fractional bandwidth of the input signal is 0.17. Since the facet technique is valid in the first band gap range, the pulse's shape parameters are specifically chosen such that essentially all of the pulse's energy lies within this frequency range.

The incident wave travels and interacts with the spherical PC of 104,312 bubbles previously considered. Figure 54 shows the scattered pressure signal at the receiver. For comparison, both an ideal spherical PC and a disordered PC with $\tau = 0.1$ is used. Notably, there is a clear overall agreement between the facet and SCS pressure signals. The deviation in the frequency response between the facet and SCS technique

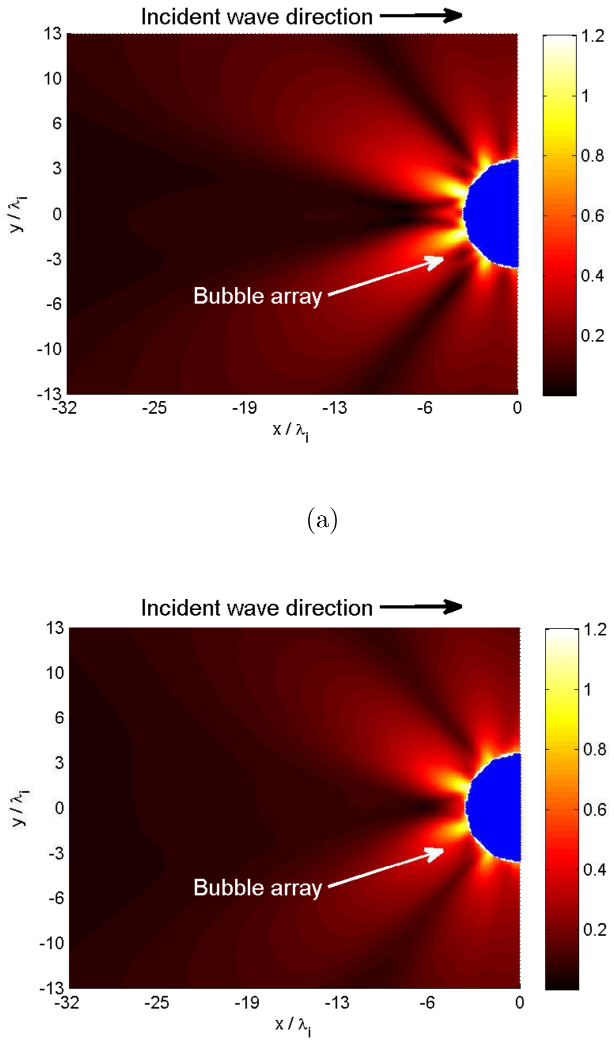

(a)

(b)

Figure 52: Amplitude of the scattered pressure field for (a) facet and (b) SCS. The bubble array is colored in blue for clarity. The incident plane wave at $\omega = 3{,}000$ rad/s strikes the PC in the direction shown. Note, the axis labels are normalized by λ_i.

leads to the disagreement for $t > 1.37$ s. Furthermore, the scattered pressure from the facet formalism shows good agreement when compared against the disordered PC. This observation coincides with the fact discussed in Sec. 6.2: the scattered pressure field, within the first band gap, is very robust to weak internal disorder. Overall, these transient results, for an input pulse spectrum contained within the first band gap, good agreement when using the facet technique to model the transient scattered

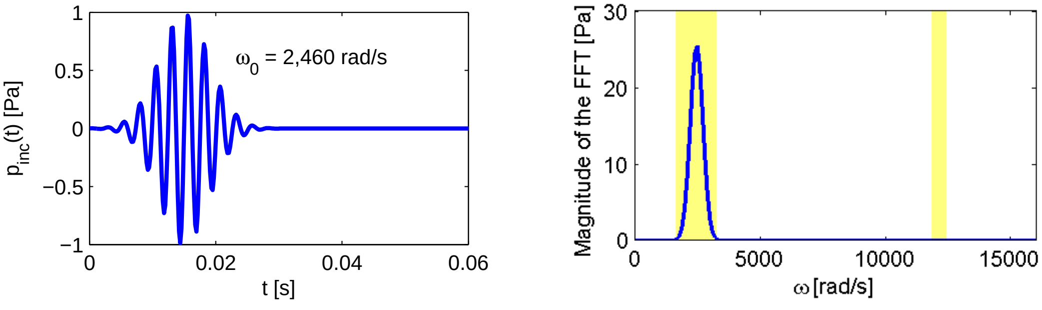

(a) (b)

Figure 53: (a) The input pulse from Eq. (97) with $\omega_0 = 2{,}460$ rad/s. (b) The magnitude of the fast Fourier transform of (a). The band gap ranges are highlighted.

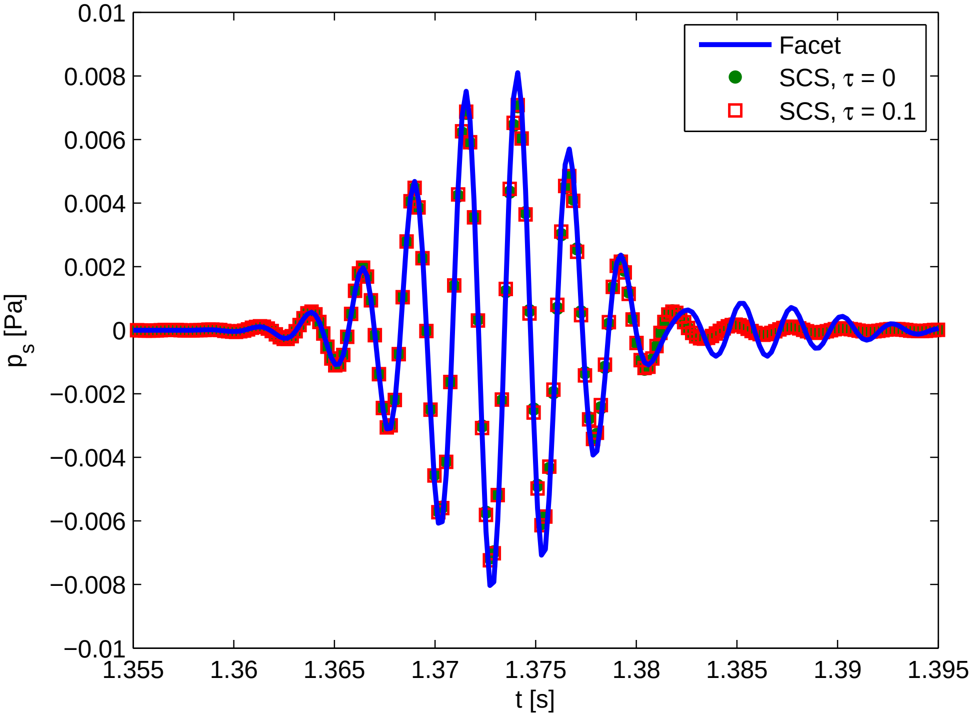

Figure 54: Time history of the pulse scattered by the spherical fish school of Fig. 50 using the facet (blue line), ideal school using SCS (green dots), and disordered school ($\tau = 0.1$) using SCS (red squares). The ideal and disordered results SCS are nearly identical. Note the horizontal time axes includes the travel time between the source and receiver.

behavior.

6.4 Scattering from a bean-shaped school

Based on the accurate harmonic and transient scattering results from the spherical school, an ambitious calculation is next performed. The school's shape, shown in Fig. 55, is a construction of the imagination and meant to push the boundaries of the facet formalism. The bean-shaped school contains NB = 382,269 fish with $\tau = 0.2.$; the school volume is 25,550 m^3. There is even a small ellipsoidal void of volume 50.2 m^3. The school is so large that populating the matrix $\mathbf{Q}$ directly would take over two terabytes of information, for a *single* frequency. Recall, use of the FMM avoids this matrix assembly and the single frequency solution took just a few hours; over all frequencies the solution lasted 13 days.

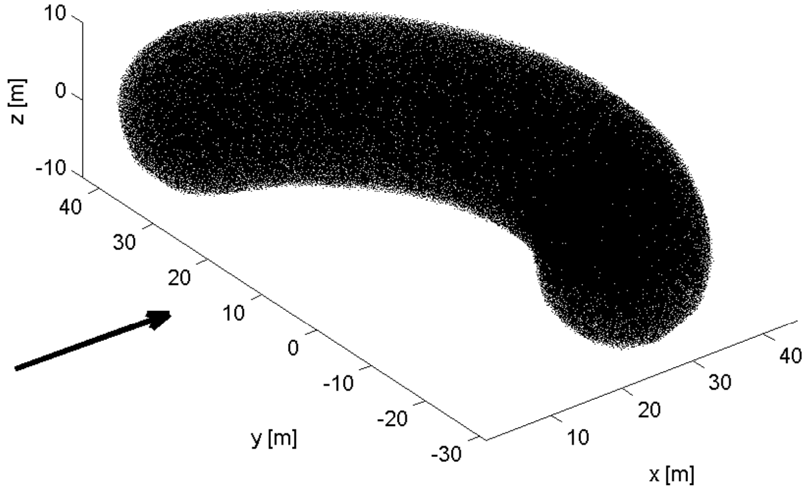

Figure 55: Bean-shaped school with NB = 382,269 fish, $\tau = 0.2$. The incident wave is pointed in the direction shown by the arrow.

Using a geometrical model, as discussed earlier, for the school, and creating a surface mesh, there are 488 facets; see Fig. 56. There are 266 ensonified facets.

Running the facet formalism on all 266 facets over the frequency range of interest

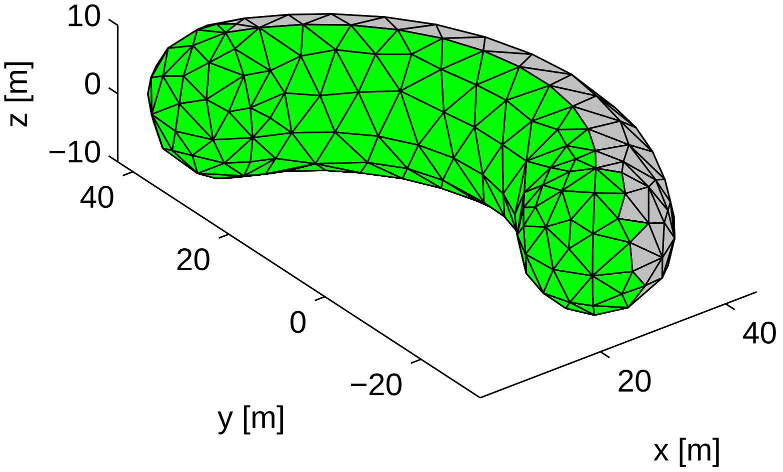

Figure 56: A faceted representation of the bean-shaped school from Fig. 55. There are 488 facets and the 266 ensonified facets are shaded green.

yields the scattered response. Computationally, the facet formalism can be calculated easily in a parallel manner; the resulting frequency simulation lasted only 3.5 days.

6.4.1 Harmonic scattering

Using the facet formalism, the scattered pressure is determined in the xy plane at ω = 3,000 rad/s. The scattered pressure field is shown for the facet and SCS case, respectively, in Fig. 57a and Fig. 57b. Clearly, the scattered pressure amplitude agrees well between the facet and SCS results, even with the fish school being disordered with $\tau = 0.2$. Notably, even close to the fish school, the pressure amplitude is accurate. Even though the facet formalism is intended to be used for backscatter, for forward scatter (right side of the above plots), the pressure amplitude is in agreement. This plot indicates the accuracy of the facet formalism, in the harmonic case, for predicting

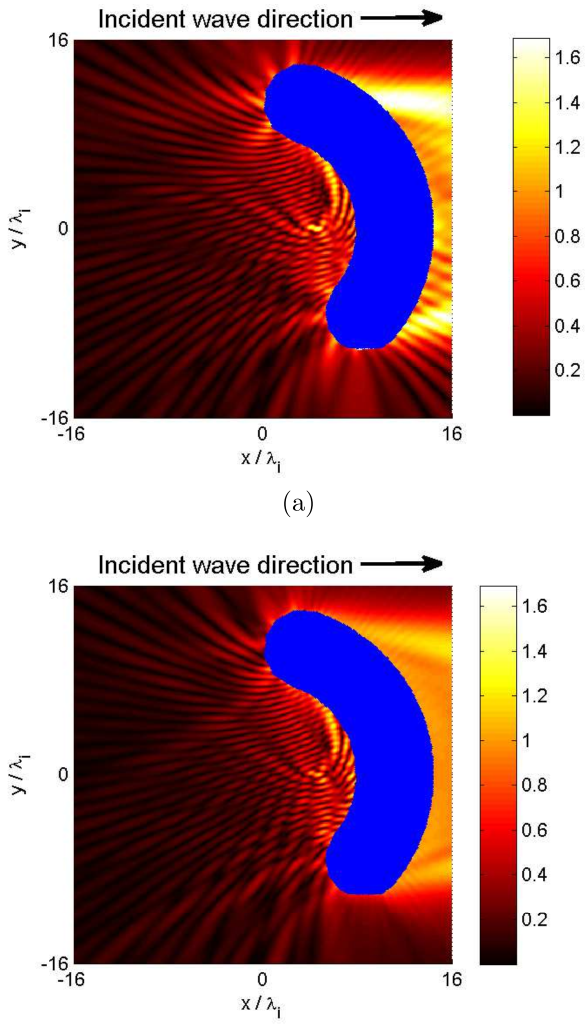

(a)

(b)

Figure 57: Amplitude of the scattered pressure field for (a) facet and (b) SCS. The fish school is colored in blue for clarity. The incident plane wave at ω = 3,000 rad/s strikes the PC in the direction shown. Note, the axis labels are normalized by λ_i.

the scattered pressure amplitude from a fish school with complex shape and internal disorder.

6.4.2 Broadband pulse

Following the agreement in the harmonic scattered field, the transient scattering result from a broadband pulse is considered. The same input pulse (and frequency spectrum) from Sec. 6.3.2 is used.

The transient scattered pressure field from the facets and SCS techniques is shown in Fig. 58. Notably (even in the band gap frequency range), there is a primary and secondary scattered pulses; the facet formalism and SCS agree well within these pulses. The primary pulse is a result of the scattering from the top left portion of the school; the secondary pulse is a result of scattering from the bottom right. Outside of these primary pulses there is disagreement. The differences in the facet and SCS

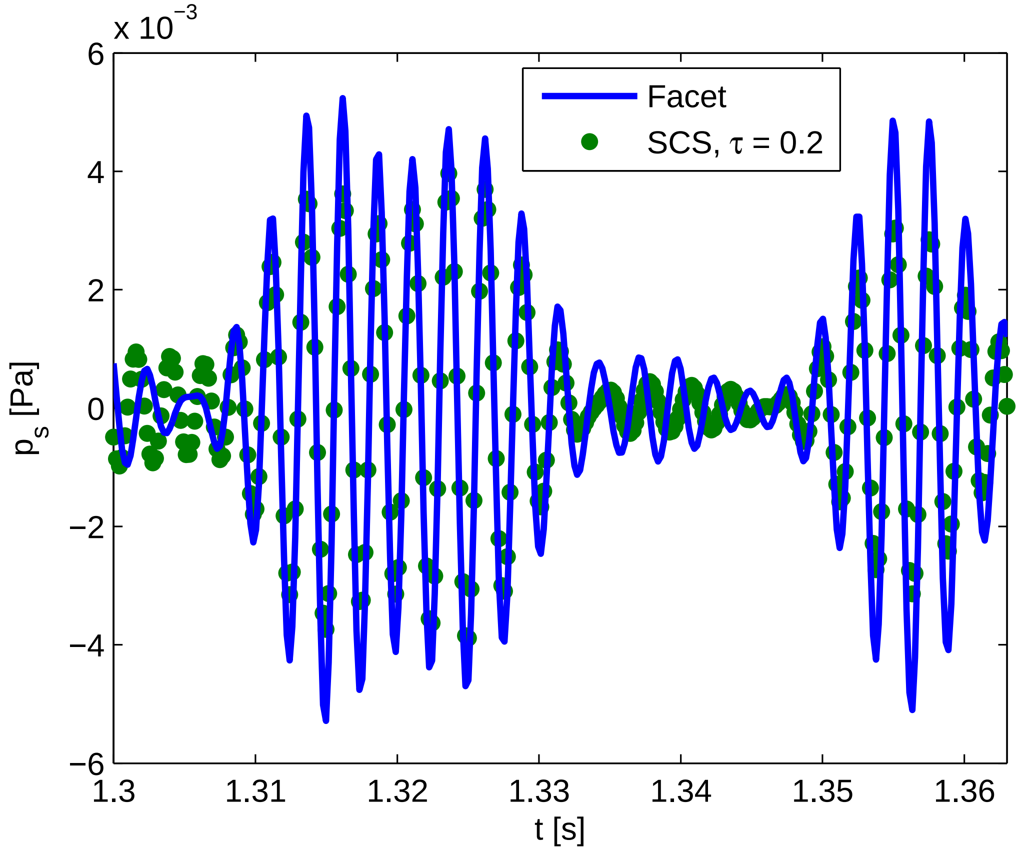

Figure 58: Time history of the pulse scattered by the bean-shaped fish school of Fig. 55 using the facet (blue line) and disordered school ($\tau = 0.2$) using SCS (green dots). The ideal and disordered results are nearly identical. Note the horizontal time axes includes the travel time between the source and receiver.

frequency response contribute to the errors in the transient analysis.

There are two key points to be concluded from this final transient result. First, the facet formalism can be applied to fish schools with complex (and even concave) geometry and yield accurate results. Secondly, as stated earlier, the introduction of weak internal disorder does not significantly change the backscattered pressure results when comparing the ideal facet model and SCS technique. Overall, this transient results indicates a promising trend: the facet formalism can be used to accurately predict the transient backscattering from a fish school with complicated geometry and disorder.

6.5 Conclusion

In this section the Bloch wave formalism was applied to study the scattering from fish schools. First, target strength studies explored the utility of the PC's band gaps to qualitative target strength predictions. Next, for a spherical and bean-shaped fish school the facet formalism was compared directly to the SCS technique. The harmonic and transient results, overall, indicated positive agreement, even versus the fish school with weak disorder.

The contributions from this chapter to the literature are: (i) Exploration of the connection between the school's target strength and the band gaps of the infinite PC; specifically, the role of the first band gap. (ii) Study of the harmonic and transient scattered field for a disordered fish school with complicated geometry using Bloch wave formalism. In future work, this last point may be extended upon for verification studies from the available experimental data.

CHAPTER VII

CONCLUSION OF THE RESEARCH

7.1 Summary

Overall in this work, respectively, Ch. 2 and Ch. 3 discussed the 2D and 3D Bloch wave expansion techniques. The scattering from finite PCs using the appropriate BWE was presented in Ch. 4. Chapter 5 considered the BWE and scattering applied to weakly disordered PCs. Finally, in Ch. 6, the above theory was demonstrated to be effective to determine the scattering from large fish schools. Specifically, when the incident acoustic pulse's energy is contained within the local resonance band gap of a unit cell (which describes the fish school), the scattered pressure can be accurately predicted using the BWE and facet formalism. In all chapters multiple verification studies were presented using the FEM and SCS techniques.

7.2 Compare and contrast

In this Thesis the pressure scattered by a fish school is computed using Bloch wave formalism and the SCS technique. To understand the applicability of each model, the advantages and disadvantages of each model are discussed.

Bloch wave formalism possesses several advantages when applied to scattering from large fish schools. First, using the finite element method for the fish body, a wider range of material and geometrical properties can be realized than is possible with the SCS or other analytical scattering techniques. An elaborate model, for example, can be seen in Feuillade and Nero [21] where the model contains an ellipsoidal fish body with viscous fluid properties, an elastic muscle wall, and an ellipsoidal air-filled swimbladder. Depending on the fish species, even non-convex or multiply-re-entrant fish swimbladders can be modeled; see [58] pp. 364; these bodies are certainly different from the bubbles considered herein. Secondly, the dispersion relationship demonstrated in Ch. 2 is valid for any frequency. However, there is a frequency limitation of the facet formalism. Thirdly, a significant result of the Bloch formalism: the formulation presented herein does not have any limitations from increasing school size or number of fish. Since the Bloch theorem reduces the domain of study to a single unit cell, the acoustic interaction of a high number of fish can be considered. Through the facet formalism it is possible to apply the theory to determine scattering from extremely large schools, for instance, in excess of ten million fish. As stated earlier, modeling the scattering from schools this large could be completely impossible using other methods, such as FEM and SCS. Even the facet formalism can be faster and more amenable to parallel computational processing schemes than the SCS technique.

In an exact sense, the Bloch formalism applies to ideal crystals. First, a realistic school inherently has variation of the fish size, variation of fish spacing and orientation, school geometry, and the possible presence of internal void regions. Clearly, the Bloch wave formalism and associated facets can not be applied to a fish school with very high levels of disorder as no periodic unit can be identified. Secondly, because the extent of the school is not modeled in the facet approach, the local resonance (which may be used to characterize's the school's shape [28]) may not be able to be ascertained from the scattering results. Further, due to the facet frequency limitations, scattering results for frequencies outside of the first band gap will be inaccurate.

On the other hand, the self-consistent scattering technique's chief advantage is flexibility. Any configuration of fish can be considered. Each fish can also vary in size and biological properties. The ability for one to consider scattering from arbitrary configurations of fish certainly is a valuable asset for modeling scattering from fish schools. Also the technique is very straight forward to implement, and of mild complexity with the fast multipole method. Additionally, time domain (as opposed to Fourier superposition) can be considered by direct integration of the differential equations governing the scattering processes [71]. This transient ability can be useful in attempts to model scattering from a school containing *moving* fish.

A disadvantage to the SCS technique is the low frequency limit; the precise numerical value of 'low' being rather arbitrary in general. Higher frequency studies, where multiple scattering can become dominant, can be impossible. Also, as the school gets larger and larger, the requirement on the computational resources grow. The FMM ameliorates this requirement; however, modeling each fish directly can demand enormous computational resources and thus hinder any effort for studying scattering from large fish schools.

7.3 Contributions

For completeness, the following contributions are repeated. These are the major contributions of this work to the scientific literature. Again, this list is meant to be brief; precise contributions can be found in the cited papers. The major contributions are:

1. A 2D and 3D half-space and layer BWE discussed and verified
2. The scattering from 2D and 3D, finite, PCs using the Helmholtz-Kirchhoff integral with the Bloch wave expansion
3. Using the BWE and HKI for 2D and 3D disordered PCs was found to be accurate, specifically, in the band gaps
4. Scattering from PCs with complex geometries using the facet formalism
5. Scattering from large fish schools using the combined theory

This Thesis culminated in the above contributions and several journal papers and conference presentations. The work may be extended to future endeavors, outlined in the next section.

7.4 Future work

At the end of any research project, there are ample opportunities for future work. The following list is meant to be a brief overview; it is not, by no means, complete. The items apply to the study of PCs or the use of the Bloch formalism for studying fish schools. Specifically for the BWE and PC scattering:

1. Modification of the layer BWE to be used for oblique (e.g. non-normal) wave incidence. Here, the finite size y, z dimensions of the PC may need to be considered.

2. In an actual finite system, because of edge effects, the pressure field at the edges of the PC may differ from that of the BWE. Possibly, a different (multiple scattering or finite element technique) may be combined with the BWE to more accurately describe the pressure field within the PC and on it's outside surface. This modification should improve the accuracy of the scattering computations via the HKI.

3. The perturbation formalism in Sec. 5.4 is within its infancy. Completion and verification of the technique, and its combination within the BWE, may prove an interesting avenue of future research.

4. Should one wish to apply the BWE formalism to PCs with solid constituents, appropriate extensions may be made. Possibly even shell elements [72] may be incorporated for efficiency with modeling inclusions with thin membranes.

5. A limitation of the facet formalism was discussed in Sec. 4.6.3. Future work may consider modification of the facet theory to circumvent this limitation and

thus enable the facet formalism to accurately predict the scattered field *for any* frequency.

6. Regarding implementation, it is anticipated that the numerical calculations can be expedited by employing the boundary element method (the basis of this method is the HKI) for the dispersion calculations versus the finite element method. Li *et al.* [53] employed the boundary element method for dispersion calculations. Furthermore, based on the fast multipole method (Appendix C), the numerical integration for the HKI can be expedited.

Specifically for the application of the theory to study scattering from fish schools:

1. A chief limitation to very large fish schools is the fact that the depth effects of the bubbles is neglected. To include this effect is more than changing the radius (according to Boyle's law), but rather, a right hand side term to the original finite element terms discussed in Sec. 2.4.1 may be necessary. Further, since there would be variation in the $z =$ depth direction, an improved facet formalism would be required.

2. Perform several studies to further validate the Bloch formalism for fish schools using published acoustical data. Although experimental data from known fish schools is limited, the reader is referred to Diachok [14] for a review of several fish acoustics topics

3. The facet formalism (and the associated Green's function) apply to a fish school in an *unbounded* medium. Using the theory outlined in Ingenito [33], knowing the unbounded response, the response for the fish school in a bounded (i.e. ocean surface and bottom) can be determined.

4. Modification of the facet formalism to the case where the fish school may contain different groups with possibly different fish, different packing densities, etc. One

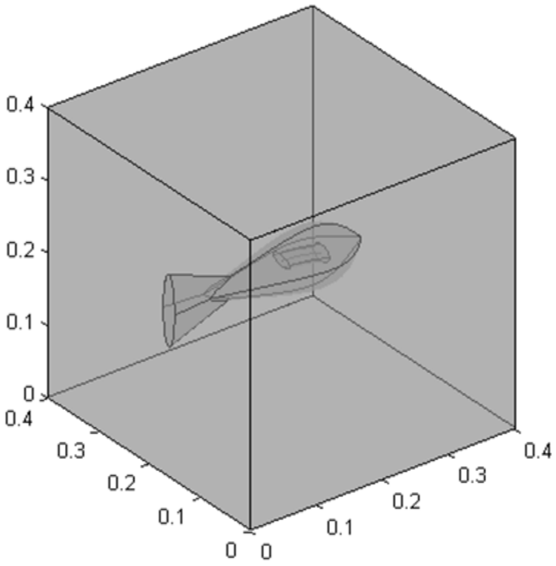

Figure 59: An example of a fish within a unit cell. The ratio of the volume of the swimbladder to the fish body is chosen to be 0.05.

possibility: each facet can be linked to a particular unit cell with the requisite properties pertaining to the specific areas in the fish school.

5. Exploration of the facet formalism and HKI for prediction of the pressure *inside* the fish school. Newly obtained numerical results have indicated this as a possibility but more thorough investigation, versus SCS, is needed. Unlike the SCS and other techniques, the Bloch formalism can avoid a singularity at the center of the fish's swimbladder and thus is able to predict the pressure accurately. In the investigation of a SONAR pulse's effect on individual fish, this ability of the Bloch formalism may be advantageous to the biology community.

6. Lastly, since the unit cell model can contain an arbitrary fish inclusion, it is possible to include a fish with a physiologically accurate swimbladder and other features. For example, consider Fig. 59.

Some of the above tasks may be difficult to accomplish with the Bloch wave formalism. Nevertheless, the above points offer interesting opportunities for future work.

Lastly, there are a few open questions that may be explored with the theory. Namely,

1. Comparing adequate experimental data to the numerical predictions, can inverse problems be attempted. For instance, can the fish species, abundant, or geometry properties be ascertained from in-situ acoustic measurements?
2. Can the fish school's internal dynamic effects, and the fish's motion swimming within the water itself, be incorporated in a dynamical model using the above theory?
3. Can the facet theory be modified, possibly with the layer BWE, for fish schools with internal voids?
4. Can the facet theory be applied, with equal accuracy, to geometries with many convex or concave features?

Future research endeavors may explore the previous topics and questions. However, with the presented techniques, it is clear that the acoustic scattering response from large fish schools can be calculated using Bloch wave formalism.

APPENDIX A

BLOCH WAVE COMPLETENESS

It was stated in Refs. [30] and [47] that the Bloch waves, at a particular frequency and plane wave incidence angle, form a complete function basis. The work later [49] implements a wave expansion, as is done in this Thesis, without thoroughly examining the completeness. A simple numerical experiment is proposed to illustrate that the set of Bloch waves is a suitable complete basis for an expansion. To establish completeness an arbitrary function $g(y)$ is formulated, which is valued on the FEM nodes on the PC interface at $x = 0$ and take an expansion of Bloch waves to replicate this function g. The incident wave parameters are taken as $\omega = 10,000$ and $\theta = 0$ and after processing propagating waves for group velocity there are 16 Bloch waves (following the five step procedure outlined in Sec 2.5). Note several more evanescent waves are included, versus the expansion for the same parameters in Sec. 2.7.2.1, as the rate of decay for evanescent waves is not of concern for the sake of this section.

The expansion is similar to Eq. (21)

$$\sum_{n=1}^{16} a_n p_n\left(0, y\right) = g(y) \tag{124}$$

where now the unknown coefficients a_n are to be determined. Taking an inner product of both sides of Eq. (124) with the m-th Bloch wave gives a set of matrix equations for the wave amplitude with components given by

$$F_{mn} a_n = C_m \tag{125a}$$

$$F_{mn} = \int_0^{a_2} p_n(0, y) p_m^*(0, y) \mathrm{d}y \tag{125b}$$

$$C_m = \int_0^{a_2} g(y) p_m^*(0, y) \mathrm{d}y. \tag{125c}$$

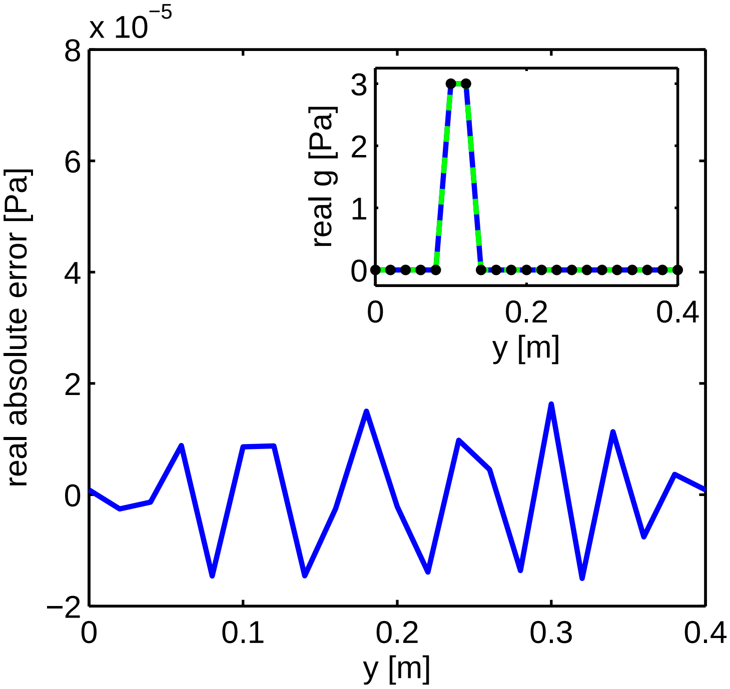

Figure 60: A test for Bloch wave completeness by considering an expansion of Bloch waves to replicate an arbitrary function. The difference between the expansion and $g(y)$ is plotted versus y. The inset shows the arbitrary function g with the FEM nodes shown as dots.

The results of the expansion are shown in Fig. 60. One will note the arbitrary function is exactly represented, between the nodes, by the Bloch wave expansion. This demonstration is not meant to be a rigorous completeness proof for all model parameters and frequencies, but rather a numerical experiment illustrating, in fact, that the set of Bloch waves used for the expansion described in this Thesis is complete.

APPENDIX B

THE 2D DISPERSION TECHNIQUE

This dispersion technique is suitable for finding the eigenvalues $\omega(\mathbf{k})$. In the $\omega(\mathbf{k})$ framework, the Bloch theorem of Eq. (1) can be taken as a different perspective. Consider a point $\mathbf{x}$ and a point translated m, n unit cells in the $\hat{\mathbf{e}}_x$,$\hat{\mathbf{e}}_y$ directions (m, n are integers). The theorem of Eq. (1) implies that $p(\mathbf{x} + m\hat{\mathbf{e}}_x + n\hat{\mathbf{e}}_y) = \hat{p}(\mathbf{x}) \exp i\mathbf{k} \cdot (ma_1\hat{\mathbf{e}}_x + na_2\hat{\mathbf{e}}_y)$. The quantity $\hat{p}$ is only the pressure inside the unit cell, e.g. $p(\mathbf{x})$. This particular form is advantageous for the $\omega(\mathbf{k})$ method.

Suppose the unit cell of the system at hand is described by

$$\left[-\omega^2\mathbf{M} + \mathbf{K}\right] \mathbf{p} = \mathbf{0} \tag{126}$$

where $\mathbf{M}, \mathbf{K}$ are the assembled versions of the terms given in Eq. (5). Upon viewing the Bloch theorem in the manner described above, one can consider a phase change of the degrees of freedom of the unit cell. For example, $p(a, 0) = \hat{p}(0, 0) \exp(ik_x a)$, etc for all nodes in the mesh model. To this end, let us write the nodal pressure vector $\mathbf{p}$ as

$$\mathbf{p} = \hat{\mathbf{T}}(\mathbf{k})\hat{\mathbf{p}} \tag{127}$$

where the matrix $\hat{\mathbf{T}}$ is *different* from the $\mathbf{T}$ given in Sec. 2.4.1. Specifically, using the notation $\hat{\mathbf{T}}(\mathbf{k})$, this matrix enforces the Bloch theorem in the manner previously described.

For convenience, the two-dimensional unit cell is repeated for the discussion here. To encompass the phase change outlined above, let us organize the nodal degree of

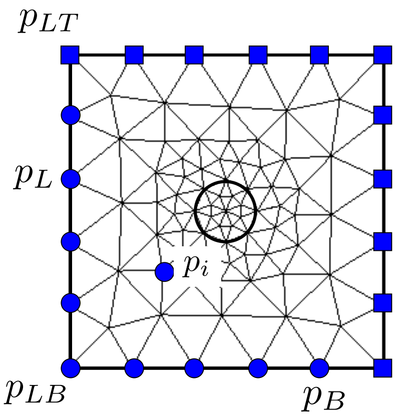

Figure 61: A representative finite element mesh of a single unit cell with reduced nodal degrees of freedom depicted as dots. The nodal degrees of freedom represented by squares are related by periodic boundary conditions via matrix $\mathbf{T}$. p_i is one node contained within the set $\mathbf{p}_i$.

freedom vector $\hat{\mathbf{p}}$ as

$$\hat{\mathbf{p}} = \begin{bmatrix} \mathbf{p}_L \\ \mathbf{p}_B \\ \mathbf{p}_{LB} \\ \mathbf{p}_I \end{bmatrix} \tag{128}$$

, where, again 'L' denotes the left degrees of freedom, 'B' for bottom, etc. This specific ordering is arbitrary. Next, using this ordering, the explicit elements of $\hat{\mathbf{T}}(\mathbf{k}) =$

$\hat{\mathbf{T}}(k_x, k_y)$ can be written as

$$\hat{\mathbf{T}}(\mathbf{k}) = \begin{bmatrix} \mathbf{I} & \mathbf{0} & \mathbf{0} & \mathbf{0} \\ \mathbf{I}\exp ik_x a_1 & \mathbf{0} & \mathbf{0} & \mathbf{0} \\ \mathbf{0} & \mathbf{I} & \mathbf{0} & \mathbf{0} \\ \mathbf{0} & \mathbf{I}\exp ik_y a_2 & \mathbf{0} & \mathbf{0} \\ \mathbf{0} & \mathbf{0} & \mathbf{I} & \mathbf{0} \\ \mathbf{0} & \mathbf{0} & \mathbf{I}\exp ik_x a_1 & \mathbf{0} \\ \mathbf{0} & \mathbf{0} & \mathbf{I}\exp ik_y a_2 & \mathbf{0} \\ \mathbf{0} & \mathbf{0} & \mathbf{I}\exp i(k_x a_1 + k_y a_2) & \mathbf{0} \\ \mathbf{0} & \mathbf{0} & \mathbf{0} & \mathbf{I} \end{bmatrix} \tag{129}$$

As done above, using $\mathbf{p} = \hat{\mathbf{T}}(\mathbf{k})\hat{\mathbf{p}}$ and pre-multiplying Eq. (126) by $\hat{\mathbf{T}^T}(-\mathbf{k})$ yields a new form for the equation of motion for the unit cell, namely,

$$\left[-\omega^2\hat{\mathbf{M}}(\mathbf{k}) + \hat{\mathbf{K}}(\mathbf{k})\right]\hat{\mathbf{p}} = \mathbf{0} \tag{130}$$

where $\hat{\mathbf{M}}(\mathbf{k}) = \hat{\mathbf{T}^T}(-\mathbf{k})\mathbf{M}\hat{\mathbf{T}}(\mathbf{k})$, etc. Note, if $\mathbf{k}$ is real, then $\hat{\mathbf{T}^T}(-\mathbf{k}) = \hat{\mathbf{T}^H}(\mathbf{k})$ where the superscript H denotes the matrix Hermitian operation. Lastly, the eigenvalues ω describe the dispersion relationship for the $\omega(\mathbf{k})$ method. It is of note, the three-dimensional $\omega(\mathbf{k})$ method takes on a similar derivation.

APPENDIX C

FAST MULTIPOLE METHOD

The practical use of the fast multipole method for the techniques discussed in this Thesis is given here. A deeper theoretical discussion can be found in Ref. [9] and the references cited therein.

Recall the matrix equation to solve for the scattered bubble amplitude is $\mathbf{Qw} = \mathbf{p}_{inc}$. This equation can be expanded, for an index u, as

$$\frac{\left(s_u - \omega^2 m_u - i\omega b_u\right) w_u}{\zeta} + \sum_{v=1, v\neq u}^{NB} w_v \frac{e^{ik_i|\mathbf{x}_u - \mathbf{x}_v|}}{|\mathbf{x}_u - \mathbf{x}_v|} = \frac{-e^{\mathbf{k}_i \cdot \mathbf{x}_u}}{\zeta} \tag{131}$$

where the scaling variable is $\zeta = -\omega^2 \rho_i / 4\pi$. The summation on the left side of the preceding equation can be a very expensive computation directly. Hence, the FMM is designed to *quickly* evaluate sums of this form, e.g., the second term on the left side

$$\sum_{v=1, v\neq u}^{NB} w_v \frac{e^{ik_i|\mathbf{x}_u - \mathbf{x}_v|}}{|\mathbf{x}_u - \mathbf{x}_v|}. \tag{132}$$

For clarification, recall the Green's function used in this Thesis contains a 4π normalization and is different from Eq. (132). Furthermore, the scaling parameter ζ is introduced explicitly because the numerical routines in Ref. [27] require input terms appearing exactly as shown in Eq. (132). Since the differential bubble volume w_u is unknown, Eq. (131) can be solved in an iterative manner such as the generalized minimal residual method (GMRES) where the FMM can be used to quickly evaluate the summation.

The FMM can also be used to accelerate calculations of the HKI from Eq. (92). The integral is discretized into a summation of monopole and dipole terms as

$$p_s\left(\mathbf{x}_f\right) = \int_S [G\nabla p - p\nabla G]\cdot\hat{\mathbf{n}} \ \mathrm{dS} \approx \sum_u \left[q_u \frac{e^{ik_i|\mathbf{x}_u - \mathbf{x}_f|}}{|\mathbf{x}_u - \mathbf{x}_f|} + d_u \hat{\mathbf{n}} \cdot \nabla_{\mathbf{x}_u} \frac{e^{ik_i|\mathbf{x}_u - \mathbf{x}_f|}}{|\mathbf{x}_u - \mathbf{x}_f|} \right]. \tag{133}$$

where the monopole strength $q_u = (\Delta^2/4\pi)\nabla p\left(\mathbf{x}_u\right) \cdot \hat{\mathbf{n}}$ and the dipole strength is $d_u = -(\Delta^2/4\pi)p(\mathbf{x}_u)$. The quantity Δ is the size of a discrete element involved in the approximation of the surface integral. Using the built-in routines in Ref. [27], summations of monopoles and dipoles can be added quickly.

APPENDIX D

PHONONIC CRYSTALS WITH VISCOUS DAMPING

In this Appendix, phononic crystals with viscous damping will be overviewed. Specifically, the dispersion technique introduced in Eq. (8) can be modified to model unit cell with damping.

For a 2D or 3D fluid PC, the density and sound speed for material i is ρ_i, c_i. With the introduction of viscous damping for fluid i, one can introduce a complex density and sound speed

$$\rho_i\left(\omega\right) = \frac{\rho_i^0}{Y\left(\omega\right)} \tag{134a}$$

$$c_i\left(\omega\right) = c_i^0 Y\left(\omega\right)^{1/2} \tag{134b}$$

where the quantity $Y(\omega)$ is a function of the frequency ω, the ideal density and speeds ρ_j^0, c_j^0

$$Y(\omega) = 1 - i\omega\frac{\xi_j}{\rho_j^0 c_j^0}. \tag{135}$$

with

$$\xi_j = \frac{4}{3}\mu_{D,j} + \mu_{B,j} \tag{136}$$

and

$$\alpha_j^{viscous} = \frac{2\xi_j\omega^2}{3\rho_j^0(c_j^0)^2} \tag{137}$$

In the above equations, $\mu_{D,j}, \mu_{B,j}$ represent, respectively, the dynamic viscosity and the bulk (volumetric) viscosity coefficients for viscous fluid j and $\alpha^{viscous}$ is the frequency dependent plane wave attenuation coefficient (also called the Stokes coefficient [80]) for the fluid j . Clearly, $\mu_{D,j}, \mu_{B,j} = 0$ correspond to ideal, inviscid, fluids. This complex fluid model encapsulates the bulk attenuation experienced by acoustic waves traveling in the fluid [11].

To synthesize a viscous fluid into the above FEM equations, recall the matrix terms from Eq. (5) contain terms such as $1/\rho$ and $1/\rho c^2$. For a viscous fluid, these quantities become (dropping j for brevity)

$$\frac{1}{\rho} = \frac{Y}{\rho^0} = \frac{1}{\rho^0} - \frac{i\omega\xi}{(c^0)^2} \tag{138a}$$

$$\frac{1}{\rho c^2} = \frac{1}{\rho^0 (c^0)^2} \tag{138b}$$

Comparison of the denominator coefficients in the matrix terms in Eq. (5) indicates, after assembly, that the mass matrix $\mathbf{M}$ is *not* altered by the introduction of viscous damping, but the stiffness and other matrices *are altered* by the presence of viscous damping. Specifically, for the stiffness matrix,

$$\mathbf{K}^{viscous}(\omega) = \mathbf{K} + i\omega \mathbf{K}^{imag} \tag{139}$$

where

$$K_{mn}^{imag,element} = \int_V \frac{-\xi}{(c^0)^2} \nabla\psi_m \cdot \nabla\psi_n \mathrm{d}V. \tag{140}$$

The matrices $\mathbf{A}_j$ and $\mathbf{B}$ follow in a similar form. Further note that, $\mathrm{Re}(\mathbf{K}^{viscous}) = \mathbf{K}$ is the same matrix discussed in Ch.2. Regarding implementation, the $\mathbf{K}^{imag}$ can be obtained by assembling the FEM matrices with an artificial density $\rho^* = -(c^0)^2/\xi$. Posing the artificial density (only for $\mathbf{K}, \mathbf{A}_j, \mathbf{B}$) in this way allows the matrices to be extracted as discussed in Sec. 2.4.2. Then, the frequency dependence can be added via Eq. (139).

After assembly, the eigenvalue problem follows the same form as Eq. (16). The group velocity calculations are changed accordingly since, now, more matrices are frequency dependent. As in [61], there is no effort to give a physical description for the imaginary part of the group velocity for a particular Bloch wave. Necessarily, the addition of viscous damping means all Bloch wavenumbers are complex. The BWE selection rules of Sec. 2.5 must still be applied: Bloch waves that exponentially grow or deliver power out of the PC medium are discarded. Lastly, for the viscous parameters experimentally measured for fish [56], the inclusion of a viscous fluid does not significantly alter the dispersion or the scattering; thus, the inviscid model used herein provides an adequate fish model.

REFERENCES

[1] Alvarez, A. and Ye, Z., "Effects of fish school structures on acoustic scattering," *ICES. J. Mar. Sci.*, vol. 56, no. 3, pp. 361–369, 1999.

[2] Anderson, P. W., "Absence of diffusion in certain random lattices," *Phys. Rev.*, vol. 109, no. 5, p. 1492, 1958.

[3] Andrews, M., Gong, Z., and Ratilal, P., "Effects of multiple scattering, attenuation and dispersion in waveguide sensing of fish," *J. Acoust. Soc. Am.*, vol. 130, p. 1253, 2011.

[4] Bendiksen, O., "Localization phenomena in structural dynamics," *Chaos, Solitons & Fractals*, vol. 11, no. 10, pp. 1621–1660, 2000.

[5] Bradley, C. E., "Time harmonic acoustic bloch wave propagation in periodic waveguides. part i. theory," *J. Acoust. Soc. Am.*, vol. 96, pp. 1844–1853, 1994.

[6] Bretagne, A., Tourin, A., and Leroy, V., "Enhanced and reduced transmission of acoustic waves with bubble meta-screens," *Appl. Phys. Lett.*, vol. 99, no. 22, pp. 221906–221906–3, 2011.

[7] Caleap, M., Drinkwater, B. W., and Wilcox, P. D., "Effective dynamic constitutive parameters of acoustic metamaterials with random microstructure," *New J. Phys.*, vol. 14, no. 3, p. 033014, 2012.

[8] Chen, Y. Y. and Ye, Z., "Theoretical analysis of acoustic stop bands in two-dimensional periodic scattering arrays," *Phys. Rev. E*, vol. 64, no. 3, p. 036616, 2001.

[9] Coifman, R., Rokhlin, V., and Wandzura, S., "The fast multipole method for the wave equation: A pedestrian prescription," *IEEE Antennas and Propag. Mag.*, vol. 35, no. 3, pp. 7–12, 1993.

[10] Collins, J. D. and Thomson, W. T., "The eigenvalue problem for structural systems with statistical properties," *AIAA Journal*, vol. 7, no. 4, pp. 642–648, 1969.

[11] COMSOL, "Comsol multiphysics v. 4.3b reference manual," 2012. pp. 862-907.

[12] Devaud, M., Hocquet, T., and Leroy, V., "Sound propagation in a monodisperse bubble cloud: From the crystal to the glass," *Eur. Phys. J. E*, vol. 32, no. 1, pp. 13–23, 2010.

[13] Devin Jr., C., "Survey of thermal, radiation, and viscous damping of pulsating air bubbles in water," *J. Acoust. Soc. Am.*, vol. 31, no. 12, pp. 1654–1667, 1959.

[14] Diachok, O., "Effects of absorptivity due to fish on transmission loss in shallow water," *J. Acoust. Soc. Am.*, vol. 105, no. 4, pp. 2107–2128, 1999.

[15] Ding, Y., Liu, Z., Qiu, C., and Shi, J., "Metamaterial with simultaneously negative bulk modulus and mass density," *Phys. Rev. Lett.*, vol. 99, no. 9, p. 093904, 2007.

[16] Duhamel, D., Mace, B. R., and Brennan, M. J., "Finite element analysis of the vibrations of waveguides and periodic structures," *J. Sound Vib.*, vol. 294, no. 1, pp. 205–220, 2006.

[17] Farquhar, G. B., *Biological sound scattering in the oceans: a review.* Oceanic sound scattering prediction, Eds. N. R. Andersen and B. J. Zahuranec, 1976. pp. 493-528.

[18] Farzbod, F., *Analysis of Bloch formalism in undamped and damped periodic structures.* Thesis, Georgia Institute of Technology, 2010.

[19] Farzbod, F. and Leamy, M. J., "The treatment of forces in bloch analysis," *J. Sound Vib.*, vol. 325, no. 3, pp. 545–551, 2009.

[20] Feuillade, C., "Scattering from collective modes of air bubbles in water and the physical mechanism of superresonances," *J. Acoust. Soc. Am.*, vol. 98, pp. 1178–1190, 1995.

[21] Feuillade, C. and Nero, R. W., "A viscous-elastic swimbladder model for describing enhanced-frequency resonance scattering from fish," *J. Acoust. Soc. Am.*, vol. 103, no. 6, pp. 3245–3255, 1998.

[22] Feuillade, C., Nero, R. W., and Love, R. H., "A low-frequency acoustic scattering model for small schools of fish," *J. Acoust. Soc. Am.*, vol. 99, no. 1, pp. 196–208, 1996.

[23] Foldy, L. L., "The multiple scattering of waves. i. general theory of isotropic scattering by randomly distributed scatterers," *Phys. Rev.*, vol. 67, no. 3-4, pp. 107–119, 1945.

[24] Golub, G. H. and Van Loan, C. F., *Matrix computations*, vol. 4. JHU Press, 2013. pp. 260.

[25] Gonella, S. and Ruzzene, M., "Homogenization and equivalent in-plane properties of two-dimensional periodic lattices," *Int. J. Solids Struct.*, vol. 45, no. 10, pp. 2897–2915, 2008.

[26] Gralak, B., Enoch, S., and Tayeb, G., "Anomalous refractive properties of photonic crystals," *J. Opt. Soc. Am. A*, vol. 17, no. 6, pp. 1012–1020, 2000.

[27] Greengard, L. and Gimbutas, Z., "Fast multipole method library 3d for matlab," 2012.

[28] Hahn, T. R., "Low frequency sound scattering from spherical assemblages of bubbles using effective medium theory," *J. Acoust. Soc. Am.*, vol. 122, p. 3252, 2007.

[29] Hou, Z., Fu, X., and Liu, Y., "Calculational method to study the transmission properties of phononic crystals," *Phys. Rev. B*, vol. 70, no. 1, p. 014304, 2004.

[30] Hsue, Y.-C., Freeman, A. J., and Gu, B.-Y., "Extended plane-wave expansion method in three-dimensional anisotropic photonic crystals," *Phys. Rev. B*, vol. 72, no. 19, p. 195118, 2005.

[31] Hussein, M. I., "Reduced bloch mode expansion for periodic media band structure calculations," *Proc. R. Soc. A*, vol. 465, no. 2109, pp. 2825–2848, 2009.

[32] Hussein, M. I., "Theory of damped bloch waves in elastic media," *Phys. Rev. B*, vol. 80, no. 21, p. 212301, 2009.

[33] Ingenito, F., "Scattering from an object in a stratified medium," *J. Acoust. Soc. Am.*, vol. 82, no. 6, pp. 2051–2059, 1987.

[34] Joannopoulos, J. D., Johnson, S. G., Winn, J. N., and Meade, R. D., *Photonic crystals: Modeling the flow of light.* Hoboken, NJ: Princeton University Press, 2nd ed., 2008. pp. 27-43, 221-227.

[35] Jones, B. A., *Echo statistics of aggregations of scatterers in a random waveguide: Application to biologic sonar clutter.* Thesis, Naval Postgraduate School, 2012.

[36] Kinsler, L. E., Frey, A. R., Coppens, A. B., and Sanders, J. V., *Fundamentals of acoustics.* Hoboken, NJ: John Wiley & Sons, Inc., 4th ed., 1999. pp. 152-155.

[37] Krokhin, A. A., Halevi, P., and Arriaga, J., "Long-wavelength limit (homogenization) for two-dimensional photonic crystals," *Phys. Rev. B*, vol. 65, no. 11, p. 115208, 2002. PRB.

[38] Krynkin, A., Umnova, O., Taherzadeh, S., and Attenborough, K., "Analytical approximations for low frequency band gaps in periodic arrays of elastic shells," *J. Acoust. Soc. Am.*, vol. 133, pp. 781–791, 2013.

[39] Kulpe, J. A., Leamy, M. J., and Sabra, K. G., "Modeling the acoustic scattering from large fish schools using the bloch-floquet theorem," in *Proceedings of Meetings on Acoustics*, vol. 19, p. 005026, 2013.

[40] Kulpe, J. A., Leamy, M. J., and Sabra, K. G., "Determination of acoustic scattering from a two-dimensional finite phononic crystal using bloch wave expansion," in *ASME International Design Engineering Technical Conferences*, Buffalo, NY, 2014.

[41] Kulpe, J. A., Sabra, K. G., and Leamy, M. J., "On the application of bloch wave expansion to study acoustic scattering form phononic crystals with complex geometry," *J. Acoust. Soc. Am.*, vol. In preparation, 2015.

[42] Kulpe, J. A., Sabra, K. G., and Leamy, M. J., "Bloch-wave expansion technique for predicting wave reflection and transmission in two-dimensional phononic crystals," *J. Acoust. Soc. Am.*, vol. 135, no. 4, pp. 1808–1819, 2014.

[43] Kulpe, J. A., Sabra, K. G., and Leamy, M. J., "A three-dimensional bloch wave expansion to determine external scattering from finite phononic crystals," *J. Acoust. Soc. Am.*, vol. Submitted, 2014.

[44] Kushwaha, M. S., Djafari-Rouhani, B., and Dobrzynski, L., "Sound isolation from cubic arrays of air bubbles in water," *Phys. Lett. A*, vol. 248, no. 2, pp. 252–256, 1998.

[45] Kushwaha, M. S. and Halevi, P., "Giant acoustic stop bands in twodimensional periodic arrays of liquid cylinders," *Appl. Phys. Lett.*, vol. 69, no. 1, pp. 31–33, 1996.

[46] Langlet, P., HladkyHennion, A., and Decarpigny, J., "Analysis of the propagation of plane acoustic waves in passive periodic materials using the finite element method," *J. Acoust. Soc. Am.*, vol. 98, pp. 2792–2800, 1995.

[47] Laude, V., Achaoui, Y., Benchabane, S., and Khelif, A., "Evanescent bloch waves and the complex band structure of phononic crystals," *Phys. Rev. B*, vol. 80, no. 9, p. 092301, 2009.

[48] Laude, V., Aoubiza, B., Achaoui, Y., Benchabane, S., and Khelif, A., "Evanescent bloch waves in phononic crystals," *Proc. SPIE 7223, Photonic and Phononic Crystal Materials and Devices IX*, vol. 7223, pp. 72230E–72230E–9, 2009.

[49] Laude, V., Moiseyenko, R. P., Benchabane, S., and Declercq, N. F., "Bloch wave deafness and modal conversion at a phononic crystal boundary," *AIP Adv.*, vol. 1, no. 4, pp. 041402–1 to 041402–11, 2011.

[50] Leamy, M. J. and Ruzzene, M., "Dynamics of complex lattice models," 2013. Internal report.

[51] Leamy, M. J., "Exact wave-based bloch analysis procedure for investigating wave propagation in two-dimensional periodic lattices," *J. Sound Vib.*, vol. 331, no. 7, pp. 1580–1596, 2012.

[52] Leroy, V., Bretagne, A., Fink, M., Willaime, H., Tabeling, P., and Tourin, A., "Design and characterization of bubble phononic crystals," *Appl. Phys. Lett.*, vol. 95, no. 17, pp. 171904–171904–3, 2009.

[53] Li, F.-L., Wang, Y.-S., Zhang, C., and Yu, G.-L., "Bandgap calculations of two-dimensional solidfluid phononic crystals with the boundary element method," *Wave Mot.*, vol. 50, no. 3, pp. 525–541, 2013.

[54] Li, Z.-Y., Zhang, X., and Zhang, Z.-Q., "Disordered photonic crystals understood by a perturbation formalism," *Phys. Rev. B*, vol. 61, no. 23, p. 15738, 2000.

[55] Liu, Z., Zhang, X., Mao, Y., Zhu, Y., Yang, Z., Chan, C. T., and Sheng, P., "Locally resonant sonic materials," *Science*, vol. 289, no. 5485, pp. 1734–1736, 2000.

[56] Love, R. H., "Resonant acoustic scattering by swimbladder-bearing fish," *J. Acoust. Soc. Am.*, vol. 64, pp. 571–580, 1978.

[57] Mead, D., "Waves and modes in finite beams: application of the phase-closure principle," *J. Sound Vib.*, vol. 171, no. 5, pp. 695–702, 1994.

[58] Medwin, H. and Clay, C. S., *Fundamentals of acoustical oceanography.* Applications of Modern Acoustics, San Diego, CA: Academic Press, 1st ed., 1997. pp. 234-254.

[59] Moiseyenko, R. P., Declercq, N. F., and Laude, V., "Numerical investigation of diffraction of acoustic waves by phononic crystals," in *AIP Conference Proceedings*, vol. 1433, pp. 319–322, 2012.

[60] Moiseyenko, R. P., Herbison, S., Declercq, N. F., and Laude, V., "Phononic crystal diffraction gratings," *J. Appl. Phys.*, vol. 111, no. 3, pp. 034907–034907–6, 2012.

[61] Moiseyenko, R. P. and Laude, S., "Material loss effect on the dispersion of bloch waves in phononic crystals," in *Ultrasonics Symposium (IUS), 2010 IEEE*, pp. 1857–1860, IEEE, 2010.

[62] Narisetti, R. K., Leamy, M. J., and Ruzzene, M., "A perturbation approach for predicting wave propagation in one-dimensional nonlinear periodic structures," *J. Vib. Acoust.*, vol. 132, no. 3, p. 031001, 2010.

[63] Nero, R. W., Feuillade, C., Thompson, C. H., and Love, R. H., "Near-resonance scattering from arrays of artificial fish swimbladders," *J. Acoust. Soc. Am.*, vol. 121, no. 1, pp. 132–143, 2007.

[64] Olsson III, R. and El-Kady, I., "Microfabricated phononic crystal devices and applications," *Meas. Sci. Technol.*, vol. 20, no. 1, p. 012002, 2009.

[65] Partridge, B. L., Pitcher, T., Cullen, J. M., and Wilson, J., "The three-dimensional structure of fish schools," *Behav. Ecol. Sociobiol.*, vol. 6, no. 4, pp. 277–288, 1980.

[66] Phani, A. S., Woodhouse, J., and Fleck, N. A., "Wave propagation in two-dimensional periodic lattices," *J. Acoust. Soc. Am.*, vol. 119, pp. 1995–2005, 2006.

[67] Pierce, A. D., *Acoustics: An introduction to its physical principles and applications.* Melville, NY: Acoustical Society of America, 3rd ed., 1994. pp. 100-125.

[68] Pitcher, T. J., "The three-dimensional structure of schools in the minnow, *Phoxinus phoxinus* (l.)," *Anim. Behav.*, vol. 21, no. 4, pp. 673–686, 1973.

[69] Pitcher, T. J. and Partridge, B. L., "Fish school density and volume," *Mar. Biol.*, vol. 54, no. 4, pp. 383–394, 1979.

[70] Qiu, C., Liu, Z., Mei, J., and Ke, M., "The layer multiple-scattering method for calculating transmission coefficients of 2d phononic crystals," *Solid State Commun.*, vol. 134, no. 11, pp. 765–770, 2005.

[71] Raveau, M. P. and Feuillade, C., "Time domain investigations of acoustical scattering from schools of swim bladder fish," *J. Acoust. Soc. Am.*, vol. 135, no. 4, pp. 2177–2177, 2014.

[72] Reddy, J. N., *An introduction to the finite element method.* New York: McGraw Hill, 3rd ed., 2006. pp. 410-523.

[73] Romero-Garcia, V., Pico, R., Cebrecos, A., Staliunas, K., and Sanchez-Morcillo, V. J., "Angular band gaps in sonic crystals: evanescent waves and spatial complex dispersion relation," *J. Vib. Acoust.*, vol. 135, no. 4, pp. 041012–041018, 2013.

[74] Ruan, Z., Qiu, M., Xiao, S., He, S., and Thylen, L., "Coupling between plane waves and bloch waves in photonic crystals with negative refraction," *Phys. Rev. B*, vol. 71, no. 4, p. 045111, 2005.

[75] Sanchis, L., Cervera, F., Sanchez-Dehesa, J., Sanchez-Perez, J. V., Rubio, C., and MartnezSala, R., "Reflectance properties of two-dimensional sonic band-gap crystals," *J. Acoust. Soc. Am.*, vol. 109, pp. 2598–2605, 2001.

[76] Shinozuka, M. and Astill, C. J., "Random eigenvalue problems in structural analysis," *AIAA Journal*, vol. 10, no. 4, pp. 456–462, 1972.

[77] Sigalas, M., Kushwaha, M. S., Economou, E. N., Kafesaki, M., Psarobas, I. E., and Steurer, W., "Classical vibrational modes in phononic lattices: Theory and experiment," *Z. Kristallogr.*, vol. 220, no. 9-10, pp. 765–809, 2005.

[78] Sukhovich, A., Jing, L., and Page, J. H., "Negative refraction and focusing of ultrasound in two-dimensional phononic crystals," *Phys. Rev. B*, vol. 77, no. 1, p. 014301, 2008.

[79] Sun, J.-H. and Wu, T.-T., “Propagation of acoustic waves in phononic-crystal plates and waveguides using a finite-difference time-domain method,” *Phys. Rev. B*, vol. 76, no. 10, p. 104304, 2007.

[80] Temkin, S., *Elements of acoustics.* Melville, NY: Acoustical Society of America, 2001. pp. 388.

[81] Twersky, V., “Multiple scattering of waves and optical phenomena,” *J. Opt. Soc. Am.*, vol. 52, no. 2, pp. 145–169, 1962.

[82] van der Aa, N., “Perturbation theory for eigenvalue problems,” 2005. Last accessed Oct. 1, 2014.

[83] Weber, T. C., Lutcavage, M. E., and Schroth-Miller, M. L., “Near resonance acoustic scattering from organized schools of juvenile atlantic bluefin tuna (thunnus thynnus),” *J. Acoust. Soc. Am.*, vol. 133, p. 3802, 2013.

[84] Weston, D. E., “Acoustic interaction effects in arrays of small spheres,” *J. Acoust. Soc. Am.*, vol. 39, no. 2, pp. 316–322, 1966.

[85] Williams, E. G., *Fourier acoustics: sound radiation and nearfield acoustical holography.* London, UK: Academic Press, 1st ed., 1999. pp. 251-262.

[86] Wu, T. W., *Boundary element acoustics: Fundamentals and computer codes*, vol. 7 of *Advances in Boundary Element.* Southampton, UK: WIT Press, 1st ed., 2000. pp. 20-21, 31.

[87] Yeh, P., “Electromagnetic propagation in birefringent layered media,” *J. Opt. Soc. Am.*, vol. 69, no. 5, pp. 742–756, 1979.

[88] Zienkiewicz, O. C., Taylor, R. L., and Zhu, J. Z., *The finite element method: Its basis and fundamentals.* Burlingtonm, MA: Elsevier, 6th ed., 2005. pp. 637.